UNIVERSITÀ
DEGLI STUDI
DI PADOVA

UNIVERSITA' DEGLI STUDI DI PADOVA

Dipartimento di Ingegneria Industriale DII

Corso di Laurea Magistrale in Ingegneria dei Materiali

Correlation between wear properties and microstructure of the 316L+10%WC composite

MATTIA NORDERA
Matricola 1177799

Supervisors:
Prof. Irene Calliari
Prof. Anne Mertens

Co-supervisors:
Tommaso Maurizi-Enrici
Olivier Dedry

Academic year 2019/2020

Abstract

In the present work, a detailed investigation concerns the correlation between microstructure and wear resistance of the SS316L+10%WC (vol.%) composite fabricated by Laser Cladding (LC) technique is reported. The microstructure of this metal matrix composite (MMS) is composed by partially dissolved WC carbides surrounded by a reinforced austenitic matrix. This microstructure was investigated by means of Optical Microscopy (OM) and Scanning Electron Microscope (SEM) in order to establish the carbides distribution and the phases present in the composite. The wear behaviour was characterised my means the use of Tribometer tests followed by Profilometer and SEM analyses on the post-mortem surfaces. The OM analyses have shown a greater frequency of the carbides in the last deposited layers together with a different size of the carbides in the whole material varying from 20 to 130μm. The SEM analyses have ensured the presence of different types of carbides formed during the process due to the partial or total dissolution of the WC in contact with the molten metal. Vickers hardness test was performed on the cross section in order to compare this property with the hardness of the pure SS316L obtained by LC, used as reference. The result exhibited a greater average hardness of the composite (around 260) than the pure SS316L (around 180) due to the complete and partial dissolution of the reinforcement. The main goal of this work was focused on the study of the wear behaviour of this metal matrix composite. Several wear mechanisms were recognised after Tribometer tests and they were present in every test performed. Presence of a steady value of friction coefficient was noted in each test affirming the formation of a stable tribolayer. The growth of this partial oxidized tribolayer starts from the undissolved WC carbides which act as a protection against wear. Formation of debris occurred due to the worn of the counter-body (alumina ball) and of the track surface leading to generation of grooves more or less deep. Worn of the alumina ball always occurred since EDS analyses on the post-mortem surfaces showed traces of aluminium in each track. Also presence of oxygen was always noted.

Acknowledgments

First of all, I want to thank all my family to their continuous belief in me during my university career. Probably without them, I would not have written this master thesis.

I am really grateful to all my friends who I met in Padua during these years. I spent good time together, working hard and at the same I enjoyed and shared many things. Also a big thank to my friends who live in Verona because they were always present when I was in trouble, helping and motivating me.

I would like to thank Prof. Irene Calliari for her patience and availability for satisfied my request for the Erasmus mobility period.

I am infinitely grateful to my two supervisors in ULiege, Olivier Dedry and Tommaso Maurizi-Enrici for helping me during my work. I learned to use a lot of different instruments, I improved my technical English written and speaking and also, I understood how to work in a correct way in a research field. A big thank to Sylvie Salieri for the preparation of my samples before the analyses and her patience. I am also grateful to the entire team of the Metallic Material Science (MMS): Jérôme T. Tchuindjang, Hakan Paydas, Jocelyn Delahaye and Rosine Pirson for their availability during my mobility period in ULiege.

A big thank to my Erasmus friends for sharing many fun moments and for making this Erasmus experience unforgettable for me. I improved a lot my bad initial English mainly thanks to the help of my flatmates with whom I shared really nice moments.

Table of Contents

List of Figures

List of Tables

1. Introduction

The conventional surface cladding processes such as thermal spraying, plasma spraying and arc welding [1–3] of same or similar material as substrate or wear resistance overlays [4] have been investigated for years in order to solve problems concerning deep cracks and wear failures of components. This is mainly due to fatigues and overload operating conditions of elements in transportation and aerospace fields [5]. Several limitations such as large heat affected zone (HAZ), large deformation, less geometrical accuracy and poor surface quality have been noted in the solutions above mentioned. To overcome these troubles additive manufacturing (AM) method, also known as three-dimensional (3D) printing, has carefully been studied with a significant growth over the past 25 years in several areas. AM consist in a layer-by layer builds up of components by the use of powder or wire as a feedstock which is selectively melted by a focused heat source (laser or electron beam) and consolidated in subsequent cooling to form a part. It has been found that under a very narrow range of laser parameters a homogeneous microstructure with minimum area fraction of porosity can be achieved. AM ensures the possibility to repair locally the damaged parts, control of the heat input, more rapid manufacturing, ability to design complex geometry and simultaneously improves the wear characteristics of the element [6]. The extremely high cooling rates and the large thermal gradient of the AM techniques lead to different solidification routes of the available alloys in comparison to the microstructures obtained from classical manufacturing processes. Nowadays, just 50 alloys are commercially available for AM i.e. TiAl6V4, Inconel 718, some stainless steel and AlSi10Mg [7]. The presence of cracks, the difficulty to obtain the alloy as AM feedstock and/or the poorer mechanical properties in comparison to the traditional part are the main problems for which the majority of the alloys used in the industry cannot be additively manufactured. Nevertheless, nowadays the research of new alloys for the AM and even more on the fabrication of alloys or composites, possible only with the AM technologies, remain a necessity and a sensitive topic.

The Laser Cladding (LC) is an AM technology, also known as Direct Metal Deposition, who provides the possibility to feed two different powders into a focused laser beam depositing on a substrate the new material. In this way, it is possible to fabricate Metal Matrix Composites (MMC) composed by a matrix and a reinforcement with different properties. Stainless steel 316L is known as a material with excellent corrosion resistance and widely used in constructions, petrol and chemical (oil and gas) applications, chemical industries and as biomaterial [8]. The weak wear resistance is still the main drawback for this material limiting its use in several applications. The introduction of harder particles as reinforcement could overcome this weakness. In this work, SS316L has been used as matrix whereas tungsten carbide (WC) has been used as reinforcement due to the high chemical affinity, high melting temperature (more than 2200°C) and its well-known hardness. Previous works have already been done regarding 316L+20% (vol.%) of WC [7], whereas in this case the microstructure and the wear behaviour of the 316L+10%(vol.%) of WC were studied. Due to the peculiar features of the microstructure, this material probably exhibits enhanced mechanical properties if compared with pure SS316L. The main purpose of the whole work is based on the comprehension of the different wear phenomena that occur during wear conditions. In order to investigate the wear behaviour, several pin-on-disk test were carried out and after each test Profilometer measurements and Scanning Electron Microscope (SEM) analyses were performed on the post-mortem surfaces to correlate the different wear mechanisms already known in literature with the wear sequence in this material. Furthermore, the microstructure was characterised using Optical Microscopy (OM) and SEM (to study the carbides distribution and the phases formed during solidification). Hardness tests were performed in order to understand the influence of the reinforcement on the mechanical properties.

2. State of the art

In this section a description concerning Additive Manufacturing (AM) techniques with more focus on Laser Cladding (LC) will be given. Furthermore, explanation regarding precursors used to create the samples, metal matrix composite and common wear mechanisms will be also reported in this chapter.

2.1 Additive Manufacturing

Additive Manufacturing (AM) consist in a layer-by layer builds up of components by the use of powder or wire as a feedstock which is selectively melted by a focused heat source (laser or electron beam) and consolidate in subsequent cooling to form a part.

This relatively new processing route can be applied in different fields like automotive, aerospace and medical field [9]. Moreover, this new technique has already replaced the traditional one for production of medical implants, dentures, aircraft and engine parts.

AM has attracted much attention over the past ten years due to its immanent advantages, such as the combination of properties of different types of materials, the possibility to create material with complex design and the short time necessary to the process [6].

Porous structures have been obtained at the beginning of the discovery of AM, but with the technological evolution nowadays it is possible to create a dense part for a number of materials, including steel, aluminium and titanium. The knowledge of the AM process parameters is fundamental to obtain the desired final microstructure and consequently the final macroscopic properties. It has been found that under a very narrow range of laser parameters a homogeneous microstructure with minimum area fraction of porosity can be achieved.

Moreover, Additive Manufacturing is characterised by a complex thermal cycle on a defined volume element of the material. This thermal cycle involves a rapid heating above melting temperature due to the absorption of the energy of the laser (or electron beam) which is converted into heat. A rapid solidification of the molten material after the heat source has moved on and numerous re-heating and re-cooling processes that occur when the following layers are welded and the volume element is still exposed to heat. Hence, many of the AM processes lead to meta-stable microstructures and non-equilibrium compositions of the resulting phases both of which also may vary for each layer of deposited material [6].

Despite diverse naming, the various metal AM processes basically share the same approach: the starting point is a 3D CAD model who is created on a computer, generated by an imaging method or obtained by reverse engineering. The model is virtually sliced into thin layers with a typical layer thickness of 20μm - 1mm [10], depending on the AM process. Based on this data, the physical part is then built by repetitive deposition of single layers and locally melting of the material by a heat source.

The AM processes involve solidification in metals that is more cellular-dendritic rather than the classical columnar- dendritic owned by the casting routes as Y. Lee et al. [11] report. The AM is characterized by high temperature gradient (G) and solidification rate (R) leading to a fine structure as it is shown in Figure 2.1.

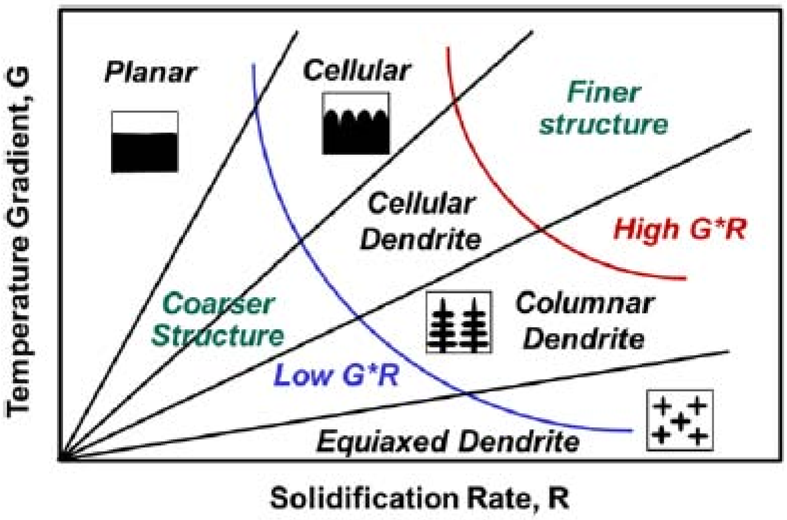

Figure 2.1: Correlation between temperature gradient (G), solidification rate (R) and microstructure for metals [11].

2.1.1 Additive Manufacturing techniques

Nowadays different AM machines are available in order to satisfy the requests of the market. They can be classified for example on basis of the feedstock material, energy source used and the building volume.

Power bed, powder feed and wire feed are the most common systems [12] and they are summarized in the Table 2.1.

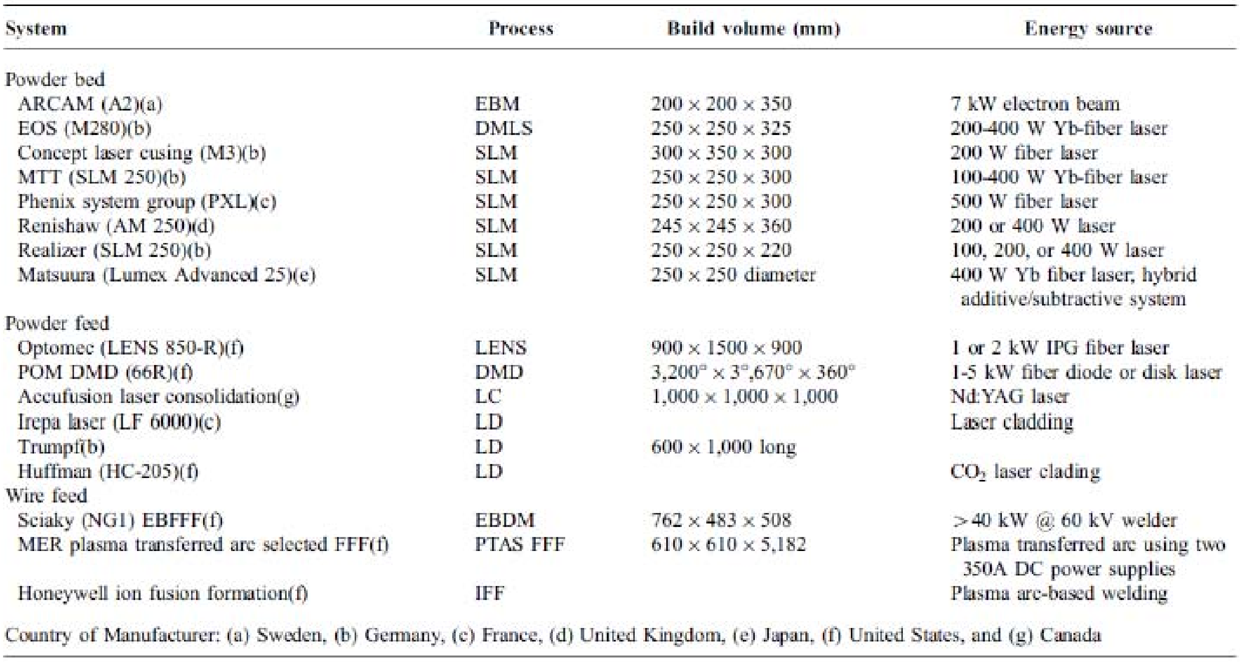

System	Process	Build volume (mm)	Energy source
Powder bed			
ARCAM (A2)(a)	EBM	200 × 200 × 350	7 kW electron beam
EOS (M280)(b)	DMLS	250 × 250 × 325	200-400 W Yb-fiber laser
Concept laser cusing (M3)(b)	SLM	300 × 350 × 300	200 W fiber laser
MTT (SLM 250)(b)	SLM	250 × 250 × 300	100-400 W Yb-fiber laser
Phenix system group (PXL)(c)	SLM	250 × 250 × 300	500 W fiber laser
Renishaw (AM 250)(d)	SLM	245 × 245 × 360	200 or 400 W laser
Realizer (SLM 250)(b)	SLM	250 × 250 × 220	100, 200, or 400 W laser
Matsuura (Lumex Advanced 25)(e)	SLM	250 × 250 diameter	400 W Yb fiber laser, hybrid additive/subtractive system
Powder feed			
Optomec (LENS 850-R)(f)	LENS	900 × 1500 × 900	1 or 2 kW IPG fiber laser
POM DMD (66R)(f)	DMD	3,200° × 3°,670° × 360°	1-5 kW fiber diode or disk laser
Accufusion laser consolidation(g)	LC	1,000 × 1,000 × 1,000	Nd:YAG laser
Irepa laser (LF 6000)(c)	LD		Laser cladding
Trumpf(b)	LD	600 × 1,000 long	
Huffman (HC-205)(f)	LD		CO_2 laser clading
Wire feed			
Sciaky (NG1) EBFFF(f)	EBDM	762 × 483 × 508	>40 kW @ 60 kV welder
MER plasma transferred arc selected FFF(f)	PTAS FFF	610 × 610 × 5,182	Plasma transferred arc using two 350A DC power supplies
Honeywell ion fusion formation(f)	IFF		Plasma arc-based welding

Country of Manufacturer: (a) Sweden, (b) Germany, (c) France, (d) United Kingdom, (e) Japan, (f) United States, and (g) Canada

Table 2.1: Main AM systems and equipment sources [12].

- *Powder bed system:* a thin layer of powder is spread by a coater. It is then scanned by the energy source (laser or electron beam) that melts or sinters the powder in the desired shape controlled by the CAD file (STL). During the second step, the working plate is lowered, another powder layer is spread by the coater and the energy source scans the new deposited powder. The process is repeated until the object, designed with the CAD software, is created. The advantages of this technique are the high resolution, the capability to produce complex lattices and the large range of material [13].

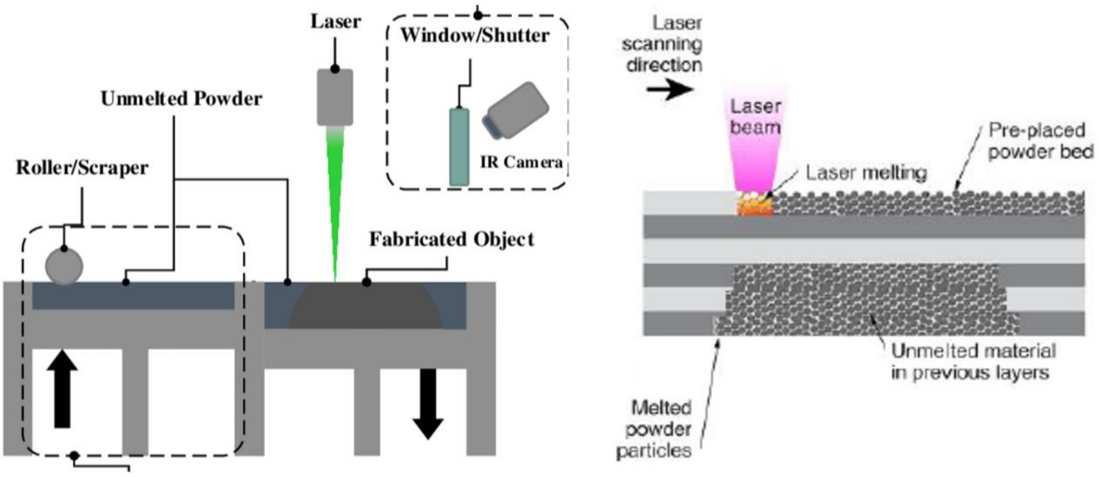

Figure 2.2: Schematic illustration of *power bed system* [13].

- *Powder feed system:* the powders are fed in a nozzle and deposited on the build surface. At the same time, a laser provides heat to melt the powders. These systems are especially used to repair worn or damaged parts. The main advantage of this manufacturing process is the use of many materials and this can be obtained through the additional feeding of a different types of powders. Other two advantages are the possibility to build a large volume and gain a good control of the quantity of the deposited material [9].

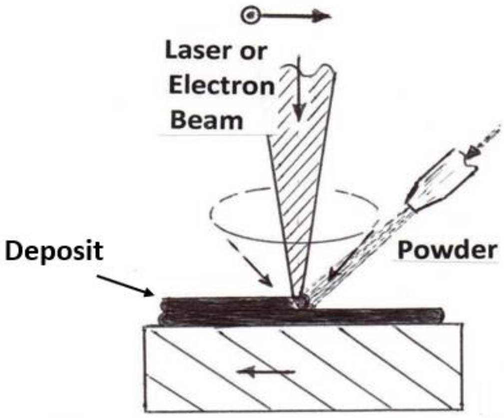

Figure 2.3: Schematic illustration of *power feed system* [9].

- *Wire feed system:* the feedstock material is in form of a wire. The energy source can either be an electron beam, a laser or even a plasma arc. At the beginning, a single track is deposited, then through different sequentially passes the 3D structure is built. This technique allows a high deposition rate of material and it is well suitable for the building of large volumes [14].

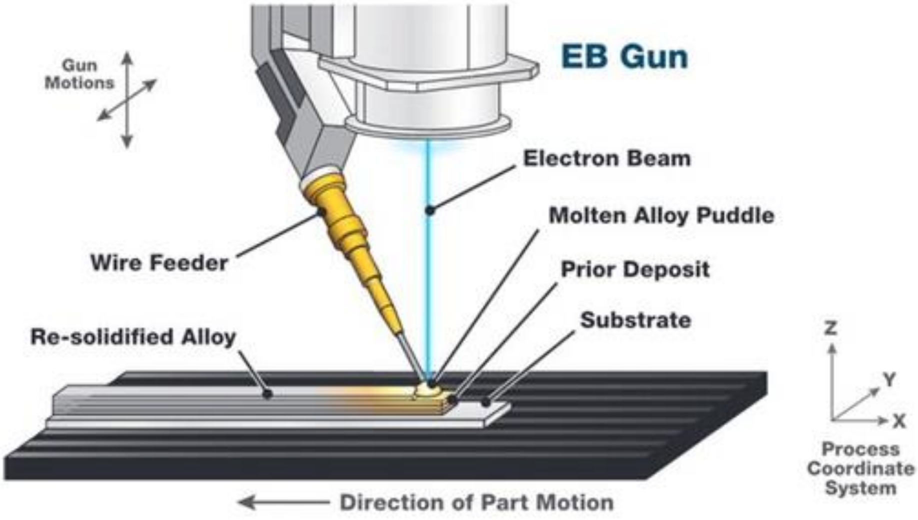

Figure 2.4: Schematic illustration of *wire feed system* [14].

Laser Metal Deposition (LMD) also known as Direct Metal Deposition (DMD), laser deposition welding or laser cladding (LC) [6] is a powder feed system and it was used to produce the SS316L+WC composite.

2.1.2 Laser Cladding (LC)

In Laser Metal Deposition (LMD), also known as laser cladding (LC), a part is built by means of melting a surface and simultaneously applying the metal powder. A laser energy source is utilized to deposit a thin layer of metal onto a substrate in order to reach a pore- and crack-free coating [7]. The melt pool which is typically protected against oxidation by supplying argon or helium is produced by the energy input. Feed rates between 4 g/min and 30 g/min are realized for the deposition of metal powder and several tracks with well define deposition strategy are performed until the final volume is achieved.

One clad track is formed by one scan of the laser beam. Overlapping tracks are made in order to achieve the required final thickness. The thickness of a single deposited layer can vary between 40 μm and 1 mm [10].

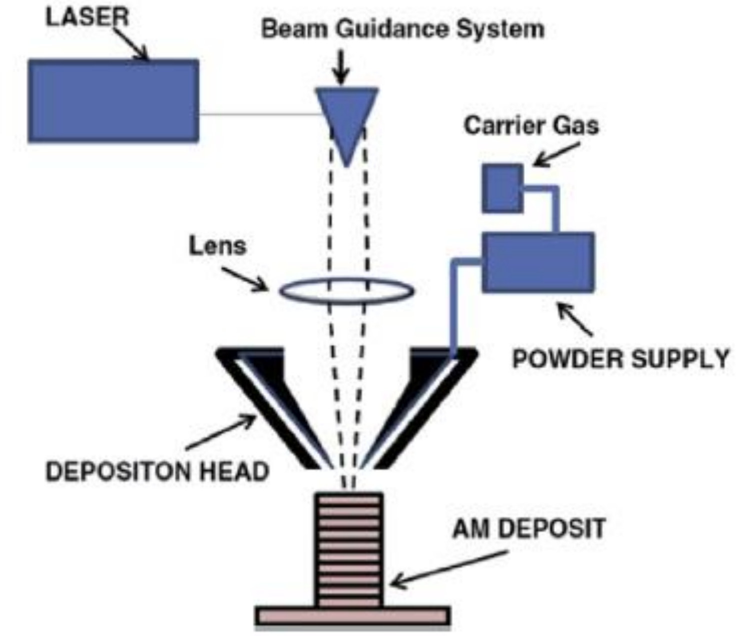

Figure 2.5: Schematics of an LMD set-up [12].

Due to intensive developments, several different systems for LMD evolved. Many studies have been conducted on laser cladding with metal powders, and it is especially beneficial for the low-cost repair of damaged high-value components [15], [16].
Commonly repaired or produced parts are turbine blades, shafts and parts of gear mechanisms mostly made from steels, Ti and its alloys as well as Ni-based super alloys [6]. Laser cladding is a versatile technique, characterized by ultra-fast solidification and cooling rates, thus leading to ultra-fine microstructures resulting in potentially enhanced mechanical properties [17], [18].

2.2 Precursors

Stainless steel 316 low carbon (SS316L) and tungsten carbide (WC) in the form of powders are the materials used in this work and they will be described in this chapter. The high corrosion resistance of the SS316L and the high wear resistance of tungsten carbide may be found in the same material thanks to the use of Laser Cladding technique. The SS316L and WC are the matrix and the reinforcement, respectively.

2.2.1 Stainless steel 316L

High corrosion resistance combine with toughness, good ductility and formability allows a wide use of this materials in many fields such as construction, automotive and medical [19], [20]. Stainless steels are characterised by at least 12% of chromium which provides corrosion resistance due to the formation of chromium oxides layer on the surface of the material in oxidative condition, avoiding the direct contact with the surrounding environment. These oxides present a good adhesion with the material surface, are compact and non-soluble, ensuring a corrosion protection in many environments. If the protective layer breaks down it may be reforms naturally. Different kinds of stainless steels are commercially available i.e. martensitic, ferritic, austenitic, duplex and PH. They differ to each other for the elements and their percentage into the metal. Without consider Fe, C and Cr (always presents) the other elements mainly present are Ni, Mo, Mn, Si, N with different amount of them for different stainless steel. Type 316 stainless steel is one of the most largely utilized by the industries. It is characterised by an austenitic matrix (FCC - face centered cubic) obtained by means austenitizing elements, such as Ni, Mn, and N. Type 316L (where L=low carbon) has lower amount of carbon than type 316, ensuring a better corrosion resistance. In fact, having low amount of carbon, the combination among chromium and carbon to form chromium carbides becomes more difficult, hence the amount of chromium remains always high enough to ensure the formation of protective oxide, enhancing the corrosion resistance. Common chemical composition of 316L is given in Table 2.2 provided by Atlas Steels [21].

Stainless steel		***C***	***Cr***	***Mn***	***Si***	***Mo***	***Ni***	***N***	***P***	***S***	***Fe***
316L	min.	-	16.0	-	-	2.0	10.0	-	-	-	62.0
	max.	0.030	18.0	2.0	0.75	3.0	14.0	0.10	0.045	0.030	72.0

Table 2.2: Typical chemical composition of 316L [21].

2.2.2 Tungsten carbide (WC)

One of the most known and used carbide is tungsten carbide (WC) which shows properties as high melting temperature, high wear resistance, great hardness and brittleness, good chemical resistance. Tungsten carbide exists in nature as Qusongite (WC) even though the starting ore contains low amount of impurities, as chromium [22]. WC and W_2C are the main compounds commercially available and show several structural modifications according to the different amount of carbon and the temperature (Figure 2.6) [23].

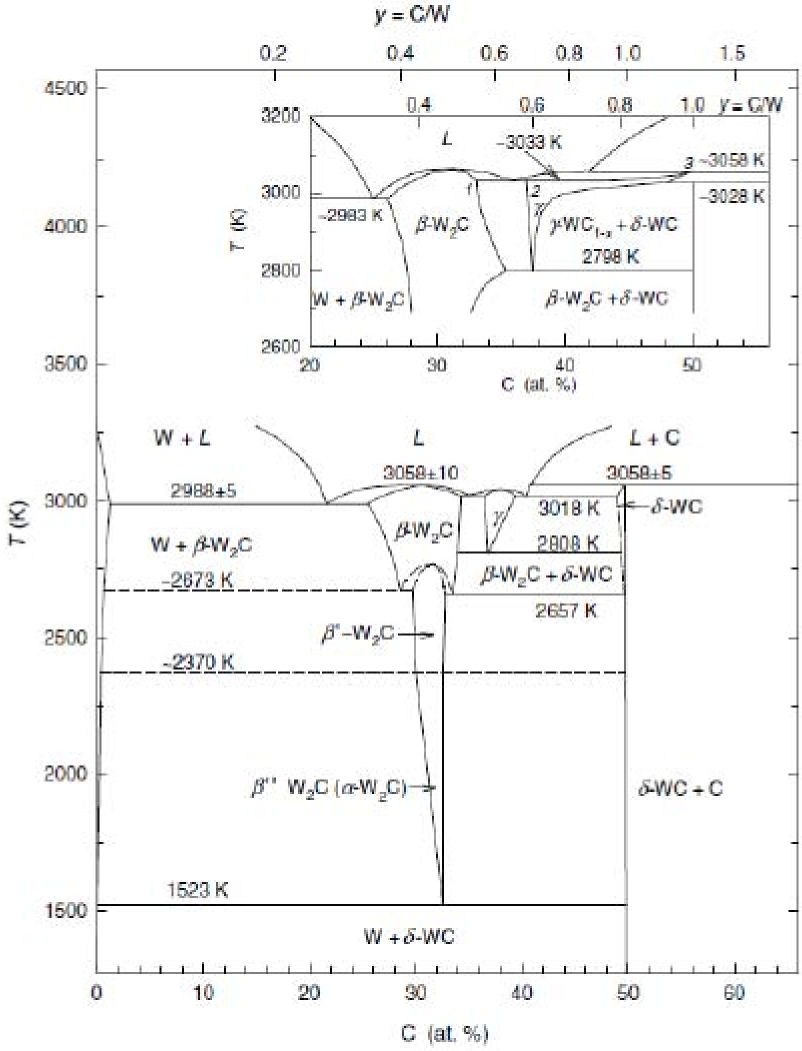

Figure 2.6.: Phase diagram of the W-C system [23].

The γ-WC_{1-x} is stable around 2600°C and in a range between 38-50% of C (at. %) with cubic structure. It is considered as a modification of the WC carbide. Different compositions of tungsten carbides are possible and, as a consequence, different structures may be obtained (Figure 2.7). The various allotropic structures depend also on the temperature used during the formation of carbides.

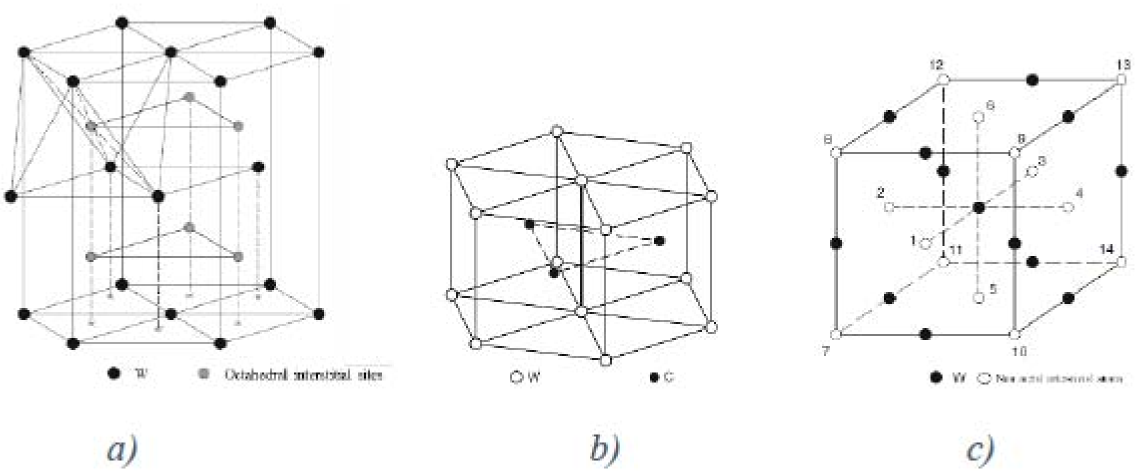

Figure 2.7: Crystallographic structures of Tungsten carbides. a) Hexagonal structure of β-W_2C carbide with low C content. The sites indicated with the ● are randomly occupied by carbon atoms with a probability of $^1/_2$; b) Cubic structure of γ-WC_{1-x} carbide with content of C between 38-50% (at. %); c) Hexagonal structure of δ-WC carbide with high C content [23].

The main properties of tungsten carbide are reported in the Table 2.3.

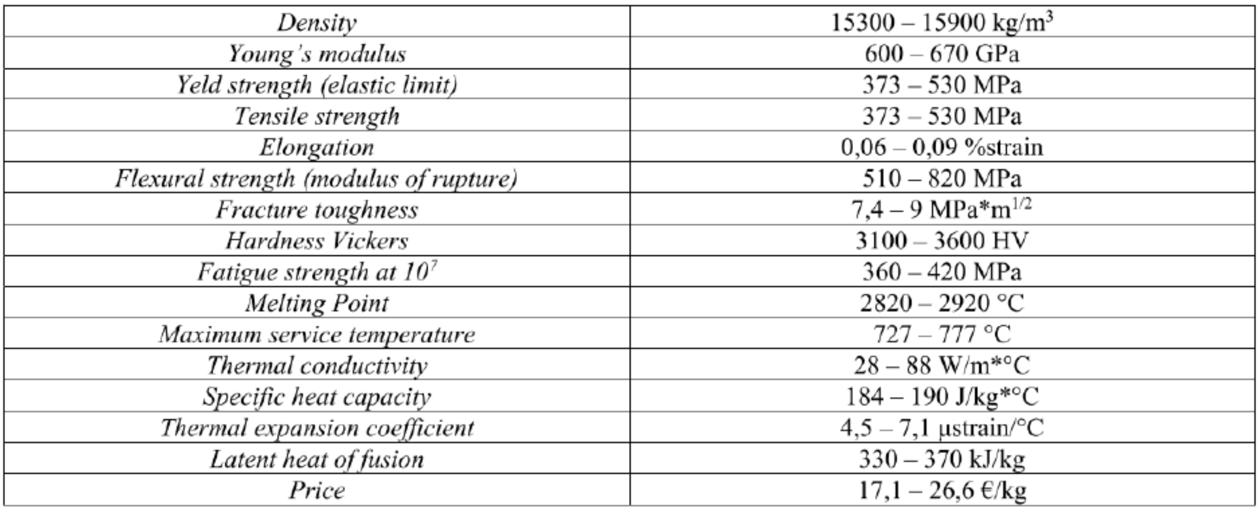

Density	15300 – 15900 kg/m^3
Young's modulus	600 – 670 GPa
Yeld strength (elastic limit)	373 – 530 MPa
Tensile strength	373 – 530 MPa
Elongation	0,06 – 0,09 %strain
Flexural strength (modulus of rupture)	510 – 820 MPa
Fracture toughness	7,4 – 9 MPa*m$^{1/2}$
Hardness Vickers	3100 – 3600 HV
Fatigue strength at 10^7	360 – 420 MPa
Melting Point	2820 – 2920 °C
Maximum service temperature	727 – 777 °C
Thermal conductivity	28 – 88 W/m*°C
Specific heat capacity	184 – 190 J/kg*°C
Thermal expansion coefficient	4,5 – 7,1 µstrain/°C
Latent heat of fusion	330 – 370 kJ/kg
Price	17,1 – 26,6 €/kg

Table 2.3: General characteristic of Tungsten carbide [24].

2.3 Metal matrix composites

In the recent years several researches have been carried out in order to improve common materials available today, especially in automotive, aerospace, marine and nuclear fields. With the technological evolution many new processes have been found out and with them also the possibility to create new materials who are able to meet the requests of the industries. Combination of different types of materials to get news composites is an interesting perspective with the possibility to join different properties in the same material. High temperature resistance, good wear resistance, lightweight, high strength are the most common properties required and one possibility to get them is based on the combination of different materials constituted by matrix and reinforcement. Metallic materials as a matrix are found to be an interesting way to follow since they can respond to the new requests. In literature there are many examples of different combinations i.e. titanium alloys matrix reinforced with titanium borides and carbides [25], aluminium matrix reinforced with silicon carbides [26], and also stainless steel reinforced with titanium borides [27]. In these materials, a ceramic phase is introduced as reinforcement to enhance the properties of the metal matrix due to their high melting temperature, high hardness value, good corrosion and creep resistance [28], [29]. Graphite, silicon carbide, titanium carbide, and tungsten carbide are commonly used in Additive Manufacturing of metal matrix composite [30]. The shape of the reinforcement plays a fundamental role to have isotropic properties and for the feasibility of the AM process [31]. Moreover, the dispersion of the second phase can affect sliding wear by hardening of the matrix and/or by reducing the real contact area between the two sliding bodies. The size of the second phase particles, their mechanical strength and their cohesion with the metallic matrix affect the wear behaviour [32].

2.4 Microstructure of SS316L+WC

In this section the microstructure of the pure SS316L and with the addiction of WC obtained by laser cladding will be reported.

2.4.1 Microstructure of pure SS316L by laser cladding

The 316L stainless steel (SS316L) obtained with traditional manufacturing methods i.e. casting, forging or extrusion [8] is characterised by a combination of good mechanical properties at elevated temperatures, excellent corrosion resistance and good machinability. The mechanical properties of SS316L may be enhanced thanks to laser processes due to their peculiars features i.e. ultra-fast solidification and cooling rates. A thermal history of Laser Cladding was analysed by M.L. Griffith et al. [33] as shown in Figure 2.8 in which may be note as the average temperature during the process tends to increase slightly.

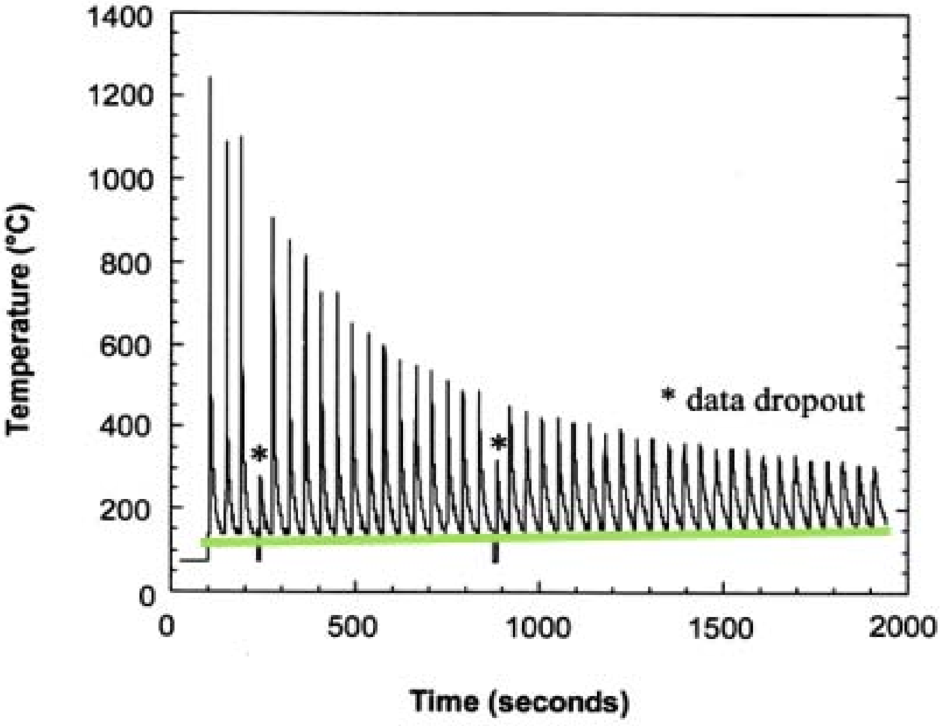

Figure 2.8: Thermal cycle of additive manufacturing process [33].

It is known from other layered structures that a possibility exists of accommodating inclusions at layer interfaces and other defects such as pores or low density regions [34].

Research found that under a very narrow range of laser parameters a homogeneous microstructure with minimum area fraction of porosity can be achieved [35]. The microhardness value was found to vary with laser parameters [34]. From Figure 2.9, it is relevant that average microhardness of the fabricated layers decreases with increase in applied power density. This effect is attributed to coarsening of grains as was evident in detailed microstructural investigation. A close comparison of plot 1 with plot 2 shows that average microhardness value increases with increase in scan speed. With increasing the scan speed, due to a shorter time of interaction a low energy is supplied during melting resulting in refinement of grains, and hence an increase in average microhardness [35].

From the variation of microhardness with laser parameters it may be concluded that hardening of the formed parts is mainly because of grain refinement and for an improved microhardness a low power and high scan speed combinations should be chosen.

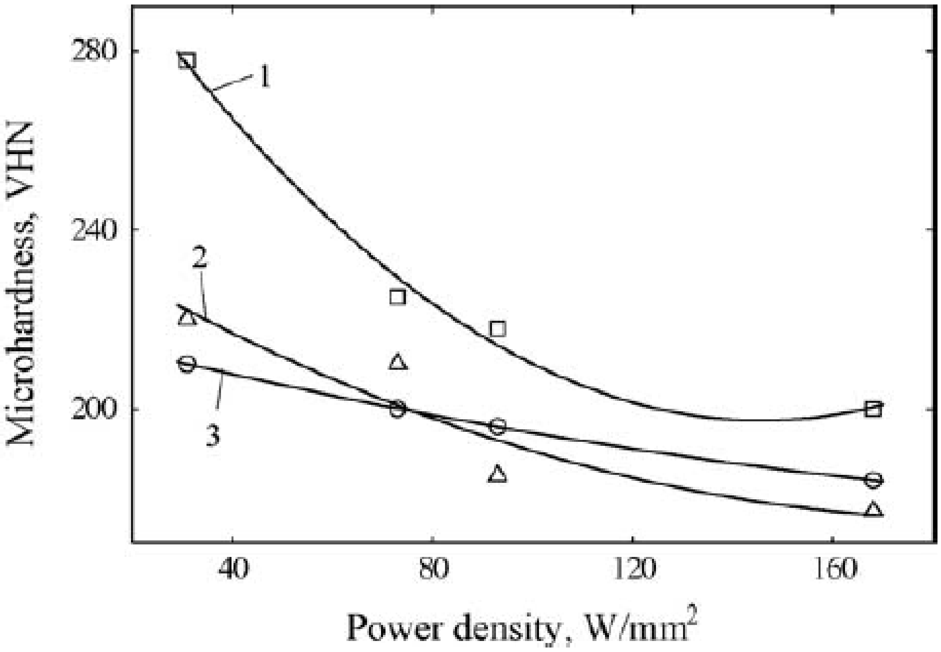

Figure 2.9: Variation of average microhardness with applied power density for laser assisted fabricated AISI 316L stainless steel lased with a (1) scan speed of 5 mm/s, powder feed rate of 203 mg/s; (2) scan speed of 2.5 mm/s, powder feed rate of 203 mg/s and (3) scan speed of 2.5 mm/s, powder feed rate of 136 mg/s, respectively [35].

Moreover, it was found that the morphology of the microstructure depends on the laser parameters, particularly the scan speed [8].

The microstructure and properties of SS316L obtained by laser cladding are expected to be different from the conventional SS316L grade because of the rapid melting and solidification process involved, leading to out-of-equilibrium microstructures [18], [34]. Columnar grains are present together with the formation of a characteristic intragranular cellular segregation network microstructure (Figure 2.10 a)) which contribute to the increase of yield strength without losing ductility. The intragranular cellular segregation network structure (cellular structure in short in the following text) exists in every columnar grain and has a cell size between 0.5 and 1 mm [34]. The observed cellular structure is formed because of the high cooling speed and high level of non-equilibrium conditions achieved during the process. The shape of the cellular structure could be seen as equiaxed or bar-like depending on the growth direction of the larger columnar grains containing them, as seen in Figure 2.10 b). Therefore, the 3D morphology of the cellular structure is well aligned in each columnar grain along the longitude direction with square, pentagon or hexagon shape seen in the transverse direction [34].

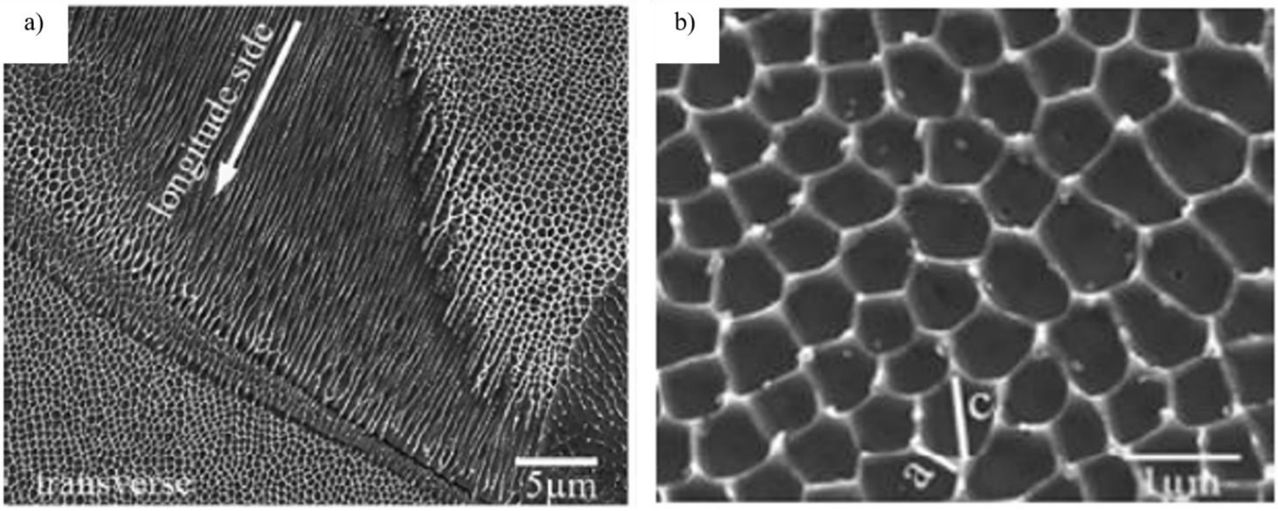

Figure 2.10: a) The SEM images of the as-built sample revealing the intragranular cellular structure; b) transverse sub-grain cell morphology [34].

Moreover, formation of several HAZ (heat affected zone) between the last and the previous layer deposited are present. These reheating modify the microstructure and the cell size [7].

2.4.2 Microstructure of SS316L+WC by laser cladding

An important characteristic of laser cladding is that the metallic melt pools cool down and solidify very rapidly, thus producing strongly out-of-equilibrium microstructures [18] together with the addiction of tungsten carbide as reinforcement for the matrix lead to obtain exceptional mechanical properties. Due to the very high temperature achieved during the process, the WC are partially or completely dissolved enriching the matrix (austenite) of these two elements. Nearby of the partially dissolved carbides the composition presents a greater amount of tungsten if compared far from the undissolved carbides. The remaining undissolved carbides act as a nuclei for the solidification [36]. Also the presence of different types of carbides are identified close to the giant WC and far from them. The interaction between the liquid metal with the WC during deposition leads to several consequences who characterise this composite and they will be discussed in the sections 4.1 and 5.2.

2.5 Common wear mechanisms

Different wear mechanisms leading to friction are briefly described in the following subchapter.

Adhesive wear

Adhesive wear occurs when the materials between the two contact surfaces have a high mutual chemical compatibility [37] and the two relative surfaces are completely free of contaminations. Typical ***"stick-slip"*** marks are associated with adhesive wear [38]. Passive films, oxidation and lubricants may reduce the adhesion among the surfaces due to the decreases of real contact area. Adhesive wear is based on ***electron transfer*** leading to formation of bonds [39].

Once the two surfaces are in direct contact it may occur material transfer from the weaker to the harder material.

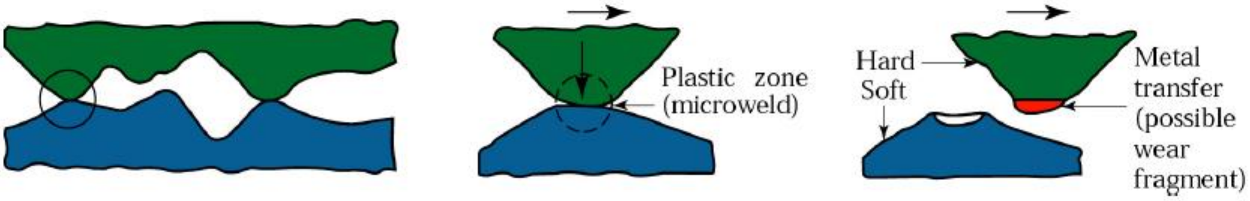

Figure 2.11: Schematic illustration of two contacting asperities, adhesion between two asperities, and formation of a wear particle [39].

For example, adhesion phenomenon among ceramic material with high amount of oxygen (i.e. alumina) and one metallic material may takes place due to the formation of bonds between oxygen atoms and the elements of the metal, usually resulting in a transfer from the metal to the ceramic material.

When adhesion taking place also brittle fractures coming from weaker asperities may occur bringing to plate-like wear debris particles. The particles can grow till they reach a critical size, then they detach from the two-contact surface.

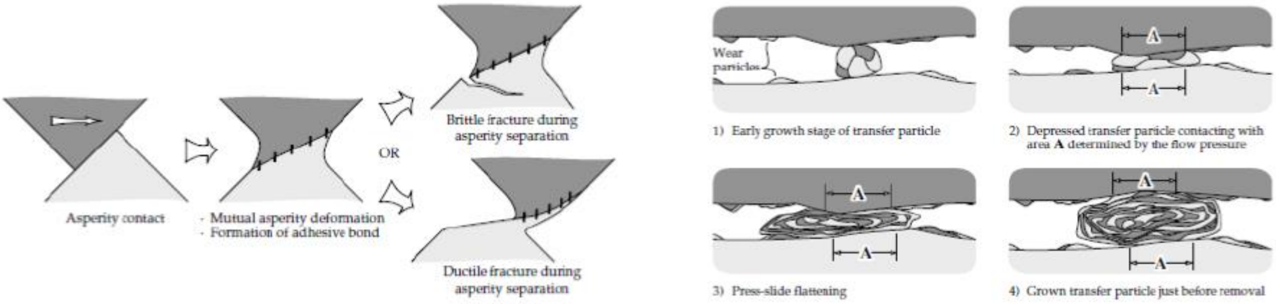

Figure 2.12: Schematic illustration of the adhesive wear process bond formation and two alternative models of fracture (left side); possible mechanism of wear debris formation due to adhesive wear (right side) [39].

Oxidative wear

The oxidative wear mechanism requires presence of oxygen in the atmosphere, i.e. in contact with air, leading to the formation of ***oxide layer*** on the sliding metal surface. Since the oxidative wear phenomenon is a thermally activated process, the formation of ***hot-spot*** temperature (several hundreds) in real contact areas lead to production of oxides in those points [32]. The composition of the oxide depends on the hot-spot temperature. The rate of the oxide film growth may be described by Arrhenius law:

$$k = A exp(-\frac{Q}{RT})$$

where k is the rate constant for oxide film growth, Q is the activation energy, R is the universal gas constant, and T is the interface temperature [40]. From the Arrhenius relationship it is clear as every increase in temperature result to increases the rate of oxide film growth, according to what mentioned before.

Oxide formation usually has a beneficial character as wear rate may be reduced [41]. The oxide growth in height and it is spread over the whole area. Beyond a critical oxide film thickness (δ =1-2µm) it breaks up to form wear debris. The detached oxide particles can remain trapped within the contact zone as abrasive particles [42]. After that, it is possible to have a direct contact between particles and the counter-body and the re-formation of oxide layer is hindered by the collision of them. The size of the hard second-phase particles of the material (d) plays a significant role [32]:

- if $d \leq \delta$ the second phase particles can be entirely included in the oxide layer. When the oxide breaks up the hard particles slide away together with oxide to form wear debris.

- if $\delta < d < 3\delta$ a small quantity of the second phase particles may be removed together with the oxide.

- if $d >> \delta$ the protection against oxidative wear is strong because when the oxide layer breaks up, the hard second-phase particles remain embedded in the matrix.

Under low sliding speed the heat generated by the slipping surfaces is not so relevant, therefore a thin oxide layer forms on the surface, but its growth is limited by slow diffusion. With the proceeding of the sliding, the thin layer fractures and the metallic wear debris oxidize while rolling between the sliding contacts. This leads to the formation of a compact layer of mixed wear debris.

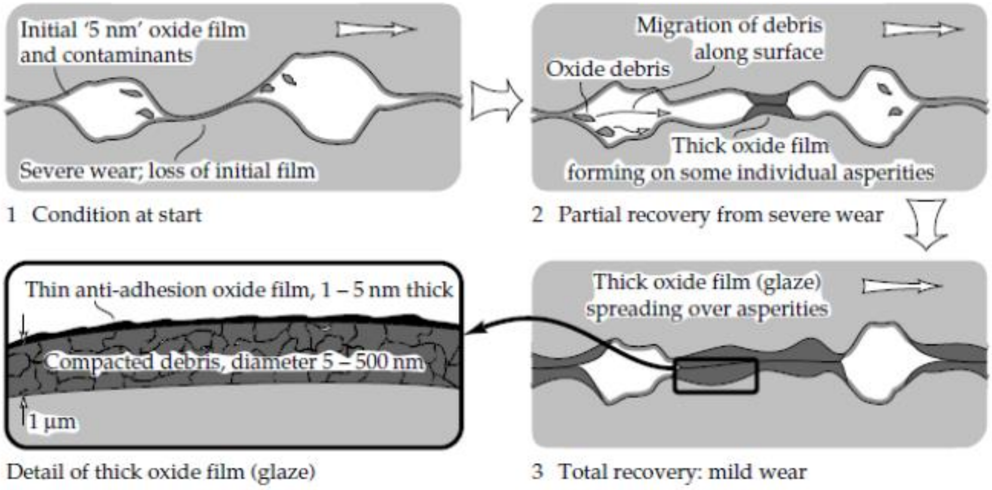

***Figure 2.13*:** Schematic illustration of the oxidative wear process at slow sliding speed [39].

The mechanical behaviour of the second-phase particles sliding against the counter-body governs the wear mechanism (even though also the properties of the matrix are important concerning wear behaviour). The **s**ize, mechanical strength and cohesion with the matrix of the second-phase particles are fundamental parameters and if they are optimized its breaking and detachment from the matrix are very difficult [32].

Abrasive wear

The abrasive wear occurs when ***harder particles roll*** on the softer material surface causing deformation. There are several mechanisms of abrasive wear such as cutting, ploughing, grain pull out, fatigue, and brittle fracture. Considering cutting, hard particles are imbedded in the softer material and it is dragged bringing to plastic deformation. Ploughing is a similar phenomenon as shown in Figure 2.14, but plastic displacement of material occurs around the abrasive edges. At the same time, some material is built up in front of the particle.

Grain pull out is a relatively rare form of wear. It is more common in ceramics, but it may occur also in metallic materials if brittle phases form at the grain boundaries.

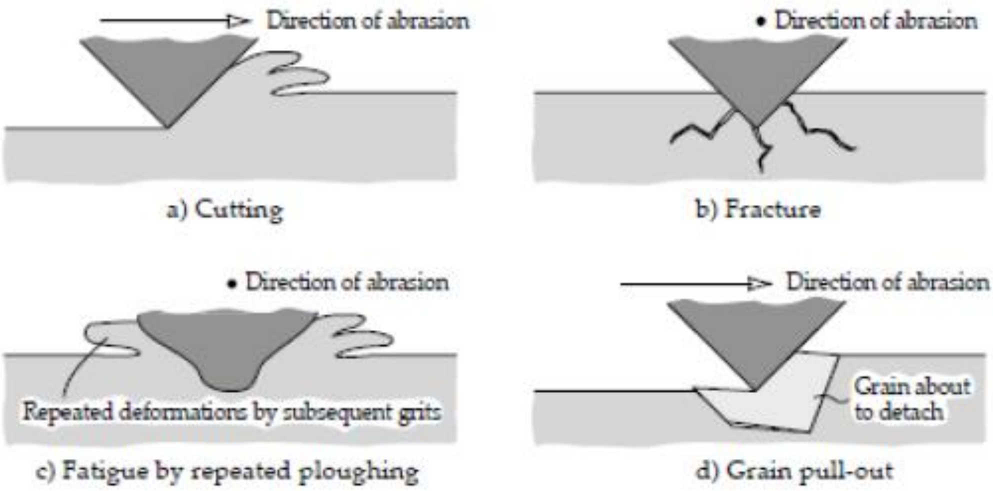

Figure 2.14: Schematic of mechanisms of abrasive wear [39].

Abrasive wear may occur by ***two-body*** or ***three-body abrasion*** (Figure 2.15). The two-body abrasion takes place when the grains are fixed in a rigid setting and they are sliding against a softer material. The pressure generate by counter-body is mainly supported by the hard particles embedded in a matrix (i.e. carbides). As a result, the pressure over hard particles on the tested surface tends to fracture the carbides into micrometric particles and they promote the abrasion phenomenon [43]. The fractured microparticles mixed with wear debris change the wear behaviour from two-body abrasion to the three-body abrasion process [37]. This leads to the presence of grooves and/or microgrooves, ridges and scratches deriving by micro-cutting as it is schematically represented.

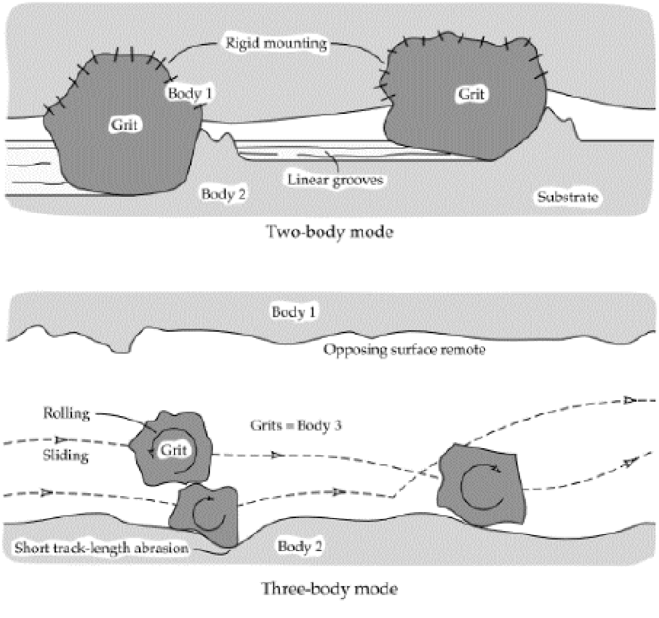

Figure 2.15: Schematic of mechanisms of abrasive wear in the two-body and three-body configuration [39].

Fatigue Wear and Delamination

Delamination wear phenomenon was proposed by A. Kapoor et al. [44] taking into account the crack growth leading to deformed plastic region. This type of wear can be associated like a competitive fracture process between two different mechanisms: - low cycle fatigue (LFC); - ratcheting failure (RF). The high plastic deformation and high stress bring to a short cyclic crack growth in the LFC mechanism. In the RF, the strain accumulation due to plastic deformation from cyclic stresses can grows till a critical threshold. When this threshold is reached, ductile failure occurs by exceeding the strain to failure limit. According to A. Kapoor the LCF and RF processes take place independently, but simultaneously. In this model, the surface region of the sliding contact is considered formed by several layers. The strain accumulation occurs in each layer during cyclic stressing if the applied shear stress exceeds the effective shear strength of the material within the layer. When strain accumulation and/or crack growth reach a critical level, the closest layer to the surface of the material will pull out due to delamination. Hence, the next layer is exposed and the process is cyclically repeated, causing the movement of subsurface layers towards the surface [44].

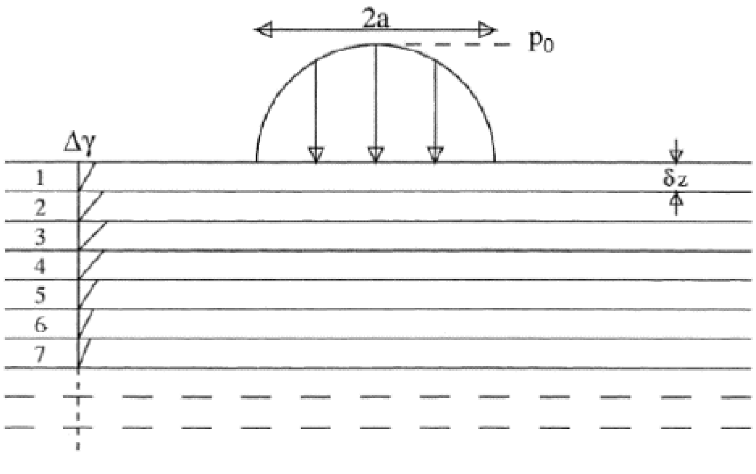

Figure 2.16: Schematic illustration of the layers of strain accumulation in the delamination wear. Δγ is the strain accumulation increment, δz is the thickness of each tribolayer, a is the radius of circular contact area for sliding contact of a sphere on a flat surface, p_0 is the Hertzian contact pressure [44].

3. Experimental methods

A brief description concerning the powders, the cladding process and the instruments used to characterize the SS316L+WC10%vol composite is given in this chapter.

3.1 Precursors powders composition

SS316L and tungsten carbide powders used to create the samples were produced by Höganäs [45], a Swedish company. Their chemical compositions are reported in Table 3.1 and Table 3.2.

	C	***Fe***	***Cr***	***Ni***	***Mo***	***Mn***	***Si***
%wt	<0.03	Bal.	16.0-18.0	10.0-14.0	2.0-3.0	1.0-2.0	<1.0

Table 3.1: Chemical composition of SS316L powder [45].

	C	***Fe***	***W***
%wt	3.5-4.0	<0.5	Bal.

Table 3.2: Chemical composition of WC powder [45].

The shape of the particles is circular avoiding the possibility to damage the pipes and the nozzle of the Laser Cladding machine. Another reason why is important to have circular shape powders is due to the possibility to have abrasion phenomenon which can occurs if the particles have irregular edge-shape.

Concerning the size of the SS316L powders it varies from 45 to 150μm, whereas the dimension of the tungsten carbide particles varies from 45 to 180μm. The size of the powder is an important parameter because if the powder particles are too small, they may form clusters increasing the local pressure in the pipes; at the same time, the particles must not be too big in order to avoid obstructions in the pipes and nozzle.

3.2 Samples fabrication

The machine used for the fabrication of the samples is a Cladding machine DUOCLAD VI LF 2000 shown in Figure 3.1. Each sample was produced by Tommaso Maurizi-Enrici at Sirris [46].

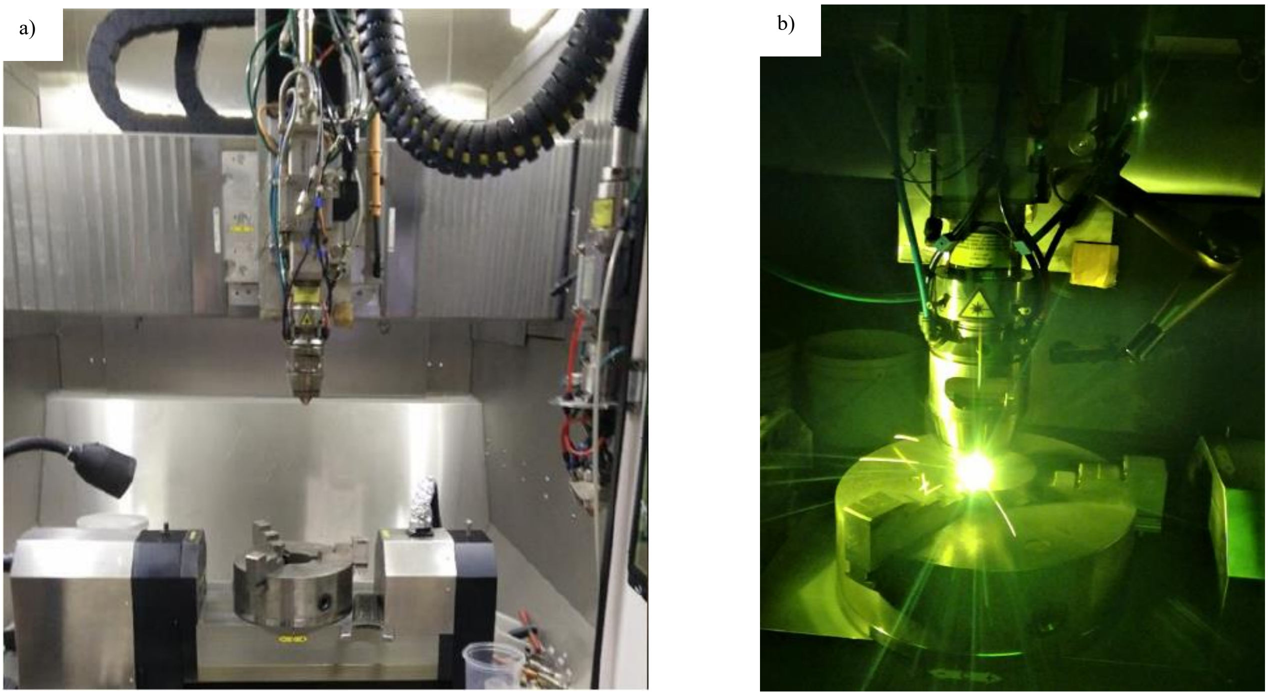

Figure 3.1: a) Internal view of Laser Cladding machine; b) Laser cladding machine during deposition [46].

A dispenser is used in order to store the powders necessary to the production of the samples. A continuous feed is provided by a turntable who allows to maintain constant the weight feed rate of powder (g/min). At the same time, the dispenser ensures a good mixing during the displacement of the raw material from the turntable to the pipe. The day before performing the deposition the powders are placed and then kept in the dispenser in order to remove the air present between the precursors, achieving a better compaction. The turntable is connected with pipes through which the powders can pass. The pipes are link with a nozzle from which the raw materials are ejected with a laser to create the material. During all these steps a constant flux of Argon is provided for the transport of the powders and to avoid oxidation during the deposition. All the machine parameters are controlled digitally. Based on Daniele Mario's Master thesis [7] the bi-directional deposition strategy is the method chosen to create the samples as schematically shown in Figure 3.2.

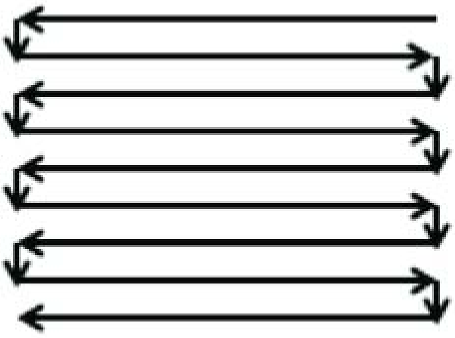

Figure 3.2: Direction followed by laser during deposition to create one layer [7].

Only the sample W10.04 was used to study the microstructure, distribution of carbides and hardness on the cross section, whereas the samples W10.12, W10.13 and W10.14 were used to performed tribometer tests and their relative characterization by means Profilometer and SEM. Each sample was prepared using stainless steel 316 low carbon and tungsten carbides powders deposited on stainless steel substrate with Laser Cladding technique (LC). The general characteristics of the samples are summarized in the Table 3.3. Some images of the samples obtained are represented in Figure 3.3 showing as the deposit have a parallelepiped shape, a square base with side of 35mm and height close to 14mm.

Name	*316L [g/min]*	*WC [g/min]*	*Total weight feed [g/min]*	*Volumetric percentage of WC in SS316L*	*Height [mm]*
W 10.04	15.7	4.3	20	11.7	13.2
W 10.12	14.7	3.5	18.2	10.4	12.9
W 10.13	14.8	3.3	18.1	9.7	12.5
W 10.14	14.8	3.2	18	9.5	12.8

Table 3.3: General parameters and characteristics of the samples.

Figure 3.3.: Different views of the same sample with powder deposition on stainless steel substrate obtained by Laser Cladding process.

3.3 Microstructural characterization

The Spark Erosion machine was used to cut the W 10.04 sample considered for the microstructural characterization. Only the cross section was taken into account since it was noted to be the best representative part of the material in the previous studies [7]. As may be seen in Figure 3.5, the sample was embedded in a Bakelite cylinder using a STRUERS Citopress-1 (Figure 3.4 a)). Surface preparation to get a clean and plane surface was needed before the analysis with optical and electron microscope. Polishing was carried out thanks to STRUERS Tegramin-30 (Figure 3.4 b)) using a disc of 300mm of diameter. An additional treatment was performed with the PRESI vibrometer to improve as much as possible the surface quality. In this instrument, a colloidal solution containing silica with micrometric size acts as cleaning agent for the micro-impurities.

a) b)

Figure 3.4: a) STRUERS Citopress-1 used to the polymerization of bakelite around the sample; b) STRUERS Tegramin-30 to polishing the sample surface before the analysis.

a) b)

Figure 3.5: a) Sample W10.04 cut for cross section analysis; b) Cross section of W10.04 sample embedded into bakelite.

3.3.1 Optical microscope and Stream Motion software

The cross section of W10.04 sample was analysed by means of an Olympus BX60 microscope (Figure 3.6) in order to have a preliminary idea regarding the microstructure of this metallic material composite. Light etching with a solution of 15 ml of HCl, 5 ml of HNO_3 and 80 ml of H_2O was carried out in order to better emphasise the different types of microstructures: cellular, dendritic, rosette-like.

The surface was cleaned with ethanol before analysis to remove every impurity. Magnification of 2.5x, 5x, 10x were used. The images obtained by OM will be shown in chapter 4.

Figure 3.6: Olympus BX60 Microscope

Starting from the image taken at magnification 2.5x with optical microscope it was possible to detect the carbides present in the cross section thanks to Stream Motion software. Distribution map, frequency and size distribution of carbides were found using the Excel file data derived by the detection of carbides. Even small points who could not be associated to carbides were detected, hence, rearrangement of Excel file was necessary to get more accuracy.

3.3.2 Scanning Electron Microscope

Furthers analysis were performed using Phillips XL30 FEG-ESEM Scanning Electron Microscope, as shown in Figure 3.7. The sample preparation for the Electron microscope is the same used for the Optical microscope already previously explained (subchapter 3.3). Several images were taken in different modes. The SEM analysis was carried out to have a general idea concerning the different types of carbides and microstructures present. Energy Dispersive Spectrometry (EDS) mode was used to get local chemical composition along a profile. Electron Back Scattered Diffraction (EBSD) mode was useful to recognise the different crystallographic lattices.

Figure 3.7: Phillips XL30 FEG-ESEM

SEM was also used to analyse the track of the post-mortem samples (W10.12, W10.13, W10.14) after the wear test providing many information i.e. presence of oxides, carbides breakdown, generation of grooves, presence of debris from the counter-body. Furthers analysis of the post-mortem samples were carried out on a transverse cross-section.

3.4 Macro-hardness

Two Vickers hardness tests were carried out on the cross section of W10.05 and W10.04 samples, whereas the hardness test on pure SS316L performed in the previous work [7] was used as reference. The EMCO M1C 010 digital low-load hardness machine (Figure 3.8) was used to perform these tests; different applied forces and trials may be carried out i.e. Vickers. The tests were carried out considering half of the cross section for both W10.05 and W10.04 samples. After each indentation, the sample is displaced manually by 1mm. For each indentation the software of the machine measures the dimension of the imprint left by penetrator and provides the Vickers hardness value.

Figure 3.8: EMCO M1C 010 hardness machine.

3.5 Tribometer

Prior to the tribometer tests, the deposited material was cut and polished to obtain a suitable surfaces for the tests. Spark Erosion machine was used to cut the samples, then, the samples were ground. Finally, the surface was cleaned with methanol. The system for the designation of the samples is illustrated in Figure 3.9. It includes in the following order:

- the name of the sample (W10.xx; where 10 = 10% vol of WC and xx = number of the sample);
- F or H in capital letter (where F=Feet, lower part, starting from the substrate to the core (zone B in Figure 3.9 a)); H=Head, upper part, starting from the core to the top (zone A in Figure 3.9 a));
- distance from the substrate at which the surface was obtained (1.3 or 6.3 or 11.3 mm).

Example: W10.12 F6.3 = sample with 10% vol of WC number 12, surface at 6.3 mm far from the substrate.

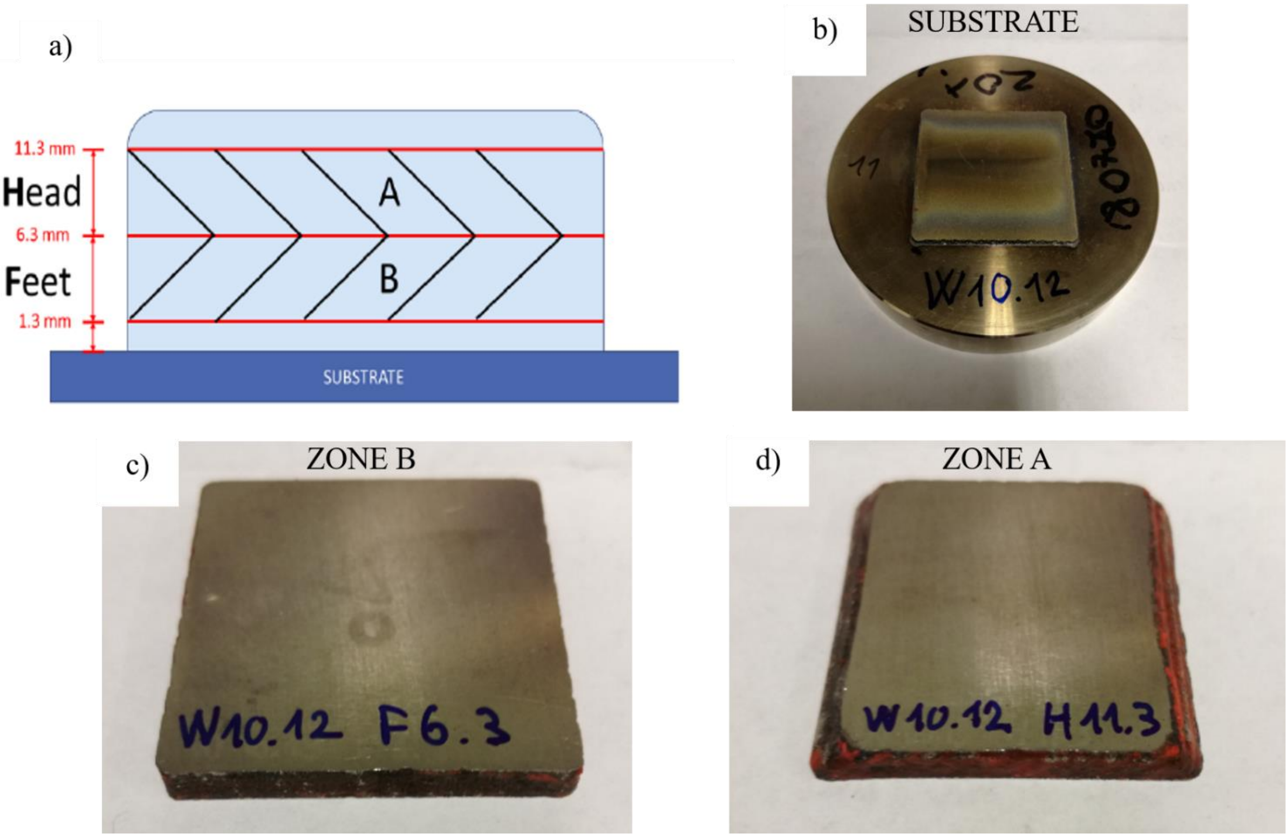

Figure 3.9*:* a) cutting position***;*** b) substrate of stainless steel and base of the deposit cut of W10.12 sample; c) feet 6.3 surface of W10.12 sample (part B shown in Figure 3.9 a)); d) head 11.3 surface of W10.12 sample (part A shown in Figure 3.9 a)).

High Temperature Tribometer 01-04611 provided by CSM Instruments SA was used to perform wear tests on different samples surfaces as summarized in Table 3.4. Based on Daniele Mario's Master thesis [7] the parameters set during each test was always the same except for the *"stop condition"* parameter.

Name	*Position*	*Speed [cm/s]*	*Load [N]*	*Radius [mm]*	*Stop condition [Cycles]*
W 10.12	F 1.3	10	10	8	22000
	F 6.3	10	10	8	2000
	F 6.3	10	10	11	7500
	H 6.3	10	10	11	12000
	H 6.3	10	10	8	5500
	H 11.3	10	10	8	22000
W 10.13	F 1.3	10	10	8	22000
	F 6.3	10	10	8	22000
	H 6.3	10	10	8	30000
	H 11.3	10	10	8	22000
W 10.14	F 6.3	10	10	11	22000
	H 6.3	10	10	11	16000

Table 3.4: Initial parameters setting and samples surfaces used.

Table 3.4 represent the name and the surfaces of the samples on which the tribometer test was carried out. Only in the W10.12 sample two tribometer tests were performed on the same surfaces (surface F 6.3 with 11 and 8mm radius, surface H 6.3 with 11 and 8mm radius) setting different radius of the track,11mm and 8mm respectively.

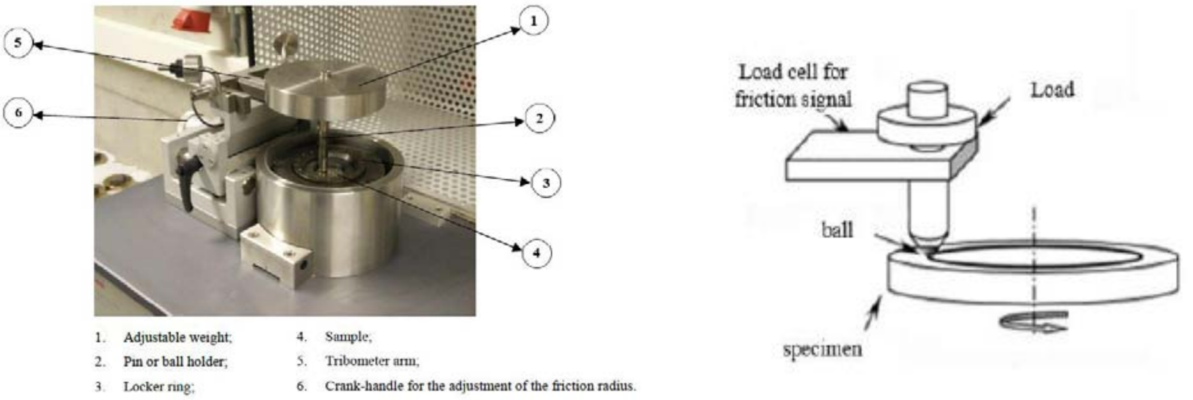

Figure 3.10: Illustration of classic pin-on-disk tester

Alumina balls (Al_2O_3) with 3mm of radius were used for the tests as counter body of the pin which is in direct contact with the sample during the test. The pin holder is made of a base of stainless steel with the extreme part in Inconel 600 [47], and it is fixed by the arm perpendicularly to the sample surface.

As the disk rotates, the resulting frictional forces acting between the pin and the disk are measured by very small deflections using a LVDT sensor. Wear coefficient for the pin and the sample is calculated automatically as well as the coefficient of friction (COF), penetration depth and number of cycles.

3.6 Profilometer

After each tribometer test the surface of the sample and the alumina ball were cleaned with ethanol and analysed using Alicona InfiniteFocus G5 machine (Figure 3.11). The instrument provides several information like worn volume of the whole wear track, width of the track, worn depth of alumina ball, presence of carbides on the track surface. To get the worn volume of alumina ball it is necessary to have its worn depth. This data is provided directly by the instrument. The radius of the alumina ball remained always the same. With these information using formula (1) the worn volume of the alumina ball is calculated.

$$V = \pi h^2 \left(r - \frac{h}{3} \right) \tag{1}$$

Where: V = worn volume of alumina ball [mm^3];

h = worn ball depth of alumina ball [mm];

r = 3mm (radius of alumina ball).

Figure 3.11: Alicona InfiniteFocus G5 profilometer [48].

This machine uses a non-contact, optical, three-dimensional measurement principle based on Focus-Variation. Focus-Variation combines the small depth of focus of an optical system with vertical scanning to provide topographical and color information from the variation of focus itself. The main component of the system is a precision optics containing various lens systems that can be equipped with different objectives, allowing measurements with different resolution [48]. The instrument magnification is up to 100x. For the analysis performed in this work the 5x, the 10x and the 20x magnifications were used. Some difficulties were found during the analysis of alumina ball. Since the profilometer projects light on the object to perform the analysis and since the not-consumed ball surface is white, the acquisition of image is impaired due to the highly reflective surface.

4. Results

4.1 Microstructural characterization of the cross section

Different techniques were used to characterize the particular microstructure of SS316L + WC 10%vol composite obtained by cladding process. Optical Microscope (OM) and Scanning Electron Microscope with different detectors i.e. Energy-dispersive X-ray spectroscopy (EDS, to analyse local chemical composition), electron backscattered diffraction (EBSD, to identify the crystallographic structure of the carbides), secondary electrons (SE, to analyse the tracks after wear test) and BSE mode were used on this metallic material composite and the results are explained in this chapter.

4.1.1 Optical Microscopy

A general overview of the cross section derived by optical microscopy is shown in Figure 4.1. Many carbides are spread in the matrix and their distribution map of W 10.04 sample has been successfully obtained by means of OM analysis using Stream Motion software.

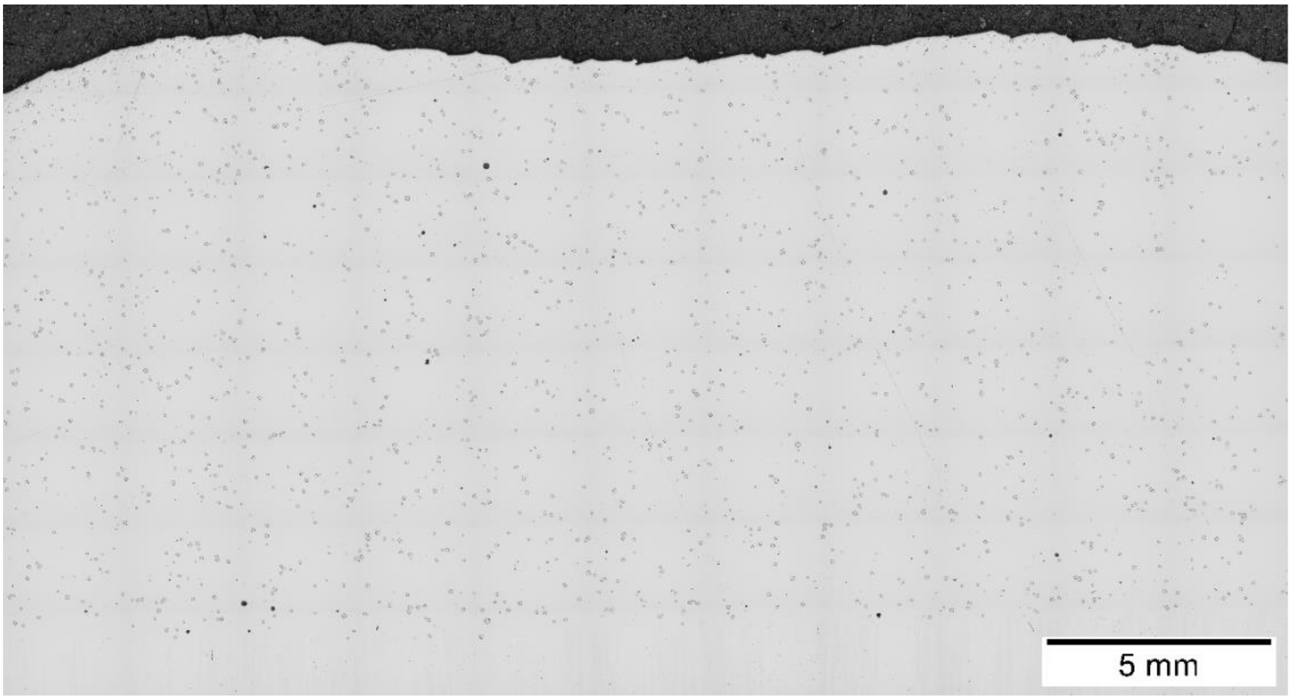

Figure 4.1: Cross section overview obtained by optical microscopy.

In Figure 4.2 are represented two OM images at high magnification. Cellular, dendritic and columnar microstructures may be recognised. As it is shown in Figure 4.2 a), the cellular microstructure prevails, even though is not unique one (Figure 4.2 b)). Also, the spherical shape of the carbides can be noted.

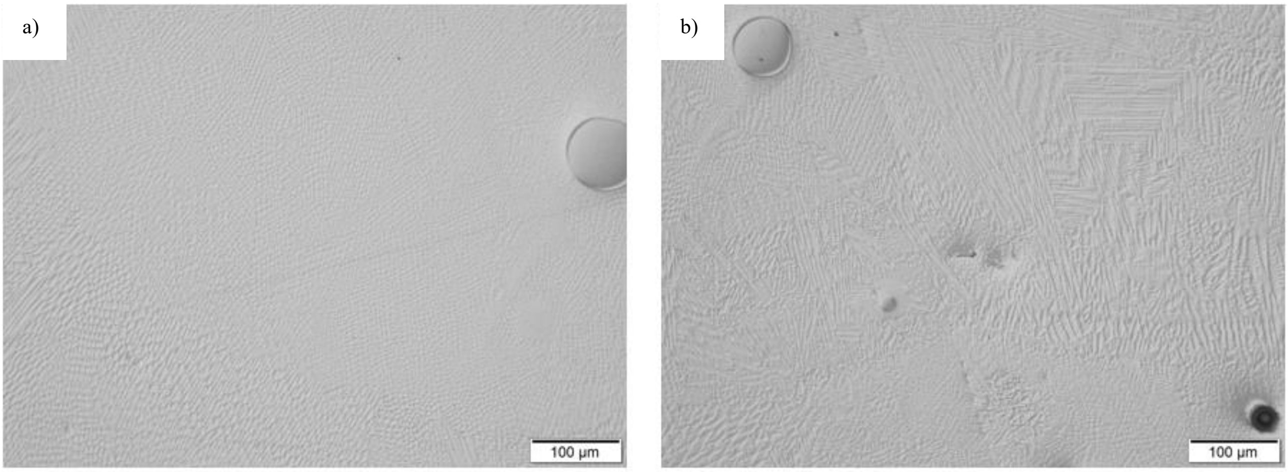

Figure 4.2 : Images of the cross section after etching derived by optical microscope: spherical carbides and mainly cellular microstructure are recognised.

Based on Figure 4.1, the Stream Motion software allows to get a rough estimation of the dimension and position of carbides, as Figure 4.3 shows. It is clear as the carbides have been well detected.

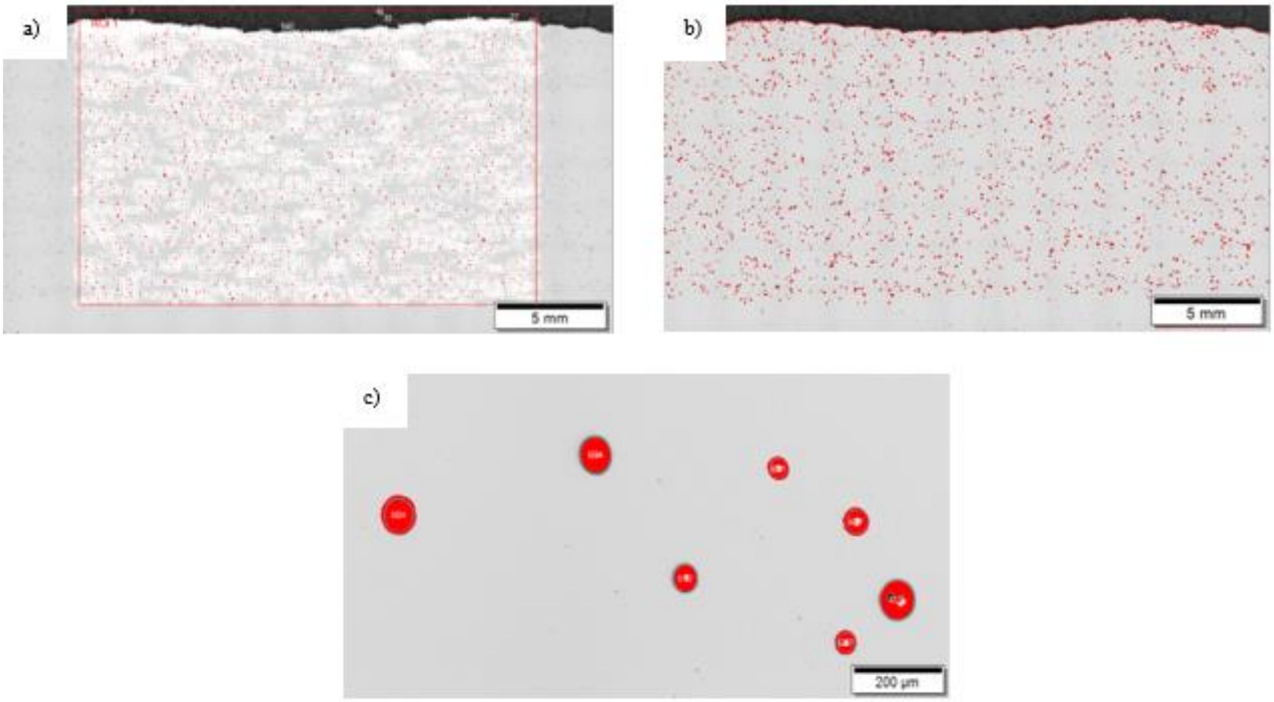

Figure 4.3: Cross section overview and higher magnification of it by Stream Motion software. Carbides with different size are clearly recognise in the sample.

Figure 4.3 a) exhibits the detected zone chosen, whereas Figure 4.3 b) represent a zoom in of the larger zone of Figure 4.3 a). Through the use of Stream Motion software the Excel file describing the map distribution of carbides was obtained in order to have a full comprehension concerning position and size of carbides in the matrix. Figure 4.3 c) at higher magnification emphasizes the different size of carbides and their spherical shape.

Excel file data from Figure 4.3 a) provided map distribution of carbides with better accuracy thanks to the use of Matlab, in which the position, frequence (number of carbides) and diameter have been represented in the Figure 4.4.

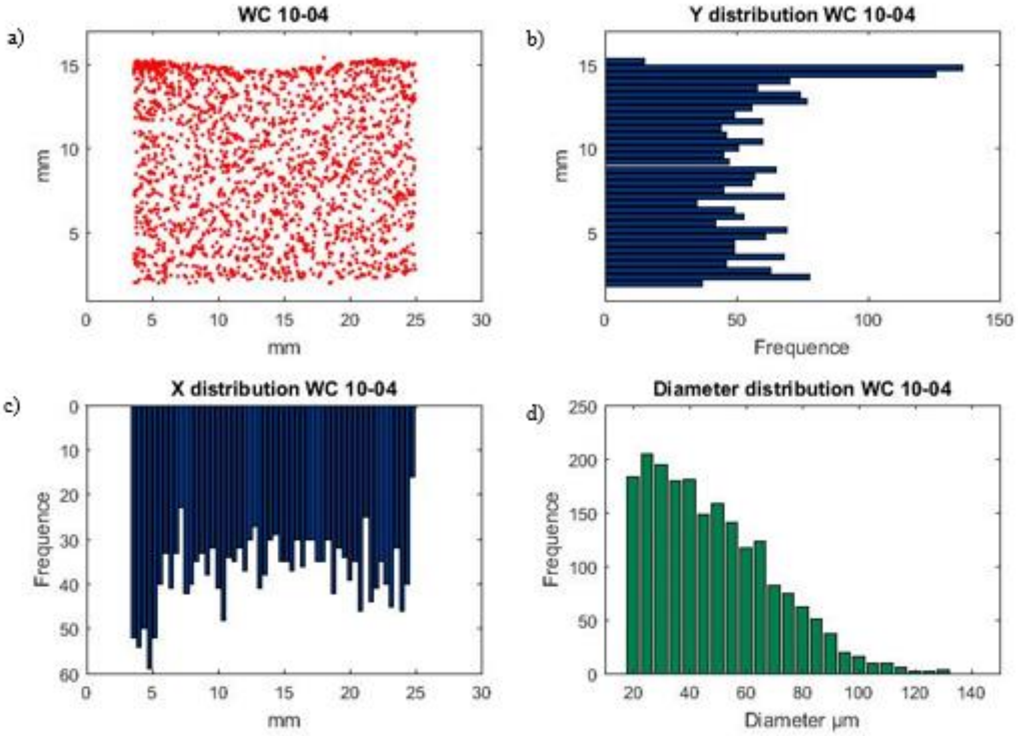

Figure 4.4: Cross section of 10-04 sample: a) Carbides distribution maps; b) carbides distribution frequency in Y direction; c) carbides distribution frequency in X direction; d) carbides size frequency.

It may be seen as the carbides distribution along Y axis (Figure 4.4, b)) is strongly displace towards the top layers. Without take into account the two largest peaks, the carbides distribution change continuously along Y axis showing many small peaks and valleys in frequence. The carbides distribution along X axis (Figure 4.4, c)) exhibits the largest peaks in the left side of the material. Also in this case, are present many small peaks and valleys in frequence. The peak of maximum frequency as a function of the size of carbides (Figure 4.4 d)) is reached around a diameter of 30µm, whereas the maximum frequency for the virgin tungsten carbides before the cladding process corresponds to a diameter of 75µm, as Figure 4.5 b) shows. The diameter distribution of virgin WC (Figure 4.5 b)) are derived by the detection of the pure tungsten carbides in Figure 4.5 a) with Stream Motion software.

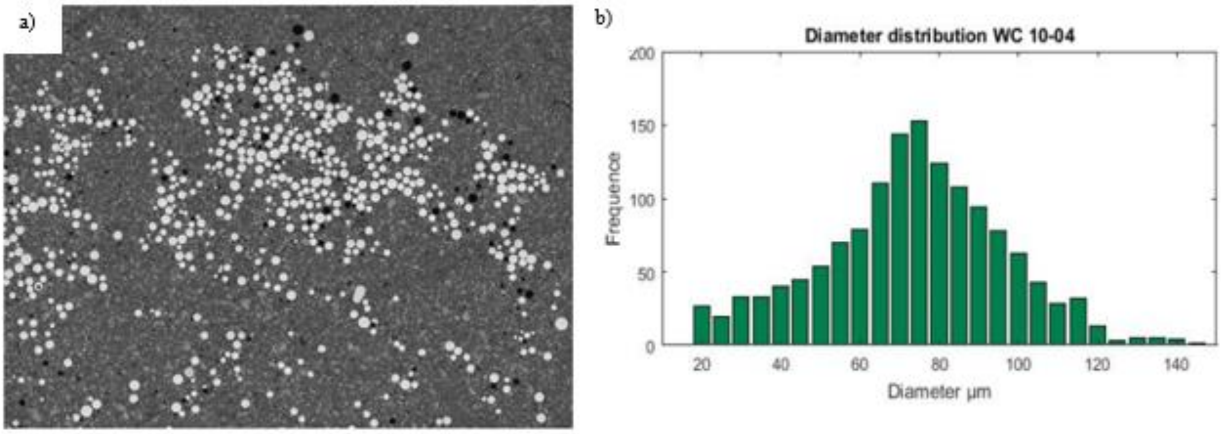

Figure 4.5: a) Virgin tungsten carbides dispersed in the bakelite; b) diameter distribution of pure WC.

As mentioned before, since the carbides distribution along Y axis exhibits the largest peaks (with a big difference in frequence than the others) in the top region, it has been interesting evaluate again position, frenquency and size distribution of tungsten carbides without consider the top layers. The result is reported in the following Figure 4.6.

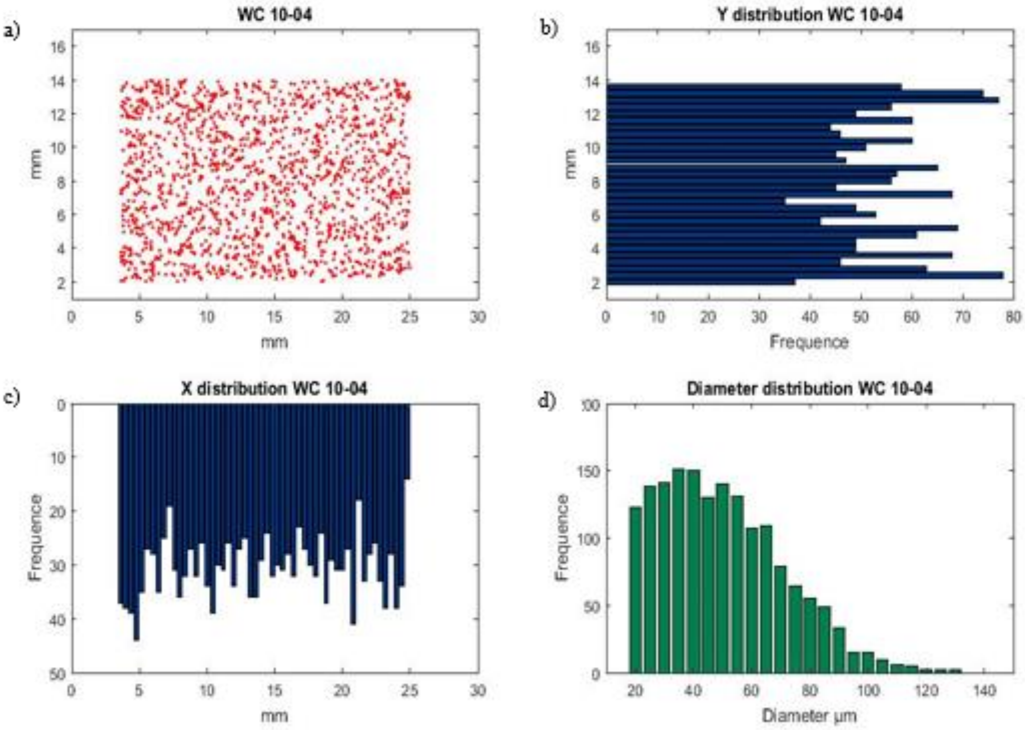

Figure 4.6: Cross section of 10-04 sample without last layers: a) Carbides distribution maps; b) carbides distribution frequency in Y direction; c) carbides distribution frequency in X direction; d) carbides size frequency.

The maximum frequency as a function of carbides diamater (Figure 4.6 d)) is now displaced towards greater size (around 40µm) if it is compared with Figure 4.4, demonstrating as the carbides present in last tracks had very low size. Carbides with size between 20 and 55 µm present the highest frequncies, whereas for greater diameter the frequence gradually decreases. To have a better idea of the dimension of carbides in the top part, only the last layers are plotted, as it is shown in Figure 4.7.

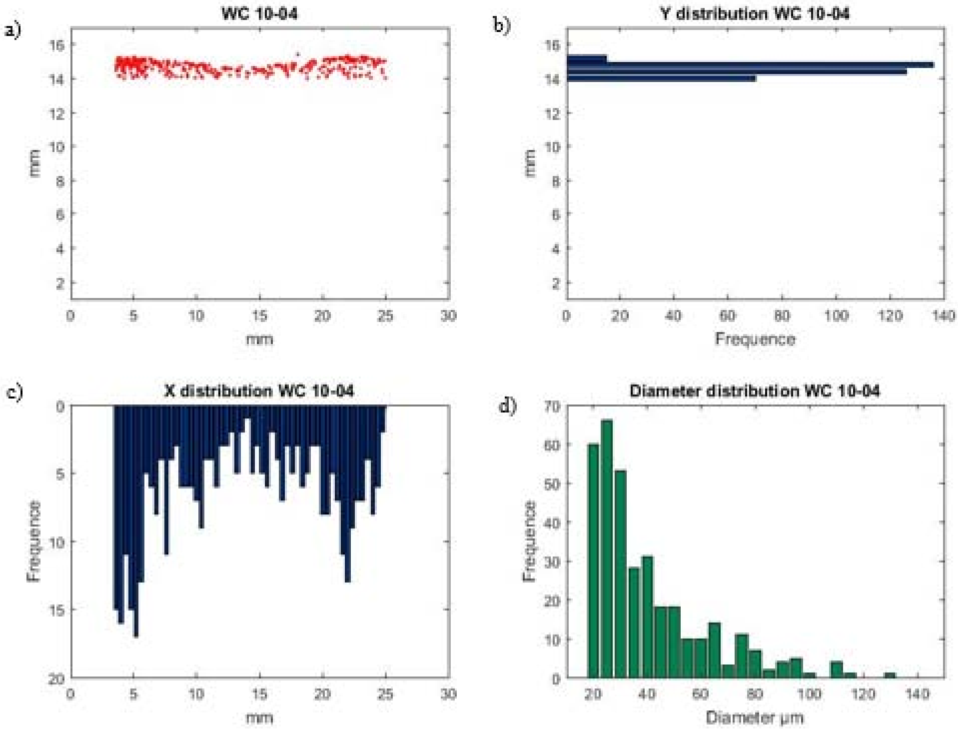

Figure 4.7: Last layers of cross section of 10-04 sample: a) Carbides distribution maps; b) carbides distribution frequency in Y direction; c) carbides distribution frequency in X direction; d) carbides size frequency.

As expected, the diameter distribution of the last tracks exhibits the largest peaks around 20-30µm confirming the previous explanation.

4.1.2 Scanning Electron Microscopy

A deeper study of the microstructure of the cross section was done using Scanning Electron Microscope (SEM). At different heights of the cross-section, morphology of the phases and EDS profiles on the microstructure of the 316L+10%WC were studied. Depending on the position in the deposited track and the WC carbides, it is possible to distinguish different microstructure due to the presence of the large reinforcements and the HAZ (Figure 4.8).

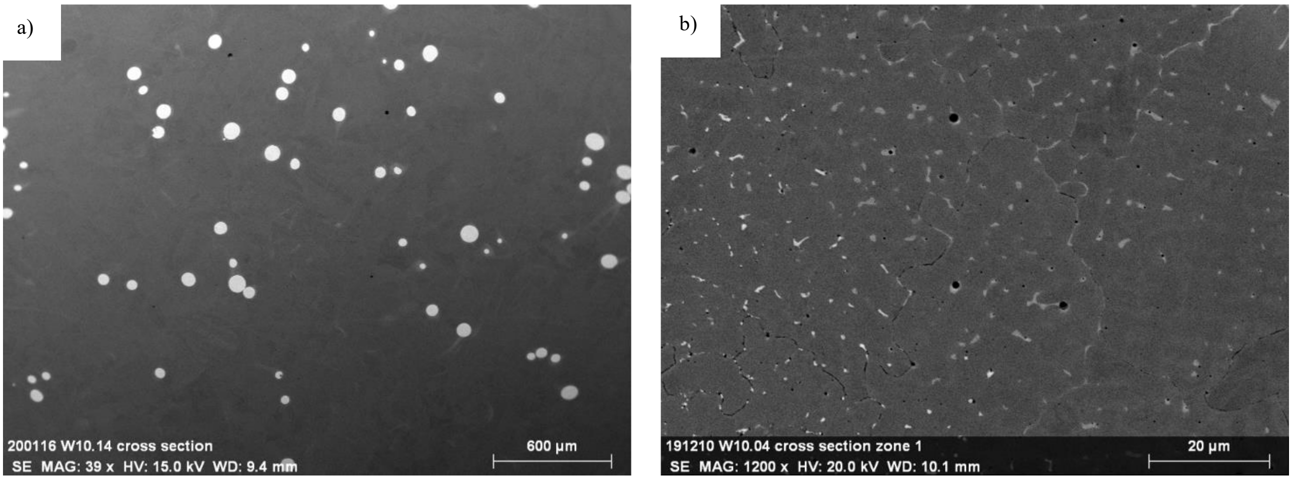

Figure 4.8: SEM images: a) cross section large view of partially dissolved WC dispersed into the matrix; b) HAZ and track of the cross section (brighter and darker zone, respectively).

Nearby of the large WC carbides (Figure 4.9), different types of carbides may be observed i.e. dark compact, complex regular and skeletal brighter carbides.

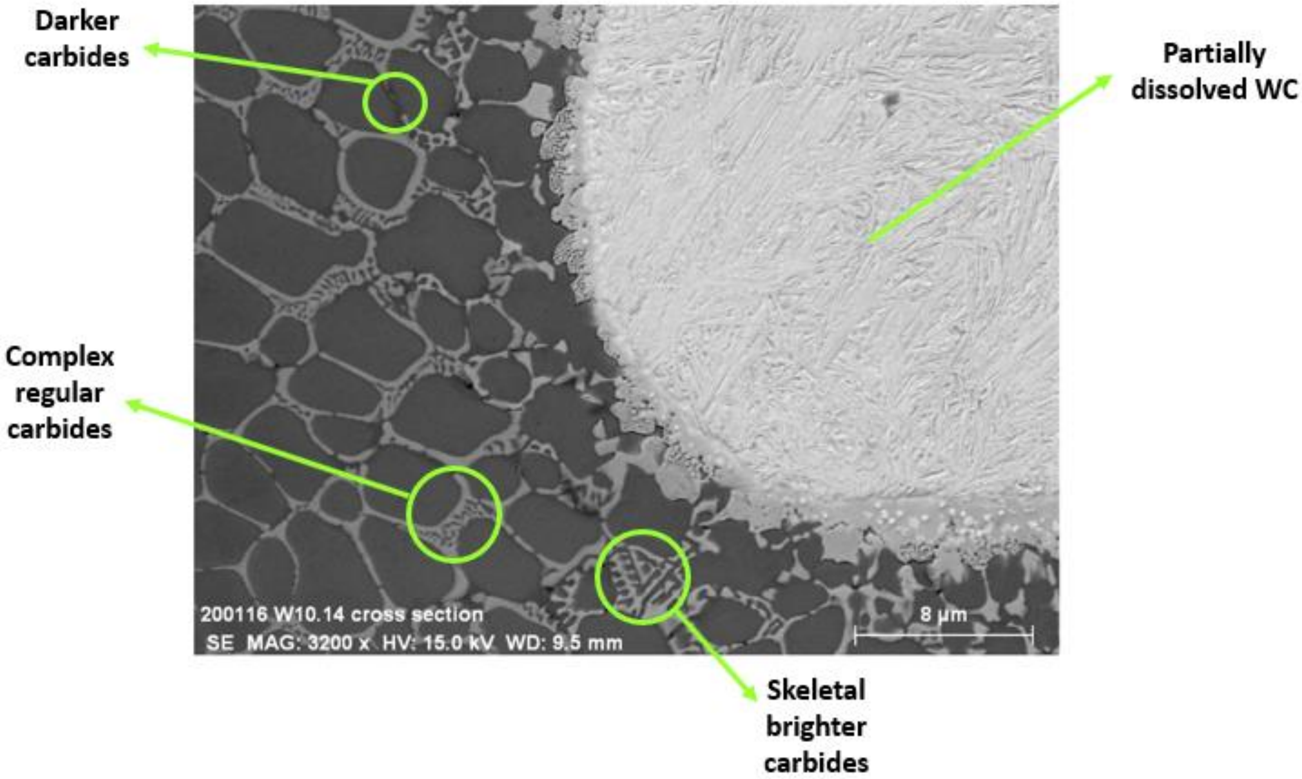

Figure 4.9: SEM image of big partially dissolved WC and sorrounding area with different types of carbides dispersed in the matrix.

Slightly dissolved WC exhibit a carbide crown, delimitating the unperturbed carbide core and the rest of the microstructure. The carbide crown may exhibit lamellar morphology as it is shown in Figure 4.10.

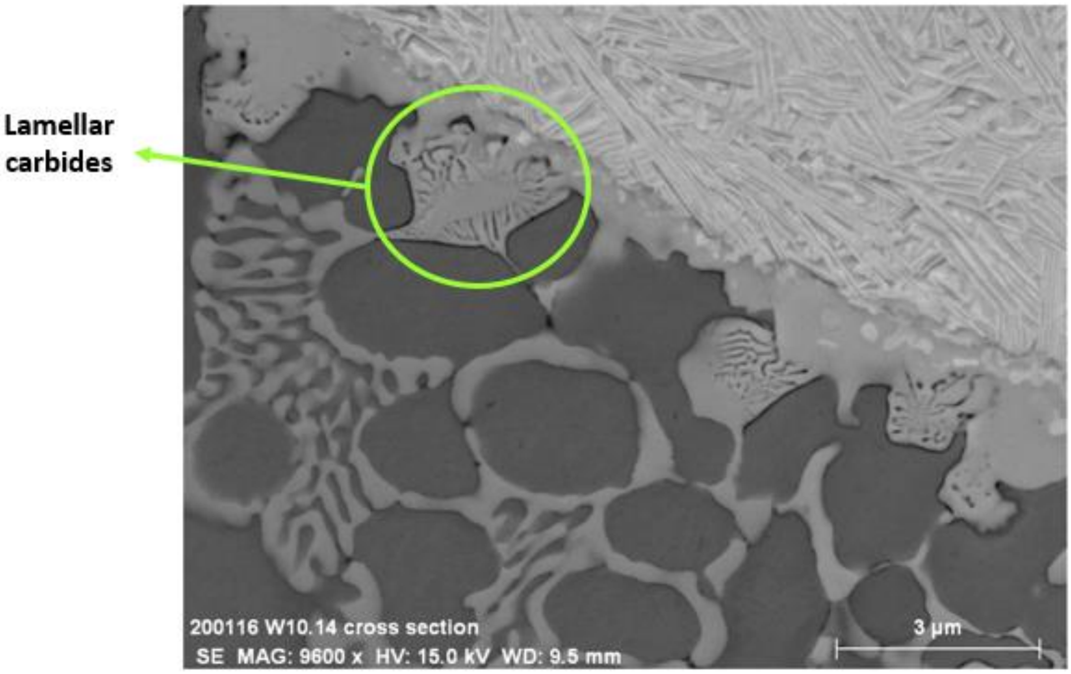

Figure 4.10: Higher magnification of big partially dissolved WC and sorrounding region.

The BSE mode provides images with different shades of grey, white and black colour, depending on the types of atoms present. Brighter zones are enriched of heavy atoms such as W, whereas darker zones are characterized by the presence of lighter atoms such as Cr. The carbides observed in the surrounding of the WC carbides appear of larger size and brighter in comparison with the carbides solidified in the melt pool and away from the WC reinforcements (Figure 4.11). The colour and therefore the composition changes moving away from the big carbide where the complex regular carbides are the only present in the melt pool. EDS profile in Figure 4.11 provides the chemical composition around the big carbide. The mass percentage of each element present in the zone analysed and the spectra of chromium and tungsten are shown in Table 4.1 and Figure 4.12, respectively.

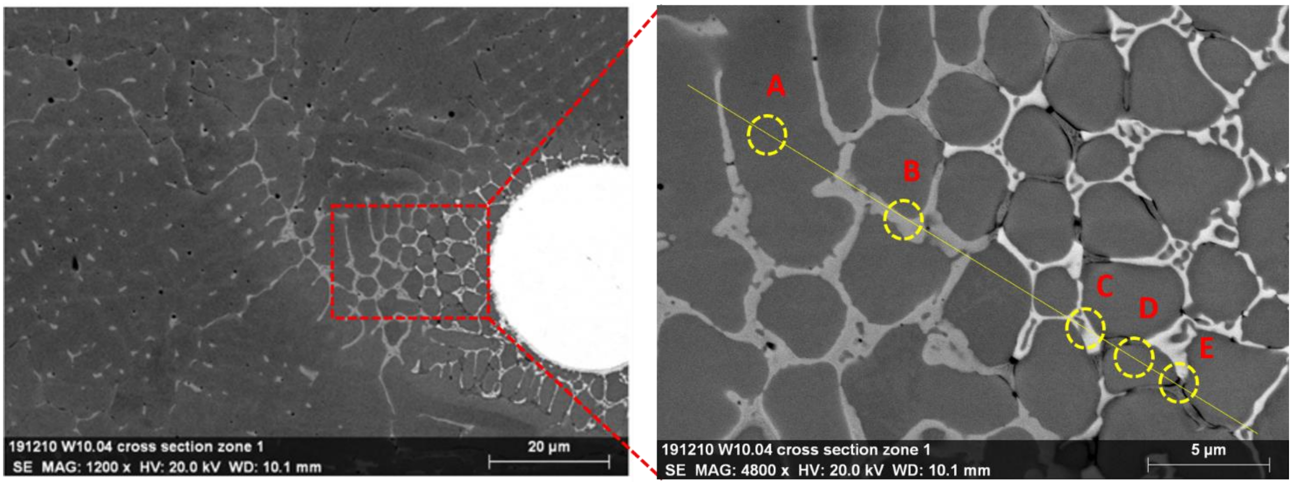

Figure 4.11: EDS profile in the zone close to the big carbide at 6 mm far from the substrate.

Points A and D present almost the same composition as Table 4.1 shows. These points can be associated to matrix with high amount of tungsten due to the partial dissolution of big WC. Point B exhibits a slight increases of tungsten, as the W-spectrum (Figure 4.12, left side) shows, together with a relavite high amount of chromium (Table 4.1). It may be associated to complex regular carbide. Point C is characterised by a sharp peak of W in the W-spectrum (Figure 4.12, left side), it can be associated to skeletal brighter carbide. Point E shows a sudden peak of Cr in the Cr-spectrum (Figure 4.12, right side) accompained with no high amount of tungsten if compared to points B and C. It may be associated to dark compact carbide.

Mass %		C	Cr	Fe	W	Ni	Mo	Si	Mn
A	**Matrix**	2.37	13.25	60.22	9.6	11.69	1.79	0.25	0.83
B	**Complex regular carbide**	2.58	**16.93**	42.5	**26.36**	7.16	3.57	0.057	0.78
C	**Skeletal brighter carbide**	1.91	13.84	37.26	**36.37**	5.24	4.18	0.067	0.94
D	**Matrix**	1.48	12.93	59.82	11.8	11.86	1	0.25	0.86
E	**Dark compact carbide**	2.6	**18.01**	55.00	11.52	9.96	2.04	0.27	1.00

Table 4.1: Mass percentage of the elements present along the profile in Figure 4.11.

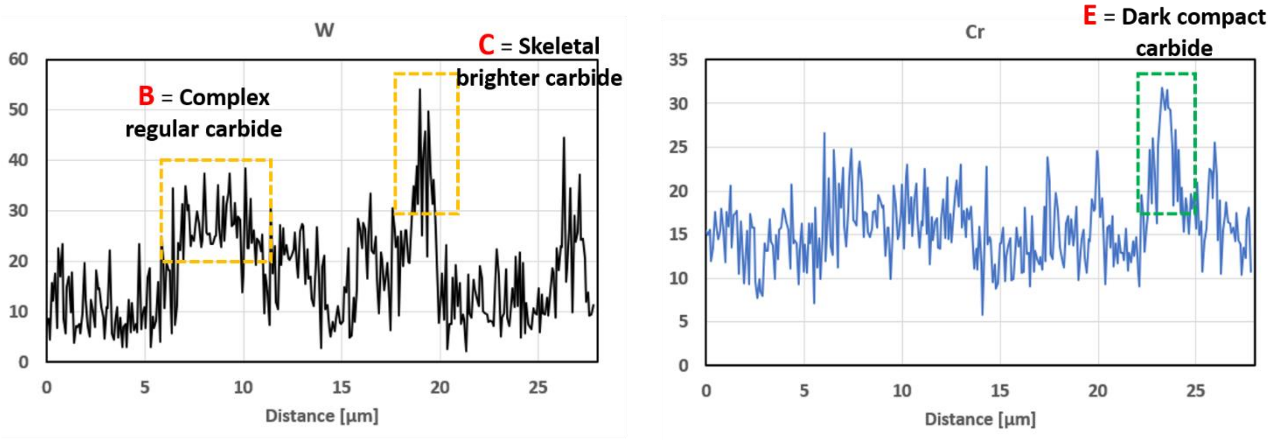

Figure 4.12: W and Cr spectra along the EDS profile showed in Figure 4.11.

In the HAZ brighter carbides are observed with smaller size of the complex regular carbides and the morphology is more coarsened. The rectangle in Figure 4.13 represent a region characterized by brighter carbides (Heat Affected Zone) compared to the surrounding area (track).

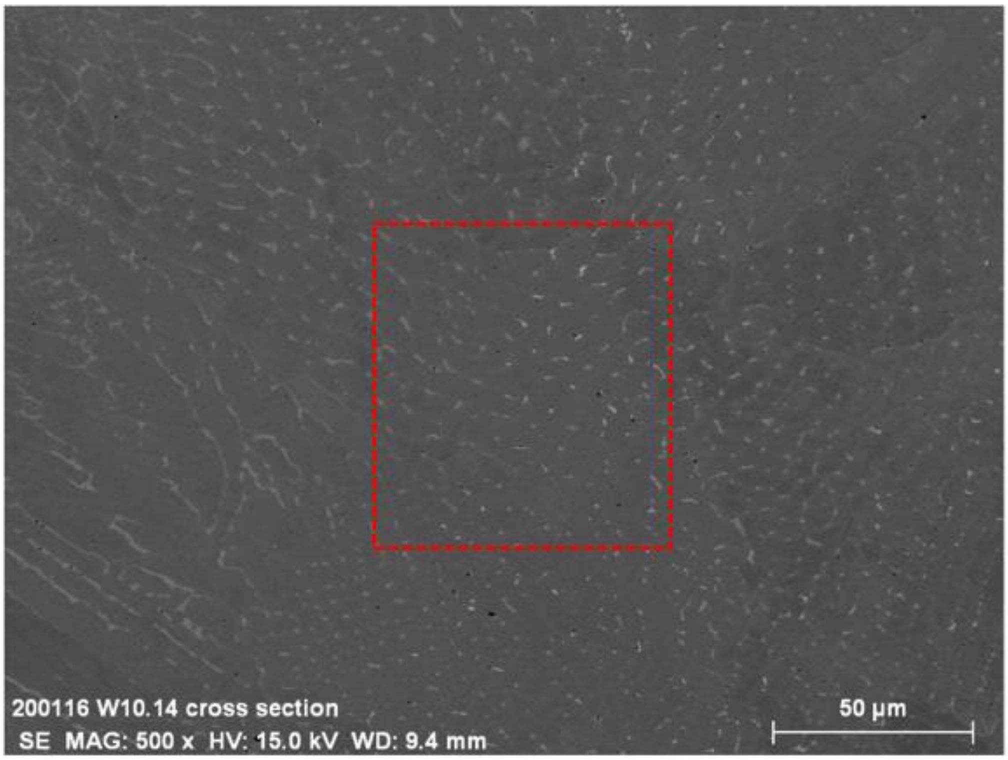

Figure 4.13: Heat afftected zone (HAZ) and track in the matrix away from the large WC. HAZ is represented by brighter colour of carbides, whereas the darker colour of carbides correspond to the track.

In Figure 4.14 the same image of Figure 4.13 at higher magnification is shown, in which two EDS profiles were performed in order to emphasize the different compositions between the Heat Affected Zone and the track.

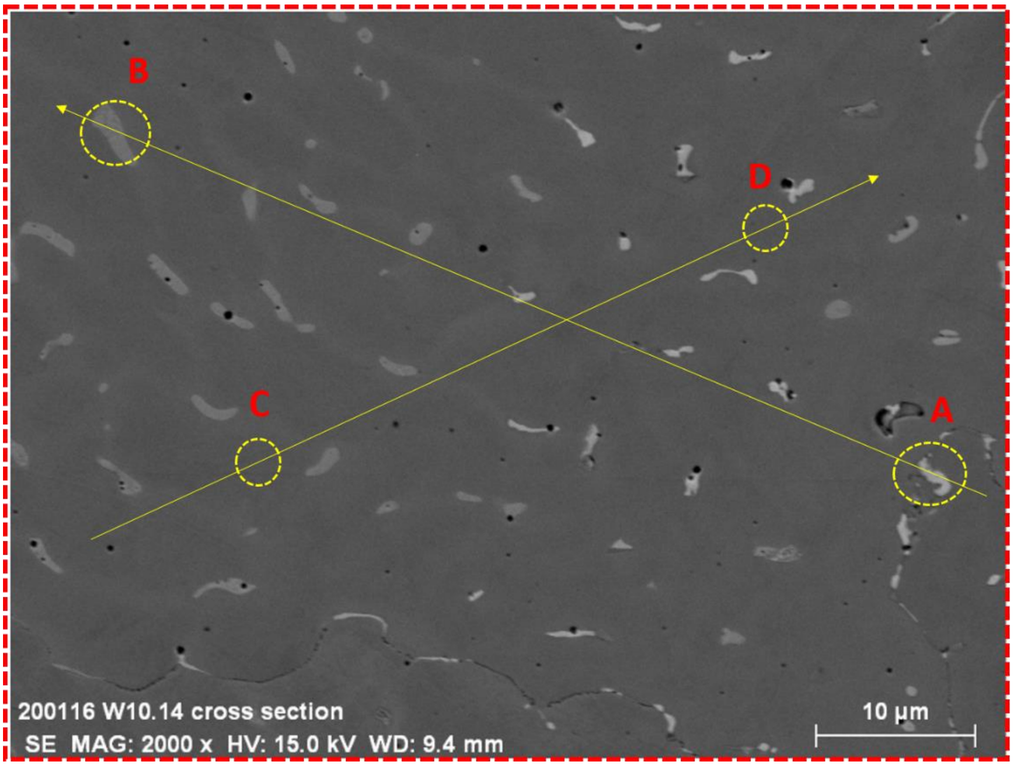

Figure 4.14: EDS profiles along HAZ (right side) and the track (left side).

The percentage in mass of the composition along some zones of the profiles in Figure 4.14 are reported in Table 4.2. The W and Cr spectra of the two profiles are shown in Figure 4.15 (left and right side, respectively). The A and B peaks in W-spectrum exhibit a difference amount of tungsten and slight difference amount of chromium. The brighter compact carbide who belong to the HAZ (zone A) shows higher content of tungsten compared with the amount of tungsten present in the complex regular carbide in the track (point B), as can be seen in Figure 4.15, left side. Instead, the amount of chromium is slightly greater in the complex regular carbide (point B) than the brighter compact carbide (point A). Regarding C and D points, they can be associated to matrix with a presence of tungsten (Table 4.2). The amount of tungsten in the matrix is lower far from the giant WC (Table 4.2, C and D points) if compared it close to the partially dissolved WC (Table 4.1, A and D points).

Mass %		C	Cr	Fe	W	Ni	Mo	Si	Mn
A	**Brighter compact carbide**	1.79	**16.11**	38.36	**29.13**	5.42	8.24	0.025	0.81
B	**Complex regular carbide**	3.46	**21.8**	46.58	**13.52**	7.16	6.23	0.19	1.4
C	**Matrix**	1.15	14.83	62.57	4.41	11.7	1.54	0.32	1.15
D	**Matrix**	1.22	14.8	65.33	5.33	11.13	1.1	0.29	0.84

Table 4.2: Mass percentage of the elements present along the profile in Figure 4.14.

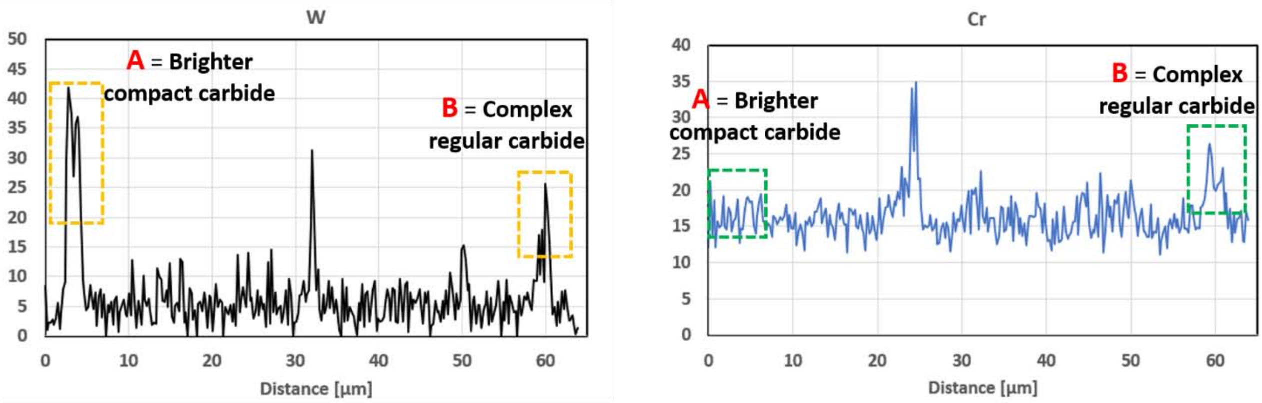

Figure 4.15: W and Cr spectra along the EDS profile showed in Figure 4.14.

During laser cladding the tungsten carbides are partially or completely dissolved in contact with the molten liquid. The C and W of the WC powders enrich the initial 316L composition and this enrichment leads to the formation of carbides in the intercellular spaces [49]. Hence, the average composition of W was calculated at three different heights from the substrate in order to evaluate the dissolution of the WC powders during cladding. Two EDS profiles were carried out at every height (2, 6 and 10mm far from the substrate), as Figure 4.16 a) shows. The profiles were carried out without pass through big carbides as it is represented in Figure 4.16 b).

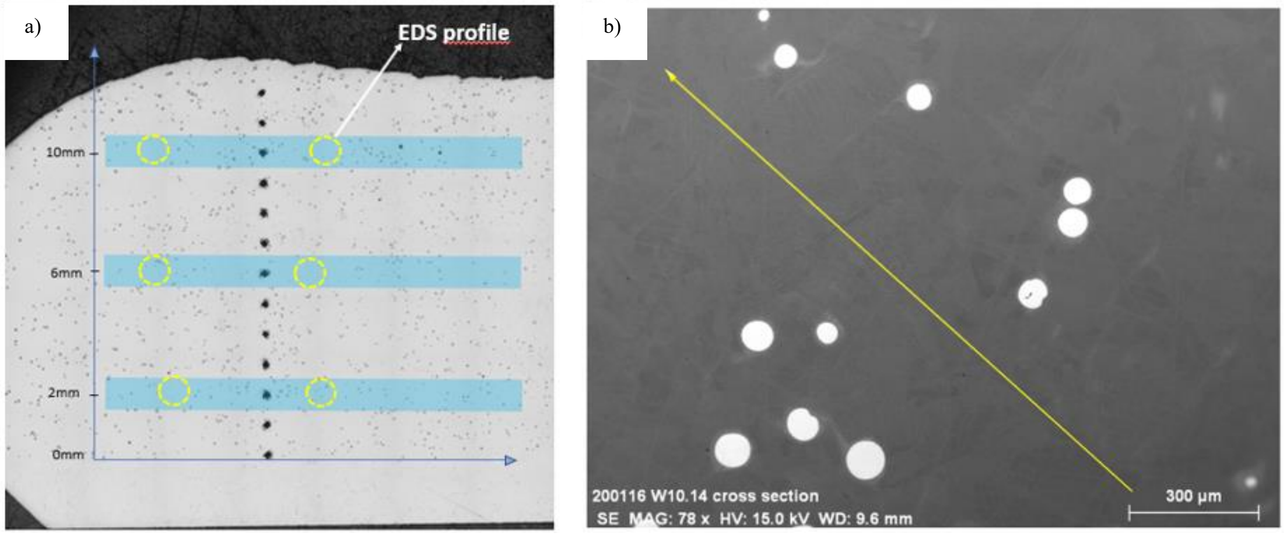

Figure 4.16: a) OM image with three different zones (light blue colour) on which EDS profiles were carried out; b) One of the EDS profiles considered to evalute the mean amount of tungsten in the matrix.

The average values (%wt.) of W at the three heights considered is plotted in the Figure 4.17. The maximum amount of tungsten is around 4.5% (%wt) corresponding to the core of the deposit. However, the standard deviation at that height is the greatest. At 2 mm from the substrate the amount of tungsten in the material is the lowest, around 3.2% (%wt), whereas amount around 3.8% (%wt) is achieved at 10 mm from the substrate.

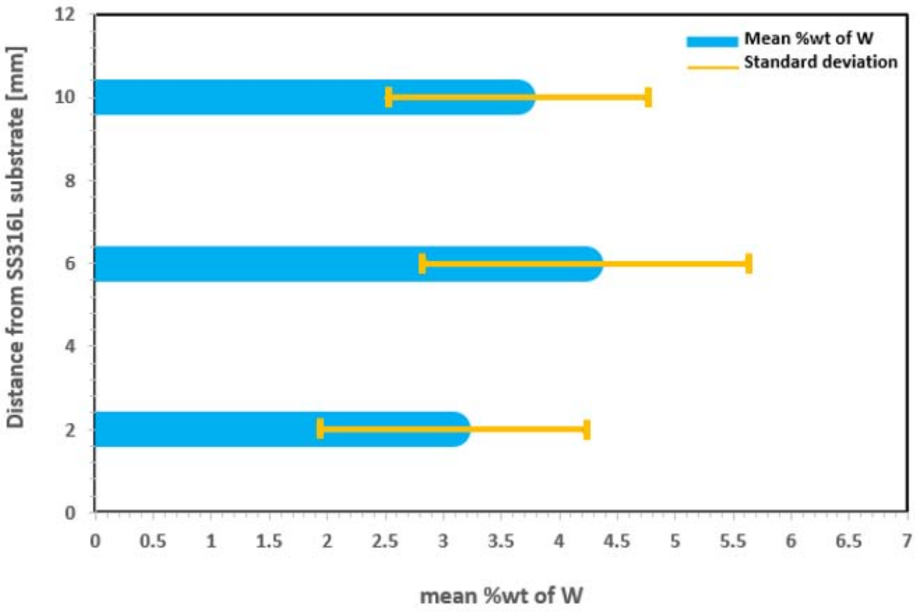

Figure 4.17: Average percentage in mass of tungsten at different heights from the substrate.

4.1.3 EBSD

Electron Back-Scattered Diffraction analyses were used to estimate the grain size at different heights in the cross section and to identify the different crystallographic structures present in the composite. Due to the out-of-equilibrium status of the phases formed during laser cladding process, some phases were not recognised during the analysis. Bad indexation is related to modification or supersaturation of the crystal lattices and not good surface preparation. Ultra-fast solidification rates and the presence of many atoms may lead to the formation of those out-of-equilibrium phases. Figure 4.18 a) shows the zone that was analysed for the identification of the phases (BSE image). The bright pattern quality (Figure 4.18 b)) corresponds to an overall good indexation, since only a few darker zones are observed.

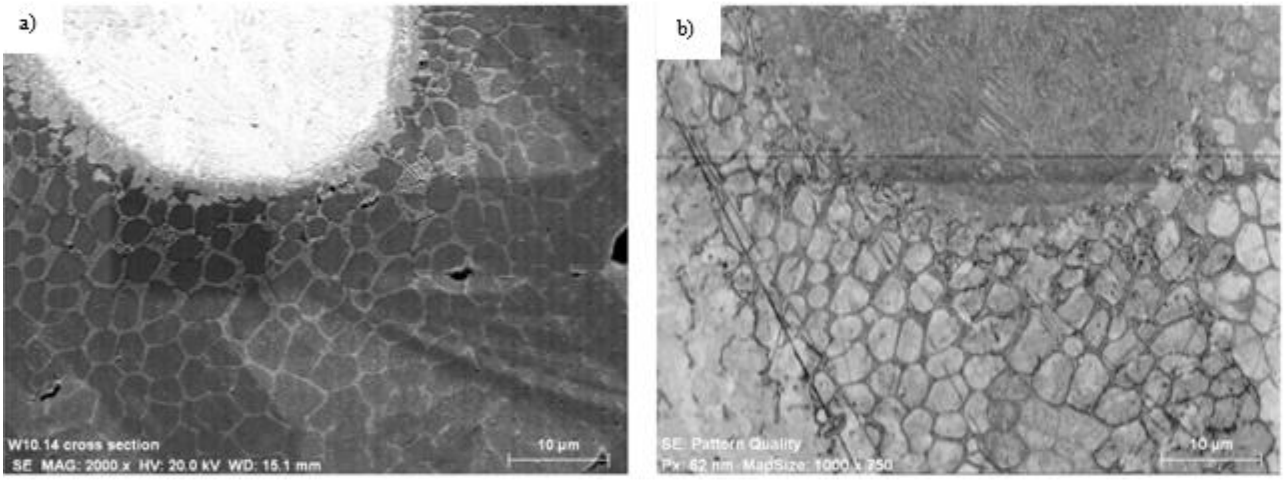

Figure 4.18: a) BSE image of big WC in which EBSD analysis was carried out; b) Pattern quality of the Figure 4.18 a).

In Figure 4.18 a) almost every phase was identified. The matrix was identified as austenite (FCC) with varying lattice parameters and it corresponds to the major part of the zone analysed. The large WC carbide is composed by crystals and it was identified as WC carbide (Hexagonal), W_2C (Orthorhombic) and an FCC crystal lattice identified as austenite (Figure 4.19). Complex regular carbides are partially identified as austenite as well, while the solidification carbides in the vicinities of the WC carbide are identified as two M_6C carbide (FCC) with same lattice parameters, but different atoms positions (Figure 4.19, light blue and yellow colours). This particular result will be explained in the next chapter 5.

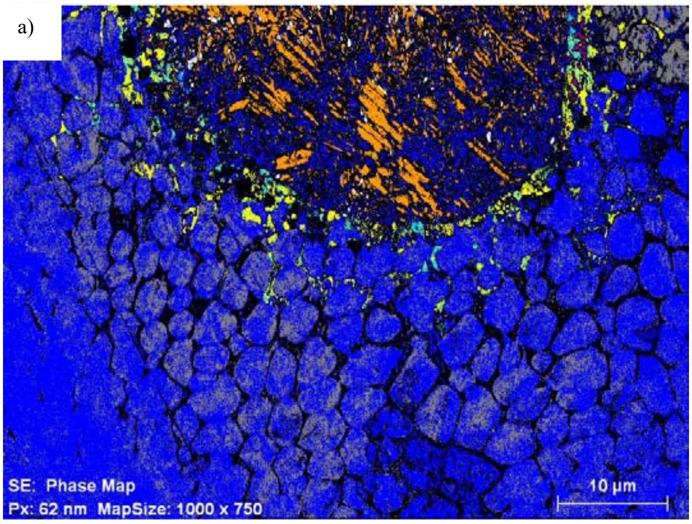

b)

	Phase	**Crystal system**	**Crystal lattice parameters a_0 b_0 c_0 [nm]**
🟦	**Austenite**	**FCC**	**0.3662**
▨			**0.4270**
🟧	**Tunsten carbide (Qusongite, WC)**	**H**	**0.2902** **0.2902** **0.2831**
⬜	**W_2C**	**O**	**4. 721** **6.03** **5.18**
🟪	**Tungsten (W)**	**BCC**	**0.3159**
* 🟨	**Iron tungsten carbide**	**FCC**	**1.1087**
* 🟦	**Iron tungsten carbide**	**FCC**	**1.1087**

Figure 4.19: a) Phase map of the EBSD analysis based on Figure 4.18; b) Phases considered for the EBSD analysis with the relative lattice characteristics. * The two Iron tungsten carbides in yellow and light blue show the same crystal system and lattice parameters; they differ only for the arrangment of the atoms in the crystal lattice.

Furthermore, EBSD analysis was carried out also far from the big tungsten carbides (Figure 4.20) in order to have a general view of the composite. The zone chosen for this EBSD analysis is the transition between HAZ and track of Figure 4.14, in which two EDS profiles were performed. Figure 4.20 a) shows the BSE image from which the pattern quality of Figure 4.20 b) was obtained. Also in this case, the pattern quality exhibits only a few darker zone indicating a general good quality of indexation. The solidification carbides are highlighted by brighter spots in the Figure 4.20 a). They were not well recognised.

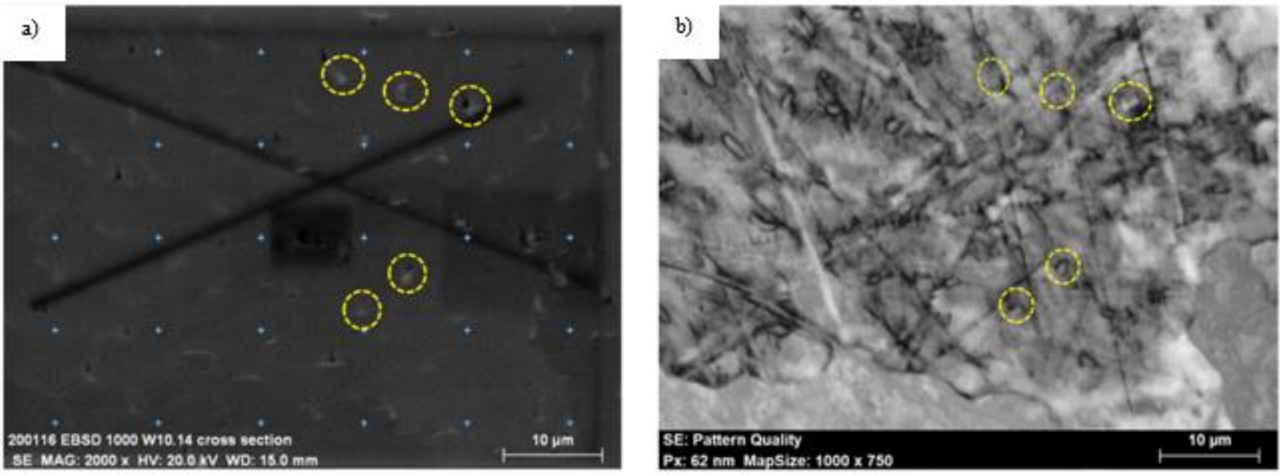

Figure 4.20: a) SEM image of a zone far from giant tungsten carbide. Precipitated carbides are partially recognised; b) Pattern quality of the Figure 4.20 a).

The phase map shown in Figure 4.21 a) exhibits the presence of austenite (blue colour) and presence of iron tungsten carbide with FCC crystal system (confirmed also in Figure 4.20, with yellow circles). Some black zones are not identified even if the indexation was good.

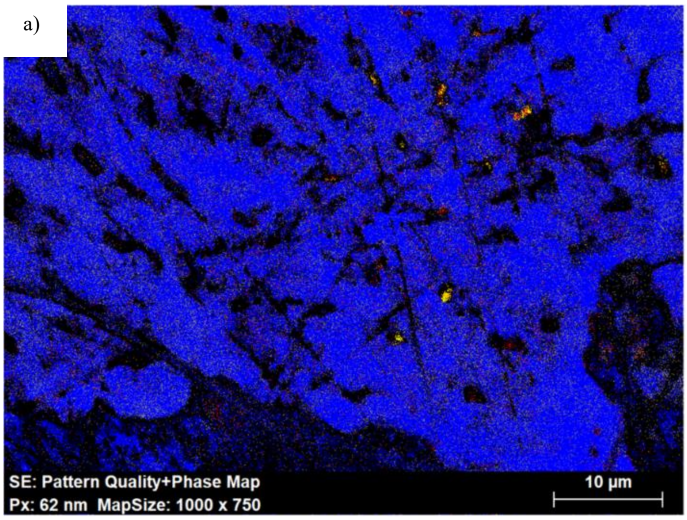

b)

	Phase	**Crystal system**	**Crystal lattice parameters a_0 b_0 c_0 [nm]**
🟦	**Austenite**	**FCC**	**0.3662**
🟨	**Iron tungsten carbide**	**FCC**	**1.1087**

Figure 4.21: a) Phase map of the EBSD analysis based on Figure 4.20; b) Phases considered for the EBSD analysis with the relative lattice characteristics.

The grain size was also evaluated by means of two EBSD analysis at low magnification. The first analysis was carried out at 2 mm from the substrate and the second analysis was performed at 6 mm from the substrate. The results obtained are summarized in Table 4.3.

Distance from the substrate	Grain size [µm]
2 mm	53
6 mm	67

Table 4.3: Mean grain size at different heights from the substrate by means EBSD analysis.

4.2 Macro-hardness

Vickers hardness test was carried out on half part of the sample W10-04 in order to evaluate the evolution of the hardness in the deposit, as it is shown in Figure 4.22.

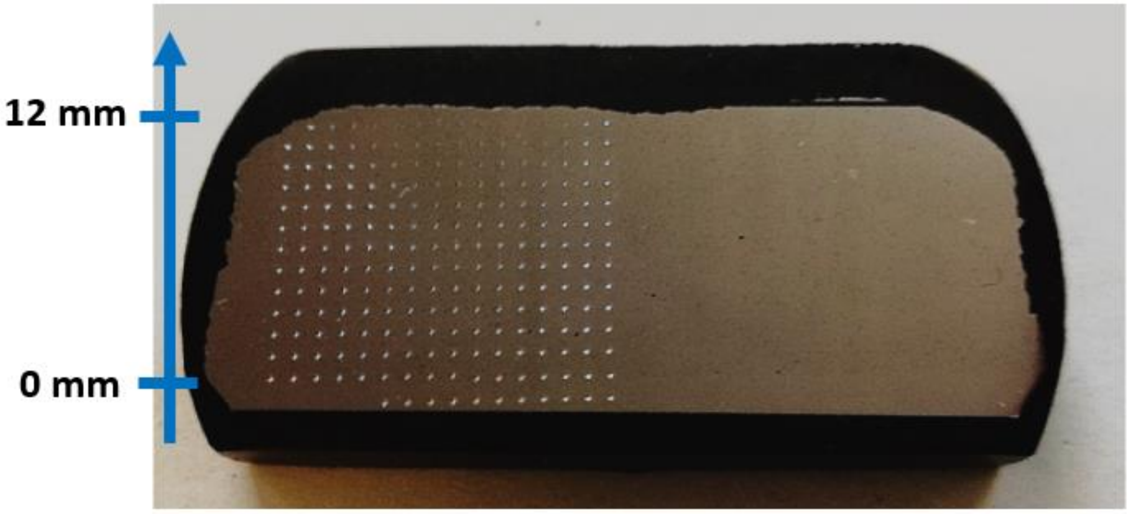

Figure 4.22: Hardness indentations on the cross section of the the sample W10-04.

The results were compared with a SS316L deposit fabricated with the same process parameters (Figure 4.23). The HV10 average value of the SS316L+10%WC is around 250, whereas for the substrate is around 190. The hardness of the composite tends to increase with increasing height, while the hardness of the SS316L tends to decrease [7].

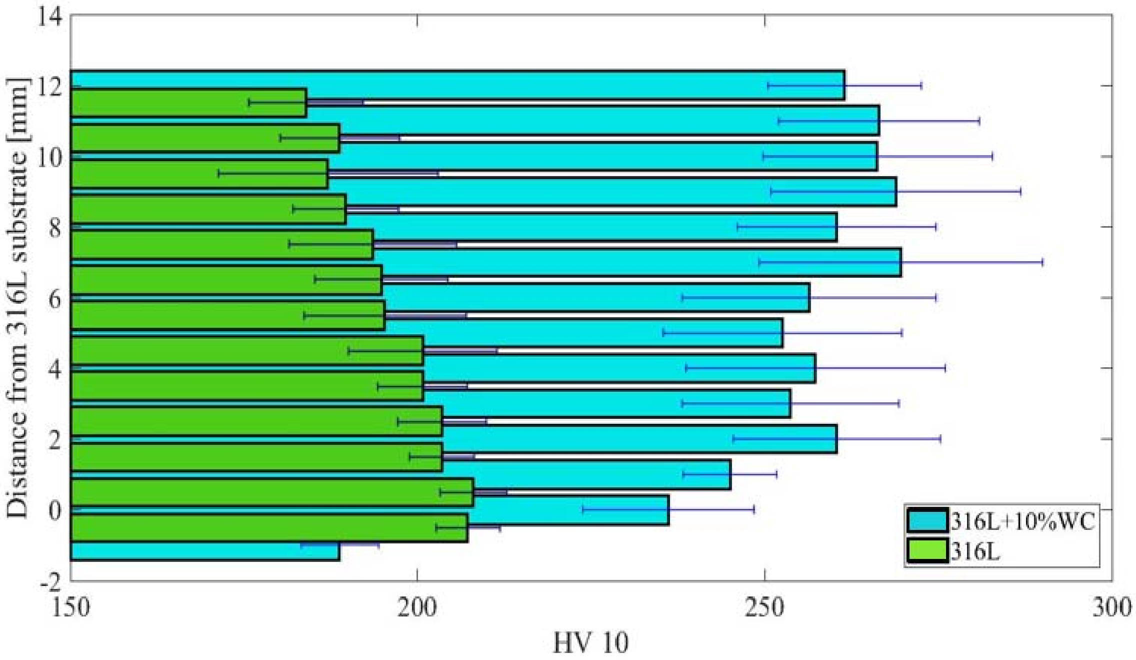

Figure 4.23: Hardness HV10 of pure SS316L and SS316L+10%WC composite against distance from substrate.

4.3 Wear tests

Several pin-on-disk tests were performed on different samples in order to characterize the wear behaviour of SS316L+10%WC composite. After each wear test the profilometer and SEM analyses were carried out on the post-mortem surfaces and the results obtained are shown in this section.

4.3.1 Tribometer tests

During the test campaign, the setup of the pin-on disc remained always the same for each wear tests, as it has been shown in Table 3.4, section 3.5. The evolution of the friction coefficient (COF) and the penetration depth as a function of the number of cycles are reported in a graph after each test, in which it is possible to study the correlation between the changing of the COF and the penetration depth. An example of the tribometer test is shown in Figure 4.24.

Figure 4.24: Sample during trimobometer test. The track and the debris are forming due to the contact between the sample and alumina ball.

The track formed on the post-mortem samples and the worn of the alumina ball (counter body) are represented by a penetration depth curve. The COF curve exhibits peaks and valleys, whereas the penetration depth shows some constant regions and others in which it slightly increases during every wear test. Each test may be divided in three main wear stages, which in turns may be recognised other different wear behaviours. To emphasize the three main zones has been chosen to use one tribometer test as a reference, represented in Figure 4.25. In the first wear stage a sharp increases of penetration depth with many short peaks and valleys are observed. The second stage is characterized by a slightly increases of COF with a constant penetration depth. The third stage starts as soon as the COF suddenly decreases. In this stage, the COF is characterized by two peaks and two valleys, whereas the penetration depth increases. After the first stage a cyclical wear behaviour may be noted, since the stage 2 and stage 3 are repeated more times during the test.

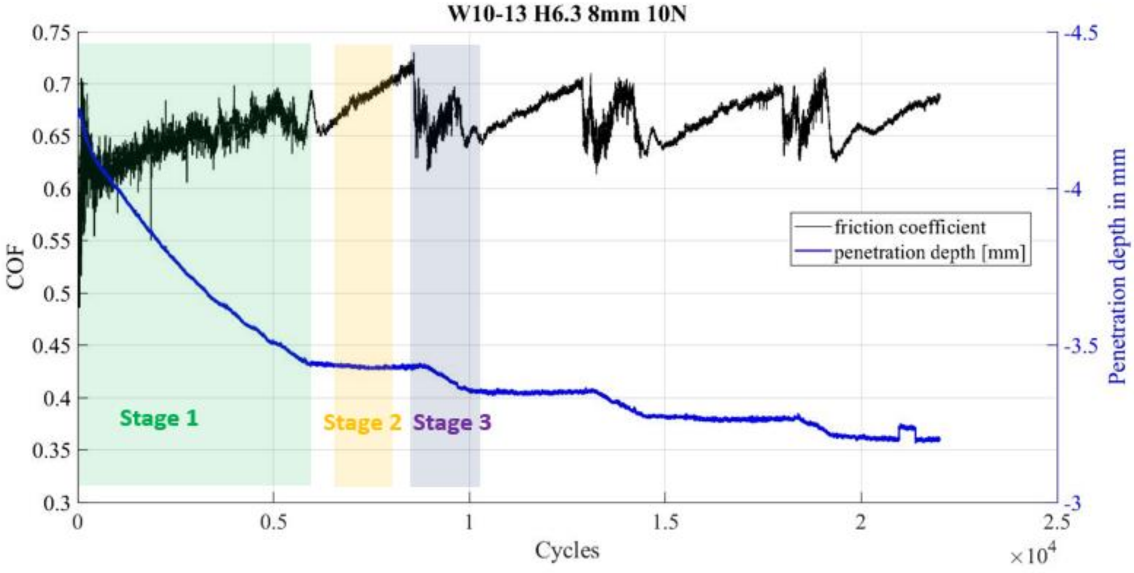

Figure 4.25: Graph derived by tribometer test used as a reference. The three wear stages may be recognised.

Seven uninterrupted tests (until 22000 cycles) were carried out and the graphs obtained are shown in the Figures 4.26, 4.27, 4.28, 4.29, 4.30, 4.31, 4.32 (Table 4.4).

Type of test	Cycles	Figure
Uninterrupted	22000	4.26
Uninterrupted	22000	4.27
Uninterrupted	22000	4.28
Uninterrupted	22000	4.29
Uninterrupted	22000	4.30
Uninterrupted	22000	4.31
Uninterrupted	22000	4.32

Table 4.4: Types of tribometer tests with their relative number of laps and number of Figure in which they are reported.

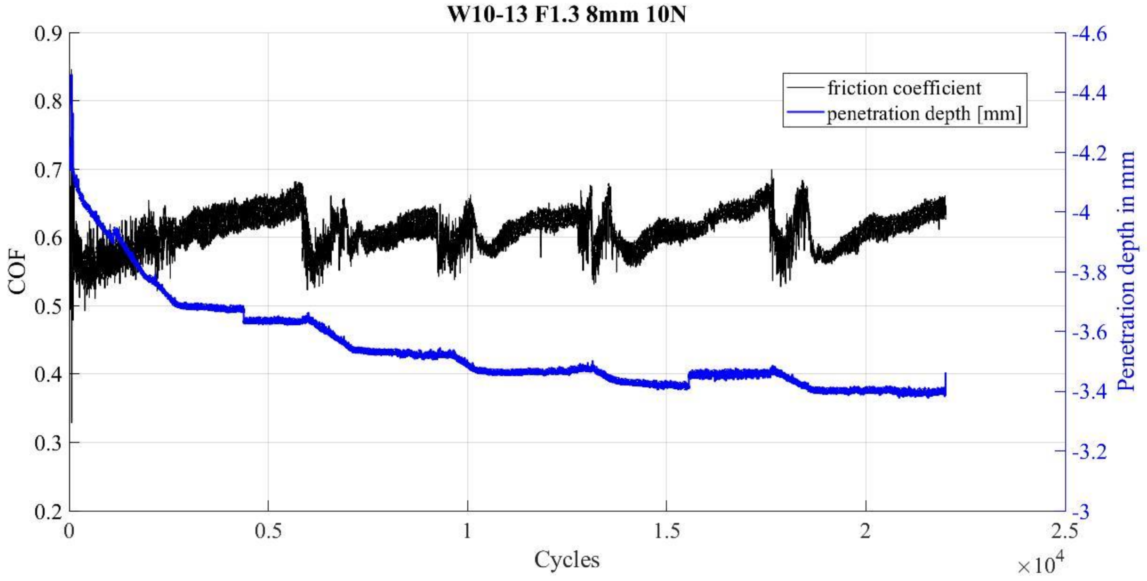

Figure 4.26: Friction coefficient and penetration depth evolution of the W10-13 F1.3 sample with radius 8mm.

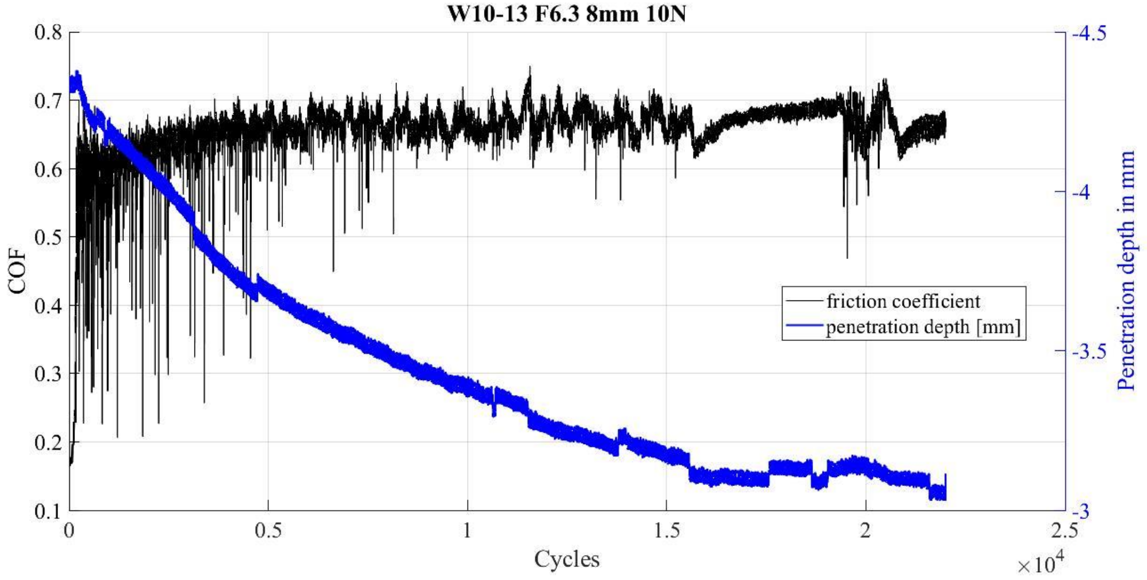

Figure 4.27: Friction coefficient and penetration depth evolution of the W10-13 F6.3 sample with radius 8mm.

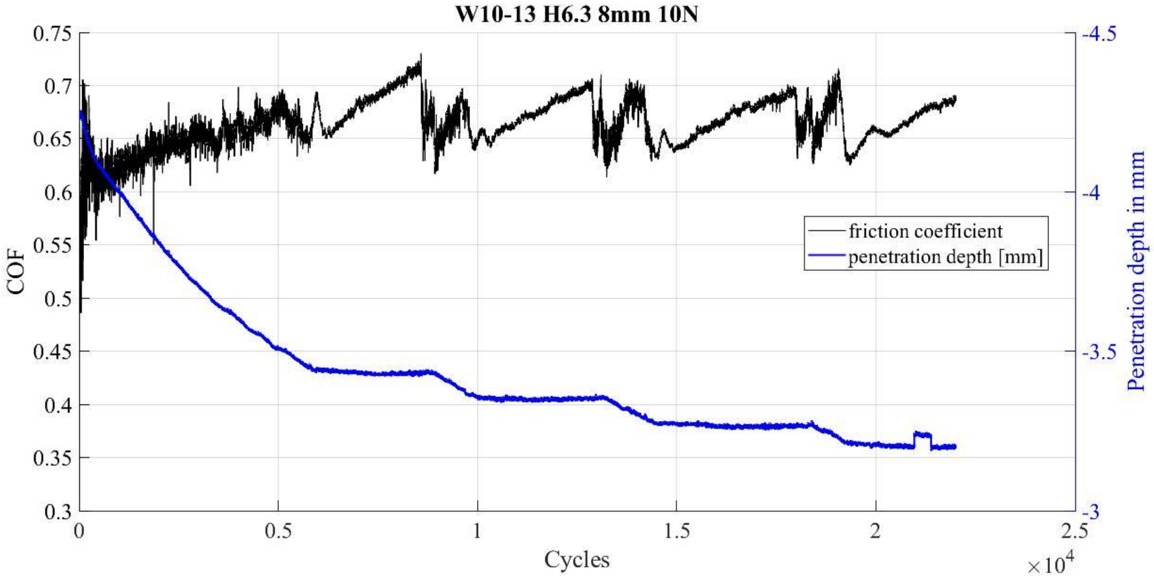

Figure 4.28: Friction coefficient and penetration depth evolution of the W10-13 H6.3 sample with radius 8mm.

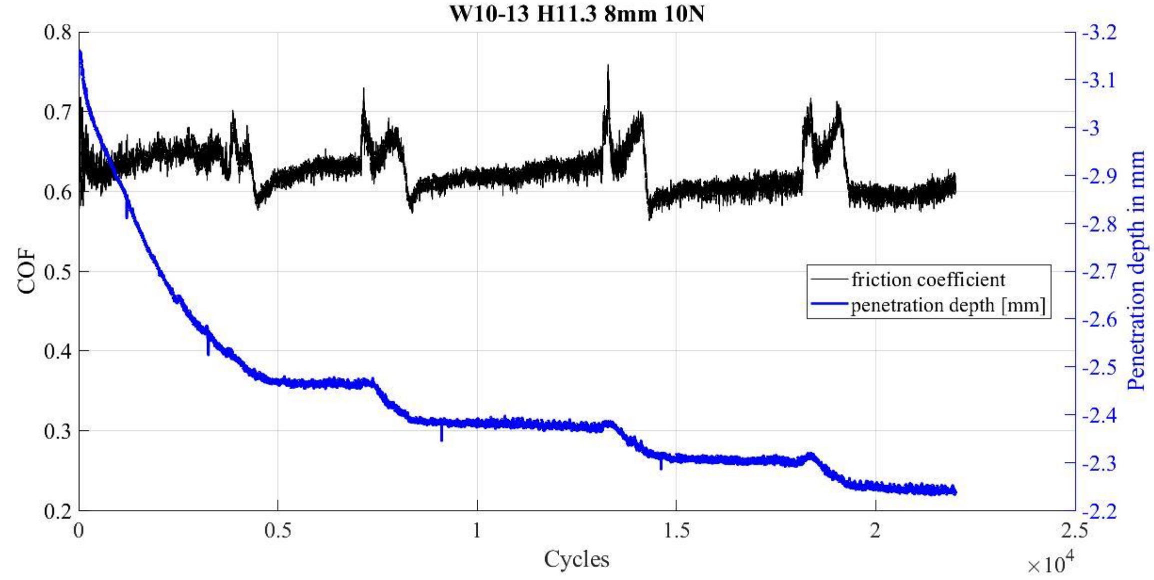

Figure 4.29: Friction coefficient and penetration depth evolution of the W10-13 H11.3 sample with radius 8mm.

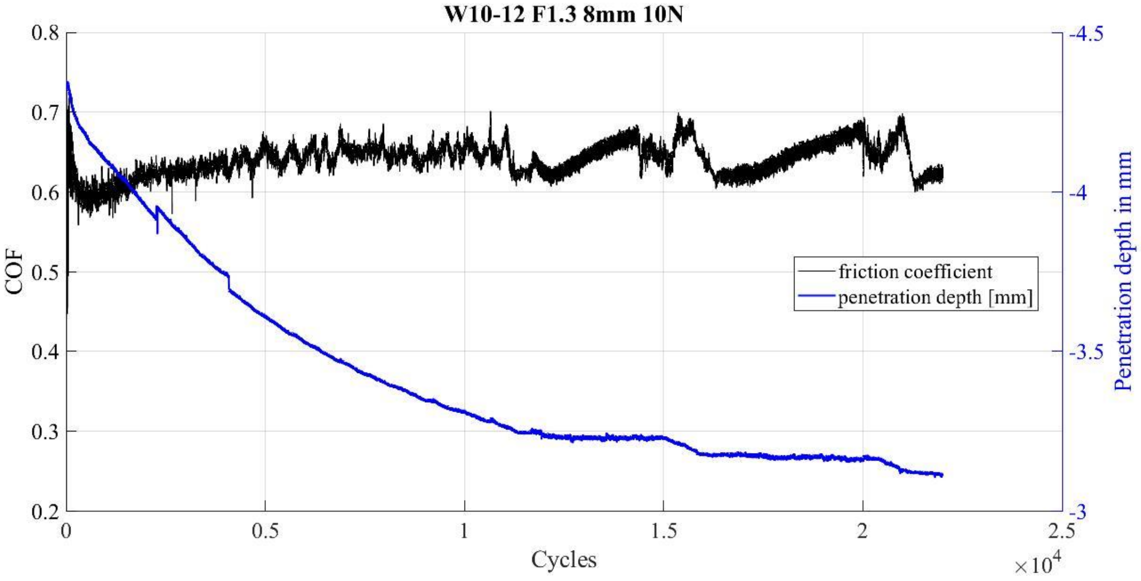

Figure 4.30: Friction coefficient and penetration depth evolution of the W10-12 F1.3 sample with radius 8mm.

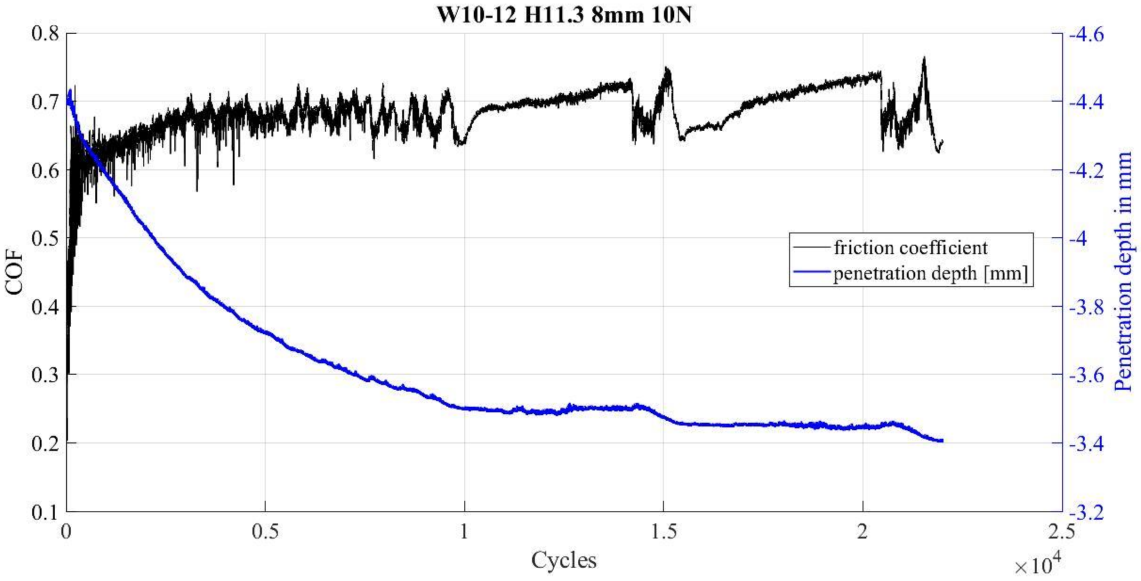

Figure 4.31: Friction coefficient and penetration depth evolution of the W10-12 H11.3 sample with radius 8mm.

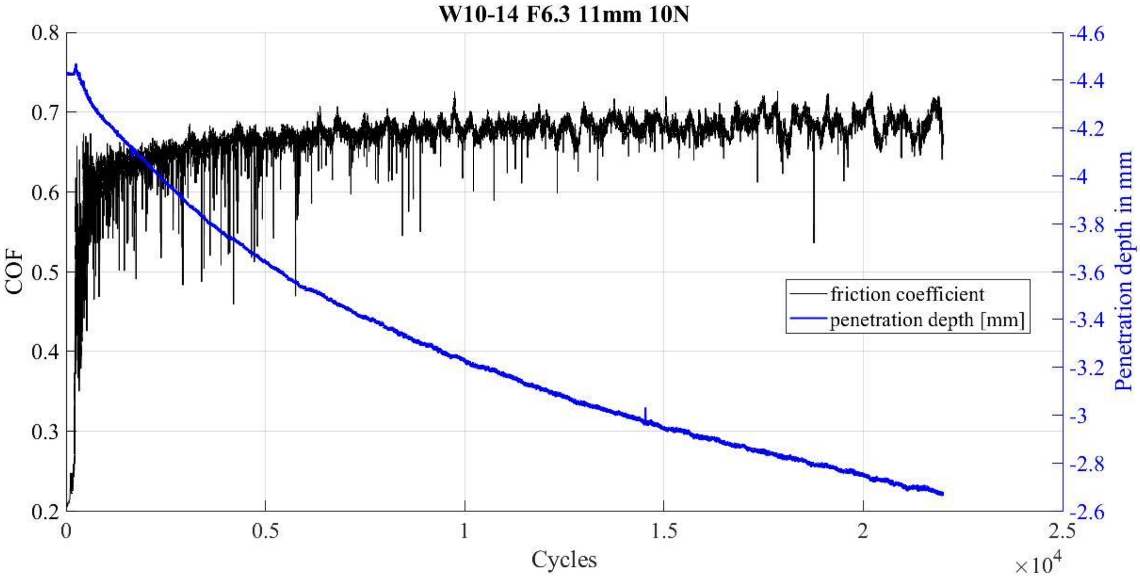

Figure 4.32: Friction coefficient and penetration depth evolution of the W10-14 F6.3 sample with radius 11mm.

The same trend of the COF and penetration depth curves can be seen in almost every tribometer test demonstrating a high rate of reproducibility. Figure 4.29 shows a peculiar COF curve with the sequence of peaks and valleys that is modified, whereas Figure 4.32 exhibits only the first stage of wear behaviour. In the subchapter 5.3.2 these two particular cases will be explained.

In order to have a better comprehension of the wear behaviours in every single stage four interrupted tests were performed (Figures 4.34, 4.35, 4.36, 4.37, Table 4.5). Considering as reference Figure 4.25, the four specific points in which stop the machine were decided, as it shows in Figure 4.33. In the Table 3.4, section 3.5, the setup of interrupted tests is shown.

Test number	Type of test	Cycles	Figure
1	Interrupted	2000	4.34
2	Interrupted	15500	4.35
3	Interrupted	12000	4.36
4	Interrupted	7500	4.37

Table 4.5: Types of tribometer tests with their relative number of laps and number of Figure in which they are reported.

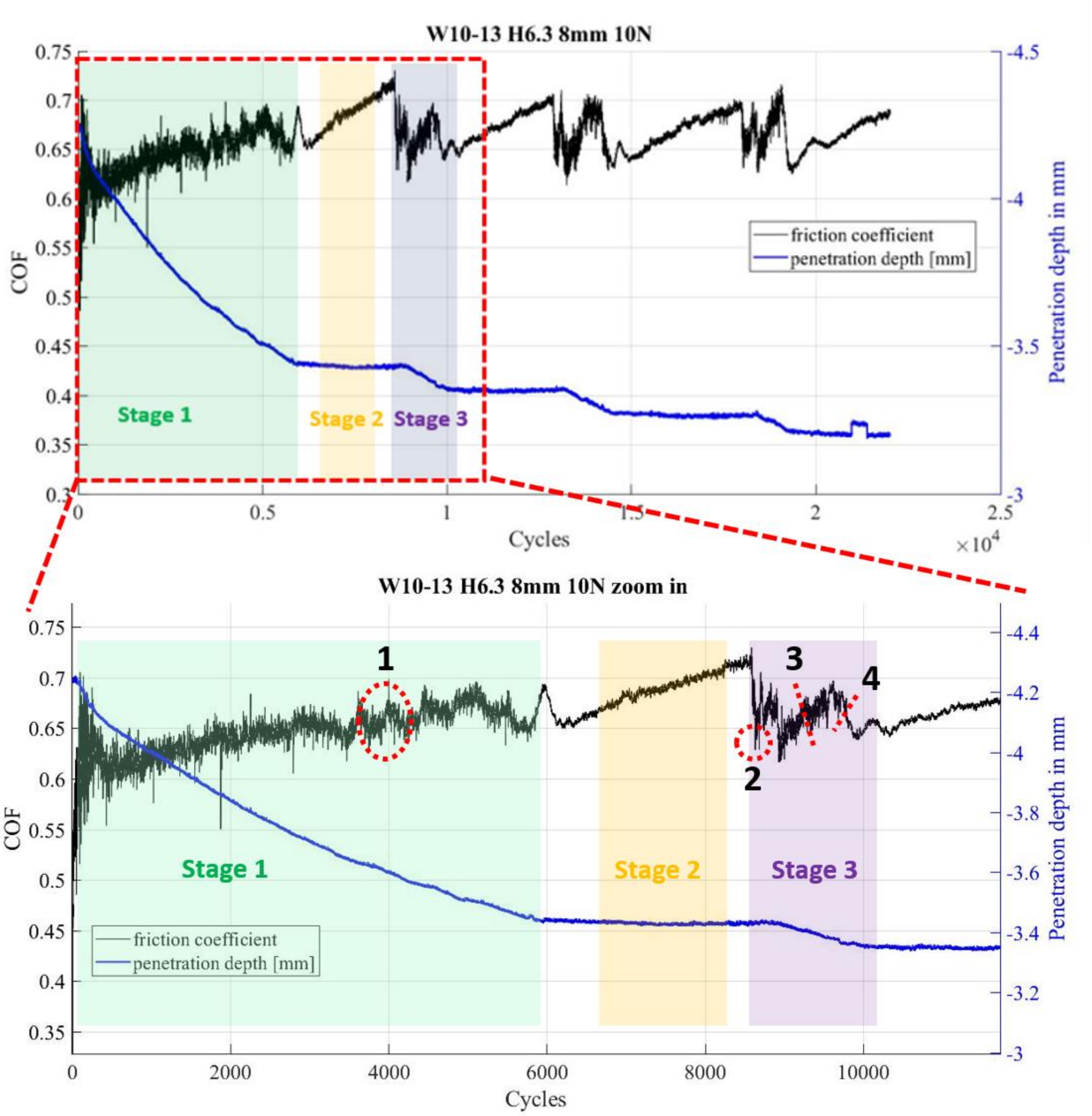

Figure 4.33: Zoom in of the graph derived by tribometer test used as reference. The four zones chosen for the interrupted tests are marked with red circles.

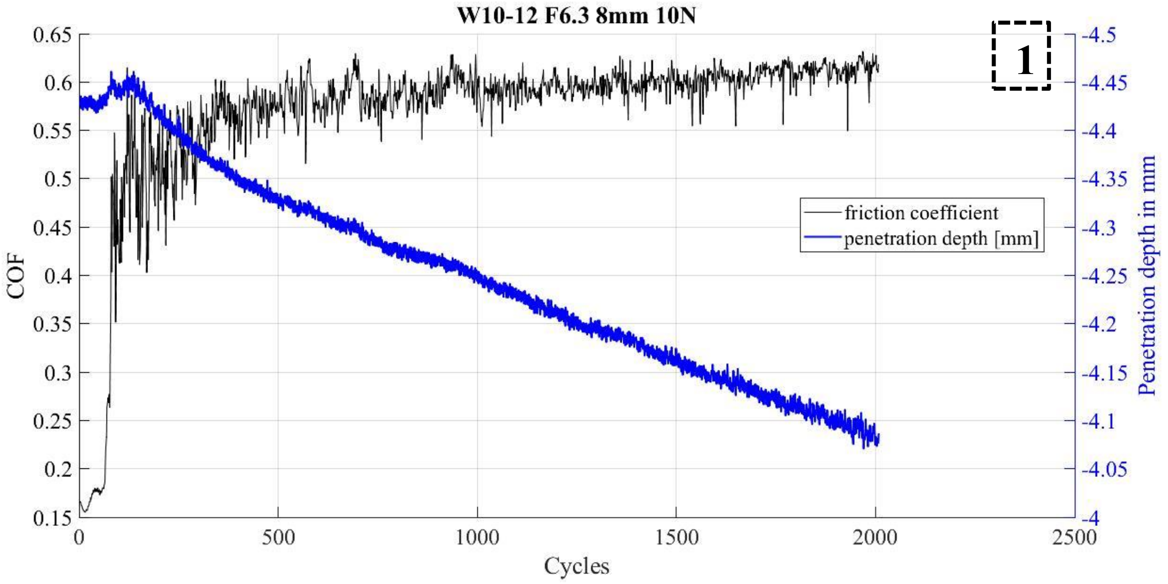

Figure 4.34: First interrupted test. W10-12 F6.3 with radius 8mm.

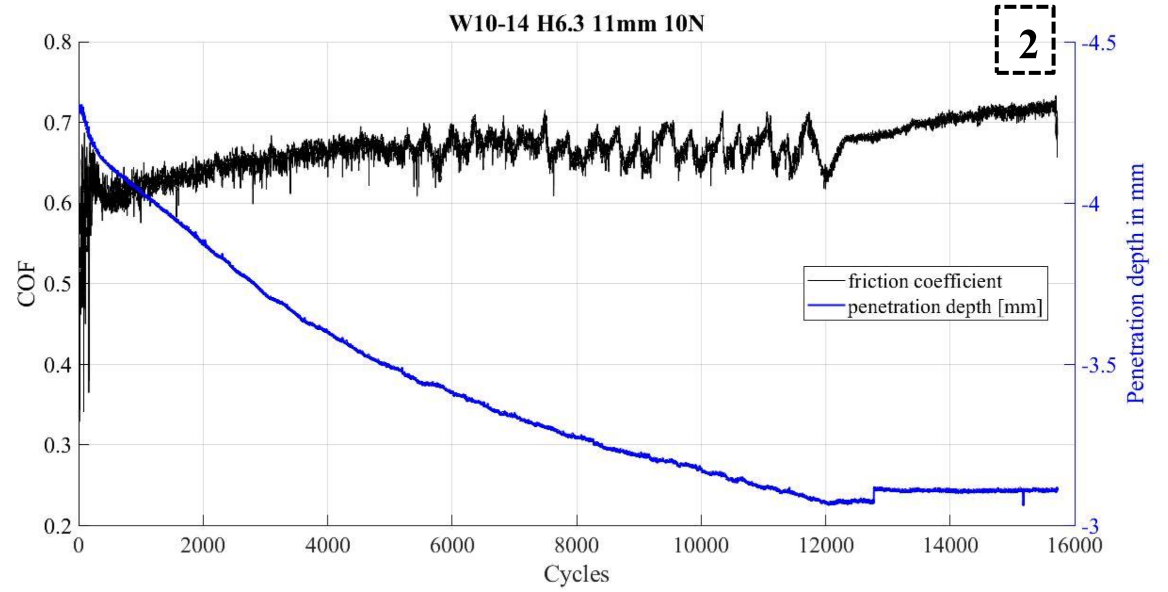

Figure 4.35: Second interrupted test. W10-14 H6.3 with radius 11mm.

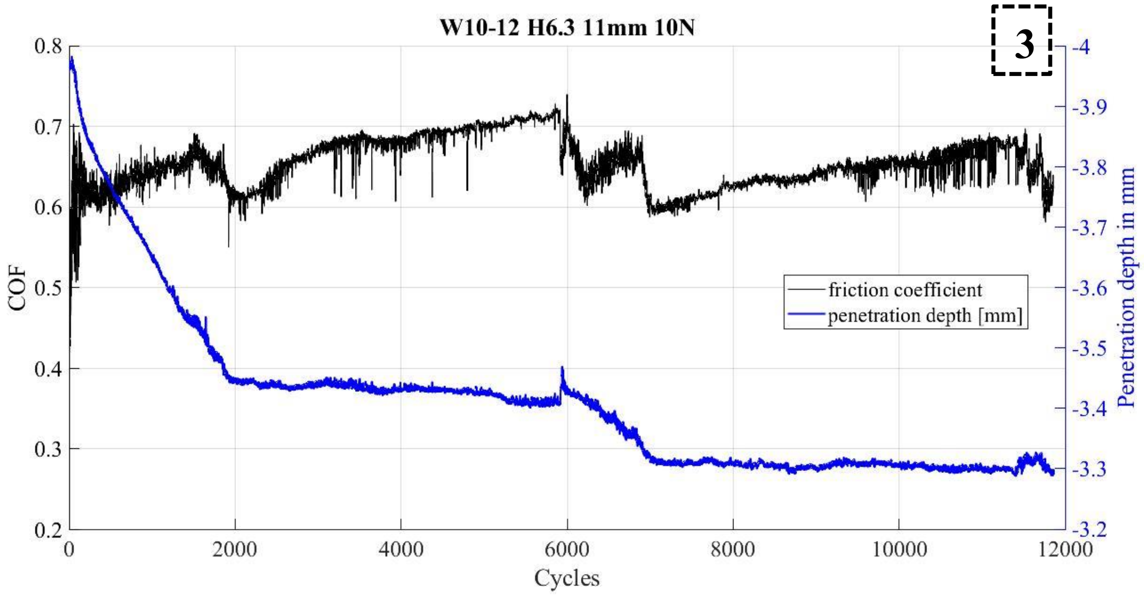

Figure 4.36: Third interrupted test. W10-12 H6.3 with radius 11mm.

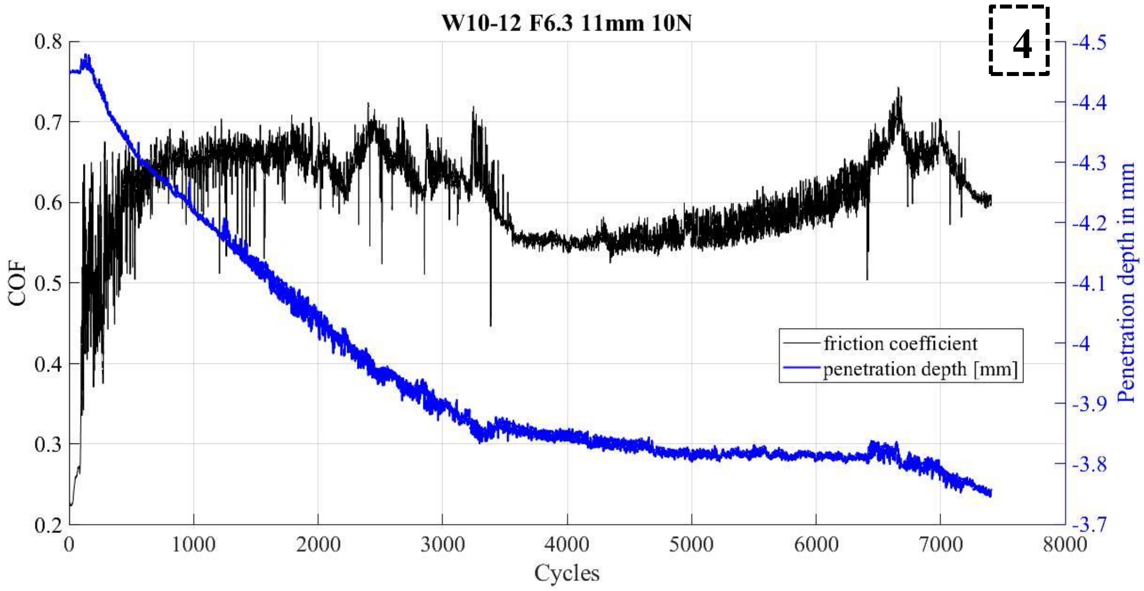

Figure 4.37: Fourth interrupted test. W10-12 F6.3 with radius 11mm.

The targets previously chosen were successfully achieved. In fact, every interrupted test corresponds to the points marked in the Figure 4.33. The first interrupted test (Figure 4.34) is in the middle of the first wear behaviour stage, where COF slightly increases showing many small peaks and valleys and the penetration depth increases. The second interrupted test (Figure 4.35) is in the third wear behaviour stage, precisely as soon as a sudden decrease of COF occurred with still a constant penetration depth. The third interrupted test (Figure 4.36) is in the third wear behaviour stage as well, but in this case the penetration depth is starting to increases. The fourth interrupted test (Figure 4.37) is in the third wear behaviour stage, when the curve of penetration depth is at the end of its increase. Behaviour of friction coefficient and penetration depth curves correlate with wear behaviour stages of the interrupted tests are summarized in Table 4.6.

	Interrupted test	**Wear behaviour stage**	**COF curve behaviour**	**Penetration depth curve behaviour**
Figure 4.34	1	1	slightly increases	increases
Figure 4.35	2	3	suddenly decreases	constant
Figure 4.36	3	3	increases	starts to increases
Figure 4.37	4	3	decreases	end of its increases

Table 4.6: Description of COF and penetration depth curve at the end of each interrupted test.

4.3.2 *Profilometer*

After each tribometer test performed, the track and the alumina ball analysis were analyses by means of profilometer scans in order to get the worn volume of the sample and of the counter-body. By means the use of a specific tool during the profilometer analysis has been possible to obtain directly the measure of the worn volume of the track. The worn volume of the alumina ball has been calculated from the worn ball depth and its radius [7]. The worn ball depth has been obtained by profilometer measure. The most representative profilometer images of the tracks and one example of the alumina ball during the analysis are shown in this section.

Figure 4.38 represent a track obtained after uninterrupted tribometer test on the sample W10-13 H 11.3 with radius 8mm. It may be noted that the track is not completely homogeneous. The zoom in of the Figure 4.38 shows a deeper track (dark pink colour) in the zone with less carbides. On the other hand, where the amount of carbides is greater the track is more protected (blue colour).

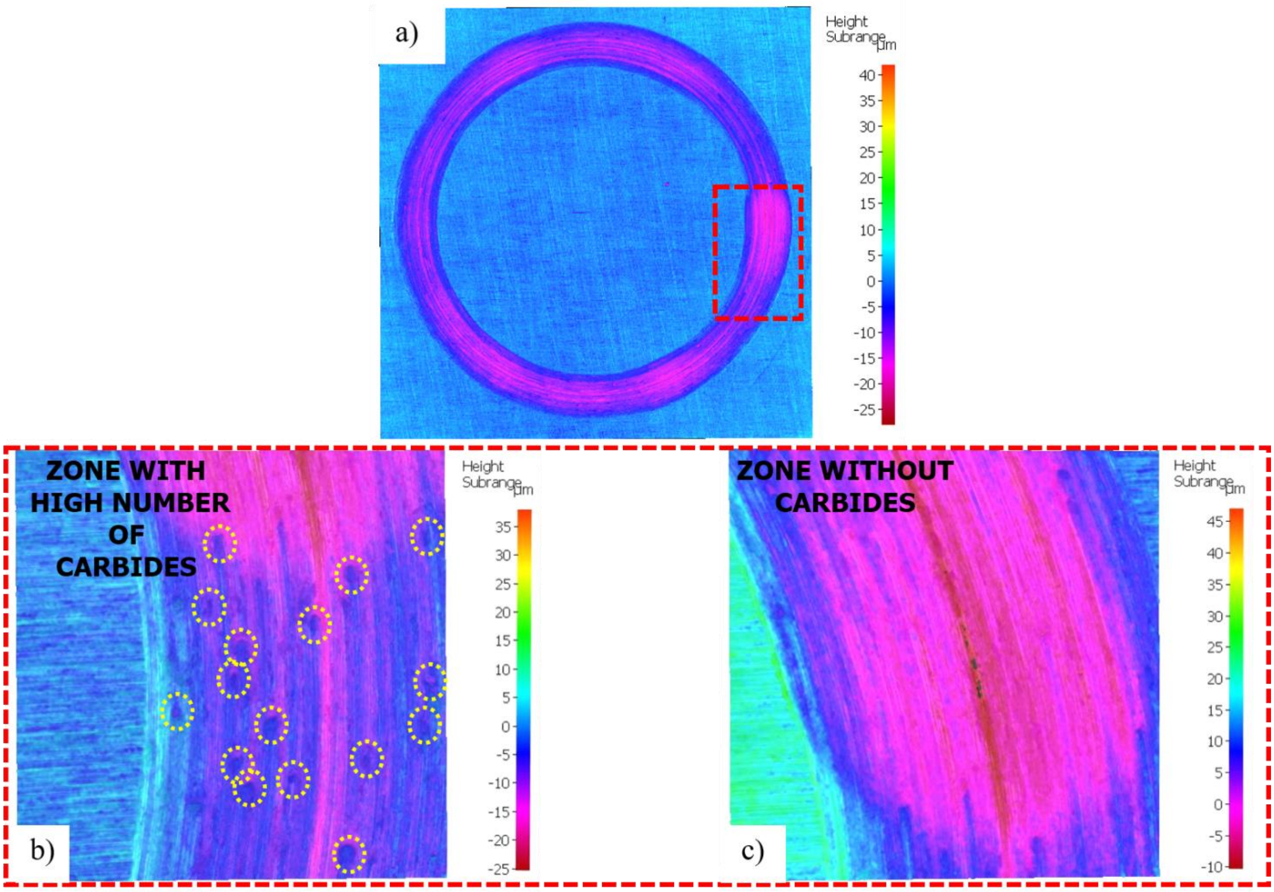

Figure 4.38: a) W10-13 H11.3 8mm radius 10N force worn track profilometer overview; b) zoom in of the Figure 4.38 a) where the protection of the carbides is shown; c) zoom in of the Figure 4.38 a) where a zone without carbides exhibits a deeper wear.

Figure 4.39 shows a track on the sample W10-12 H 11.3 with radius 8mm after uninterrupted test in which it may be seen as the depth of the track is not homogeneous, as in Figure 4.38.

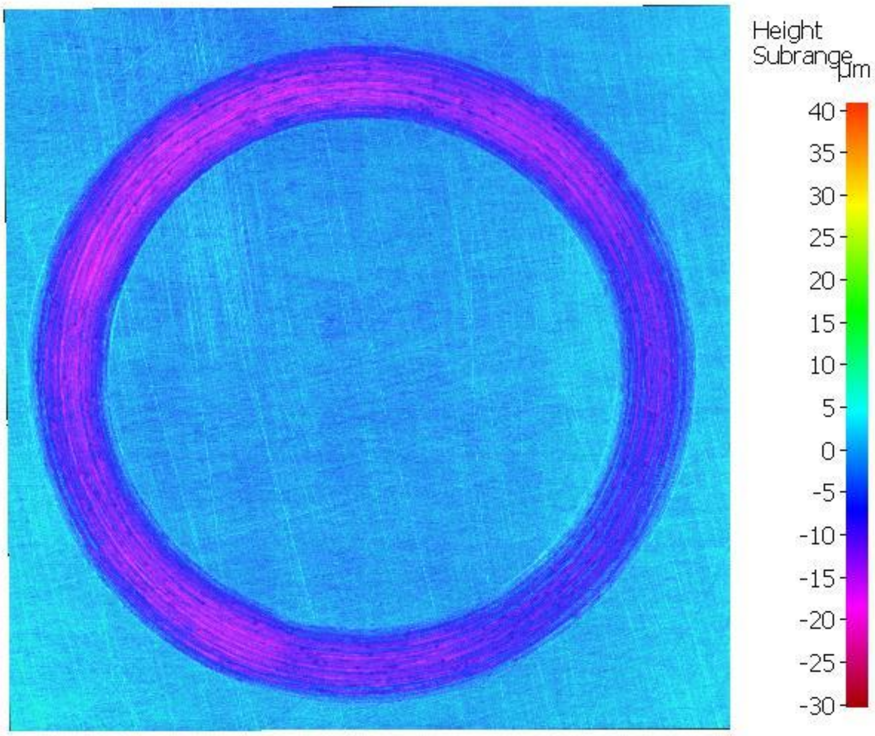

Figure 4.39: W10-12 H 11.3 8mm radius 10N force worn track profilometer overview.

Figure 4.40 shows two different interrupted tribometer tests with 8 mm and 11 mm radius on the sample W10-12 F 6.3. The two tracks in Figure 4.40 being interrupted tests are slightly less deep than Figure 4.38 and 4.39. Also in the case of interrupted tests may be observed a little difference in the worn depth along the track.

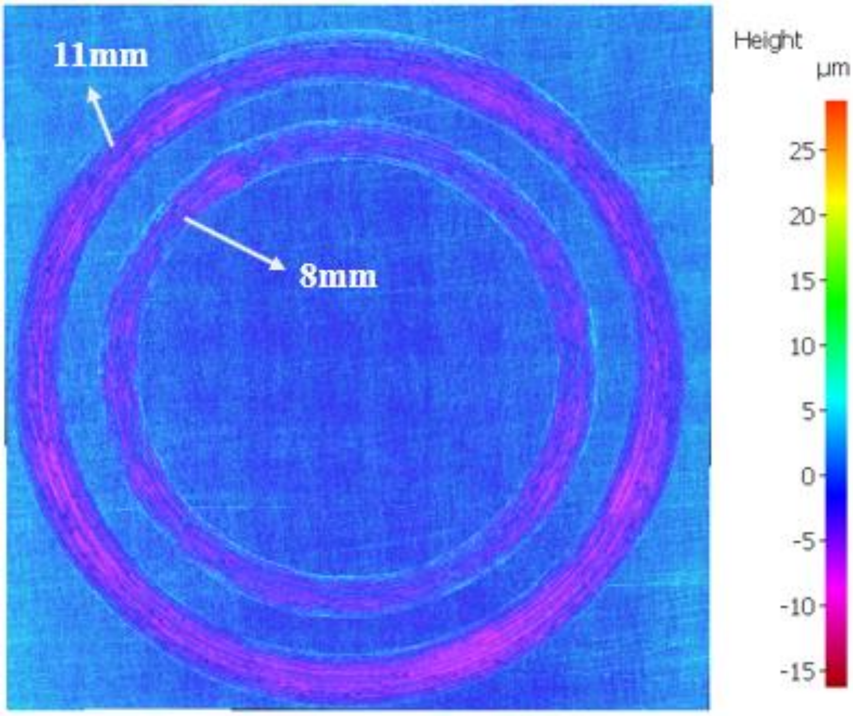

Figure 4.40: W10-12 F 6.3 8-11mm radius 10N force worn track profilometer overview.

A general overview concerning the track worn volume of each sample obtained after wear test are summarized in Table 4.7.

		SAMPLE	**WORN VOLUME [mm^3]**
NOT INTERRUPTED TESTS (22000 cycles)		W10-13 F1.3 8mm	0.6
		W10-13 F6.3 8mm	1.4
		W10-13 H6.3 8mm	1.1
		W10-13 H11.3 8mm	0.9
		W10-12 F1.3 8mm	1.2
		W10-12 H11.3 8mm	1
		W10-14 F6.3 11mm	2.7
INTERRUPTED TESTS	**2000 cycles**	W10-12 F6.3 8mm	0.2
	15500 cycles	W10-14 H6.3 11mm	1.6
	12000 cycles	W10-12 H6.3 11mm	0.6
	7500 cycles	W10-12 F6.3 11mm	0.5

Table 4.7: Worn volume of each track of the post-mortem samples calculated directly with profilometer.

As mentioned before, the worn volume of alumina ball was also calculated for each test performed. Tracing a profile along the diameter of the alumina ball it has been possible to get the worn ball depth with profilometer measure as shows Figure 4.41.

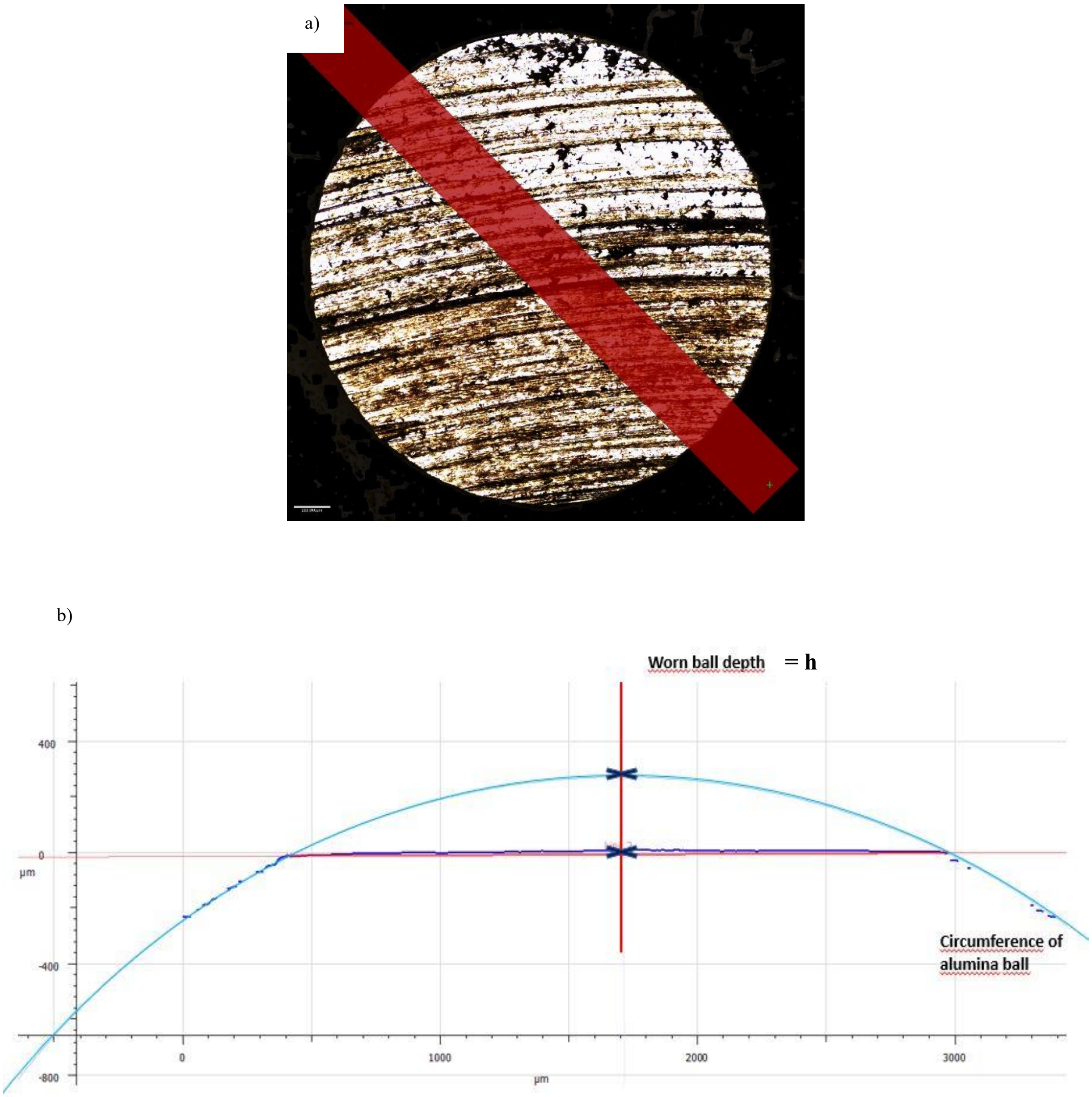

Figure 4.41: a) Profile along the diameter of alumina ball of the W10-12 F 6.3 sample with radius 8mm after tribometer test; b) worn ball depth calculated with profilometer.

To get the alumina ball worn depth it was used the Formula (1) in section 3.6 and the value obtained based on Figure 4.41 is shown in Table 4.8.

Alumina ball radius [mm]	Alumina ball worn depth [μm]
3	264

Table 4.8: Radius and measurement of alumna ball worn depth of the W10-12 F 6.3 sample with radius 8mm.

A general overview regarding the worn volume of alumina ball for each sample obtained after wear test are summarized in Table 4.9.

		SAMPLE	**ALUMINA BALL WORN VOLUME [mm^3]**
NOT INTERRUPTED TESTS (22000 cycles)		W10-13 F1.3 8mm	0.29
		W10-13 F6.3 8mm	0.81
		W10-13 H6.3 8mm	0.49
		W10-13 H11.3 8mm	0.36
		W10-12 F1.3 8mm	0.64
		W10-12 H11.3 8mm	0.47
		W10-14 F6.3 11mm	1.15
INTERRUPTED TESTS	**2000 cycles**	W10-12 F6.3 8mm	0.07
	15500 cycles	W10-14 H6.3 11mm	0.68
	12000 cycles	W10-12 H6.3 11mm	0.22
	7500 cycles	W10-12 F6.3 11mm	0.25

Table 4.9: Alumina ball worn volume of each track of the post-mortem samples calculated with Formula (1), section 3.6.

4.3.3 SEM images

The post-mortem sample obtained after wear tests were analysed by means of SEM analyses. At the end of tribometer tests the wear behaviour may be different (section 4.3.1) and consequently also the surface along the tracks. For this reason, several SEM images of different samples in a different mode (BSE and SE) were taken and they are shown in this section.

4.3.3.1 Uninterrupted test

Regarding the uninterrupted tests, the surfaces of those tests exhibit similar features (with the exception of the sample W10-14 F6.3) since those tests are stopped at the same position (stage 2). W10-13 H6.3 surface is chosen to be described since for each not interrupted test the wear stage is similar.

As shows Figure 4.42 (BSE mode) the surface present brighter and darker zone. The large bright carbides may be completely, partially and/or not broken.

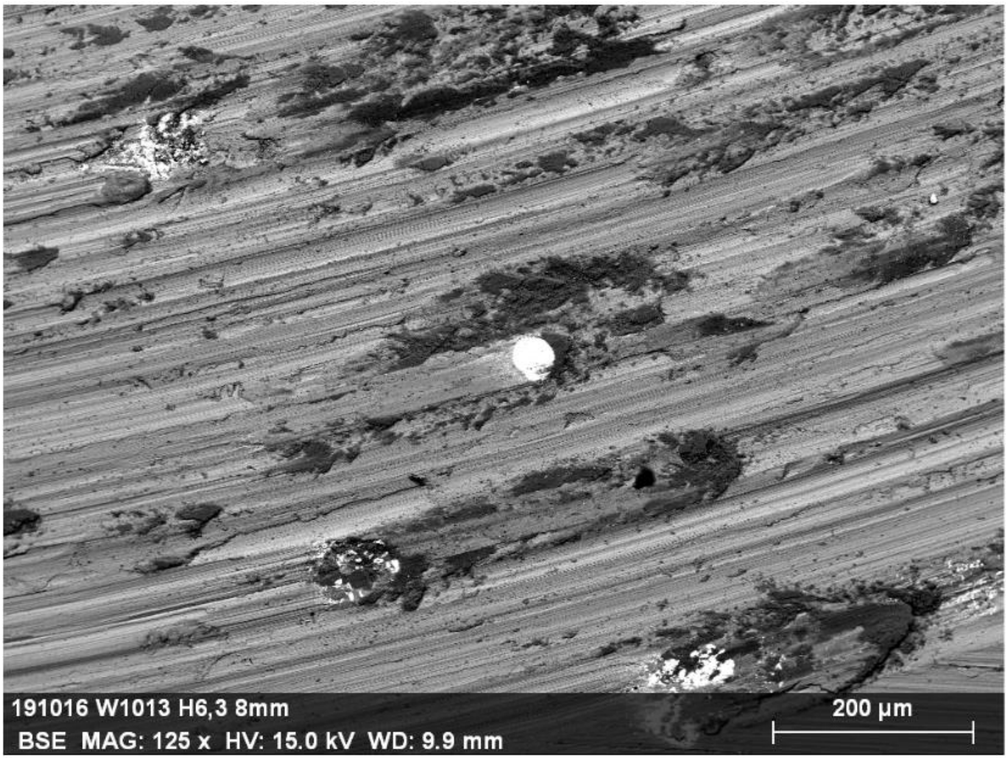

Figure 4.42: Detail of the worn track after uninterrupted test of the sample W10-13 H 6.3 with radius 8mm.

When carbide is partially broken the stacking of material occurs in front of it occur as shows Figure 4.43 a). Partially and completely broken carbides lead to over spread small pieces of WC near to the initial carbide, as it can be seen in Figure 4.43.

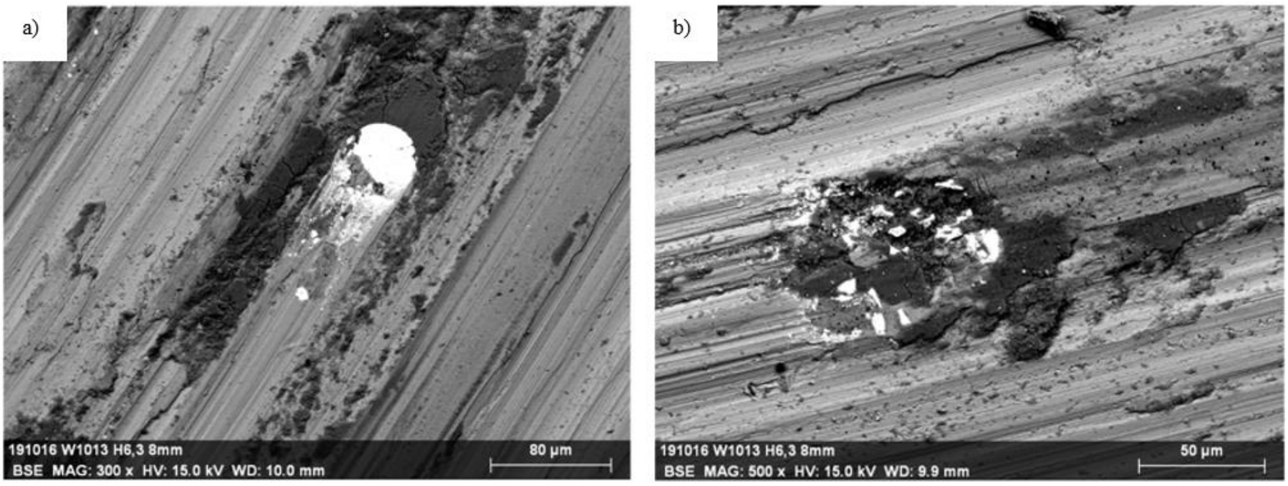

Figure 4.43: a) Partially broken carbide and stack of the material; b) completely broken carbide.

Observing the cross-section of those wear tracks, brighter oxides above the matrix may be recognised by means EDS composition, as reported in Figure 4.44. The percentage in mass of the chemical analysis 1 is reported in Table 4.10 in which a relative high amount of oxygen and aluminium are present.

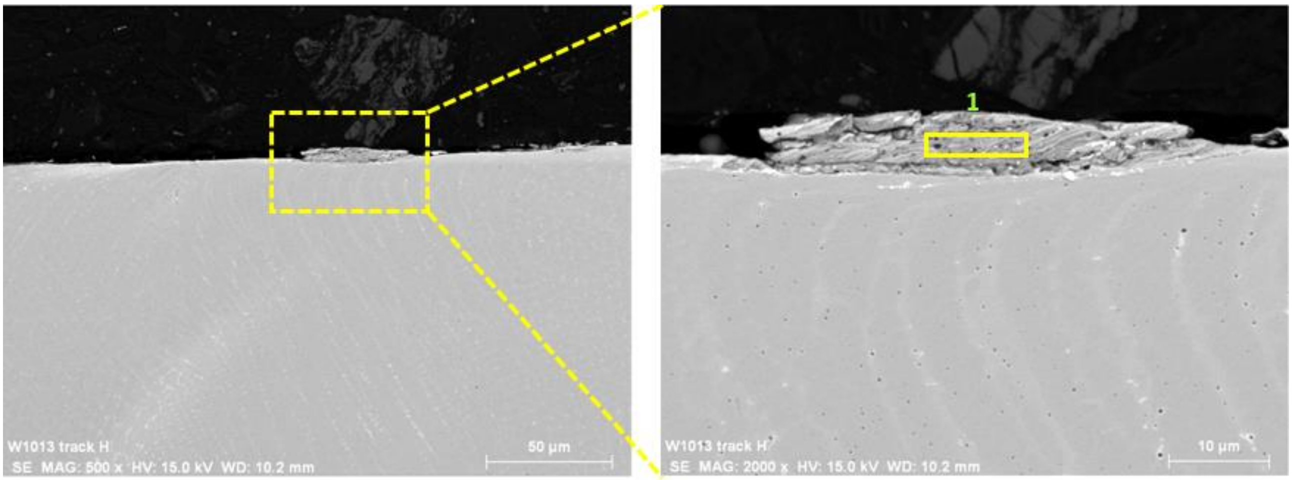

Figure 4.44: EDS analysis region of the cross section of the wear track parallel with respect to the movement of the sample against alumina ball. Presence of bright oxide on the surface.

Mass %	C	O	Cr	Fe	Al	W	Ni	Si	Mo	Mn
Zone 1	2.15	16.73	11.81	45.78	5.82	6.22	8.45	0.18	1.89	0.96

Table 4.10: Percentage in mass of each element present in chemical analysis 1 of Figure 4.44 derived by EDS analysis.

Chemical analysis 2 is described in Table 4.11. Darker oxide is present on the matrix, as Figure 4.45 shows.

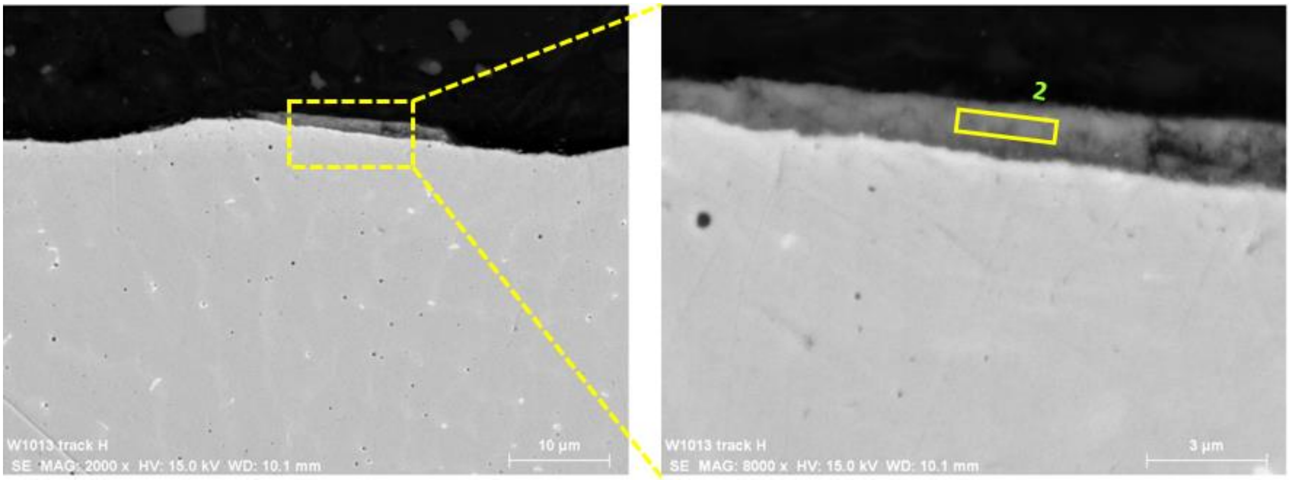

Figure 4.45: EDS analysis region of the cross section of the wear track transversal with respect to the movement of the sample against alumina ball. Presence of dark oxide on the surface.

Mass %	C	O	Cr	Fe	Al	W	Ni	Si	Mo	Mn
Zone 2	26.05	28.32	5.4	21.93	5.63	7.67	4.17	0	0.39	0.43

Table 4.11: Percentage in mass of each element present in chemical analysis 2 of Figure 4.45 derived by EDS analysis.

4.3.3.2 First interrupted test

The first interrupted test was carried out on the sample W10-12 F6.3 with radius 8mm. The test was stopped at ~ 2000 cycles (Figure 4.34). Presence of dark and brighter stacking of the material pretty compact may be noted after the wear test, as reported in Figure 4.46.

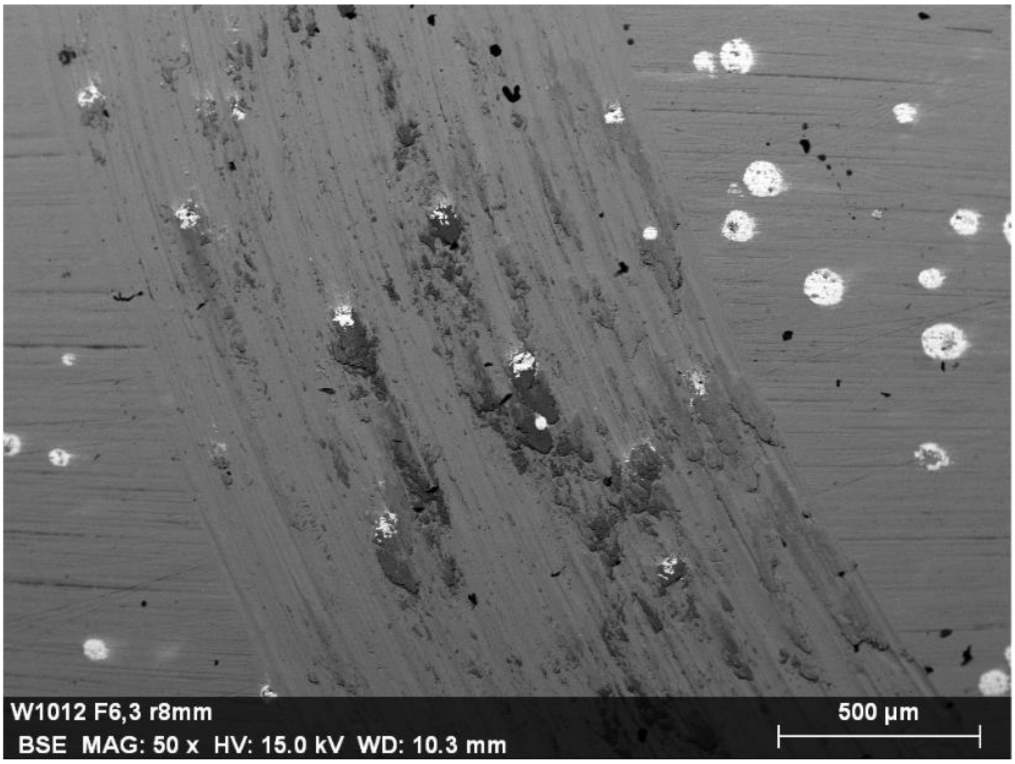

Figure 4.46: Detail of the worn track after the first interrupted test of the sample W10-12 F 6.3 with radius 8mm. Many stacks of the material in front of carbides are present.

SE mode was used to emphasize the presence of grooves and stacking of material in front of the carbides (Figure 4.47).

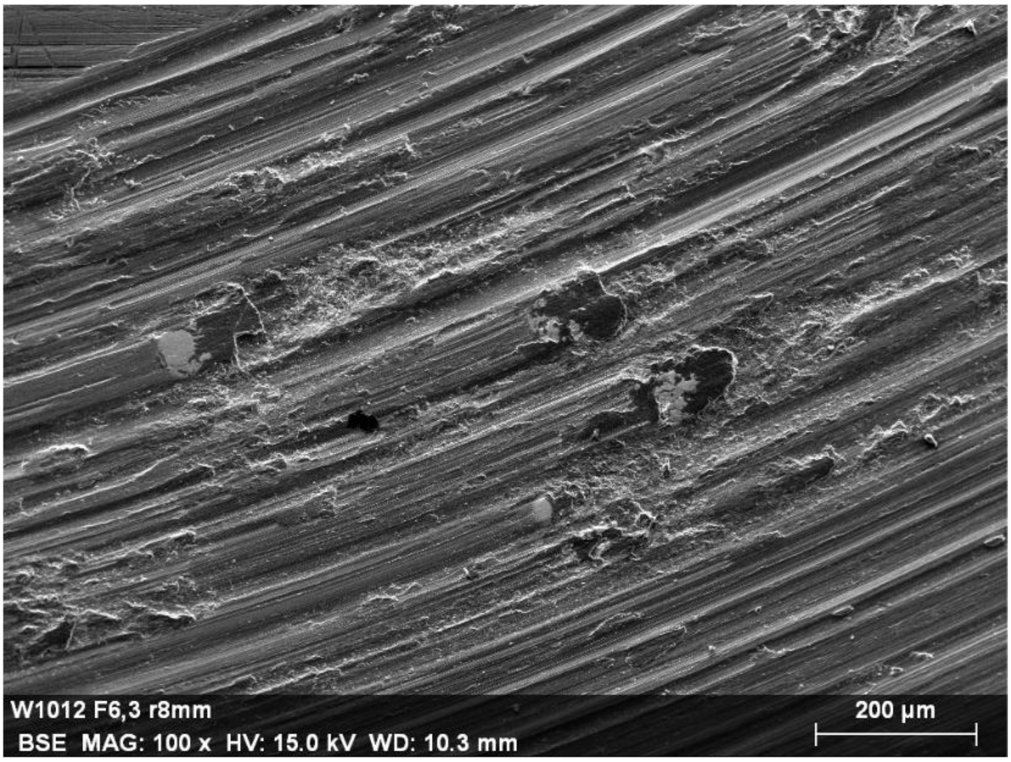

Figure 4.47: Details of the track of the sample W10-12 F6.3 with 8mm radius in secondary electrons mode.

EDS chemical analyses shown in Figure 4.48 were taken to demonstrate the presence of two different types of oxides. Table 4.12 exhibits as the chemical analysis 1 is characterized by very high amount of aluminium and oxygen, whereas chemical analysis 2 exhibits high amount of oxygen and higher percentage of chromium than chemical analysis 1. Instead, the presence of aluminium is lower than chemical analysis 1.

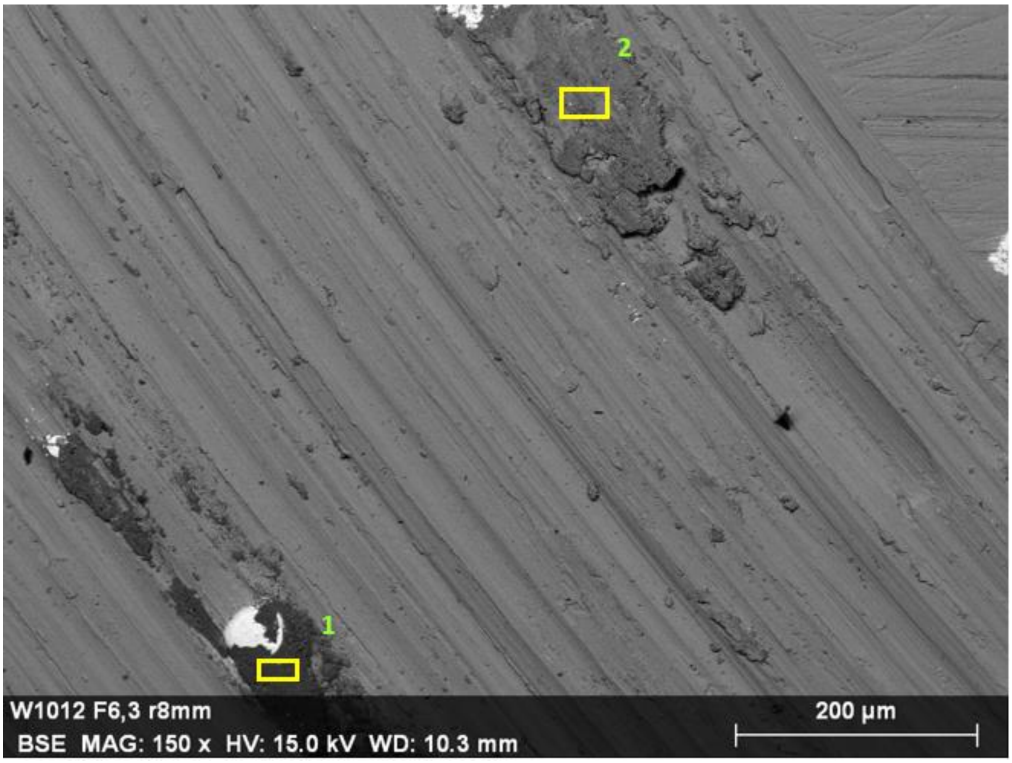

Figure 4.48: EDS composition regions on the stack of the material in front of carbides.

Mass %	C	O	Cr	Fe	Al	W	Ni	Si	Mo	Mn
Zone 1	1.93	37.48	5.91	24.83	20.77	3.11	4.59	0	0.83	0.56
Zone 2	2.28	18.79	10.79	46.25	6.47	3.50	9.48	0	1.46	0.99

Table 4.12: Percentage in mass of each element present in chemical analyses 1 and 2 of Figure 4.48 derived by EDS analysis.

After the cut of some part of the track the SEM investigation confirm a mixture of oxides. Black spots may be clearly recognised with very high quantity of aluminium (Figure 4.49 b), Table 4.13). The oxides are well linked and embedded into the matrix. Plastic deformation occurs in the matrix as shows Figure 4.49 a).

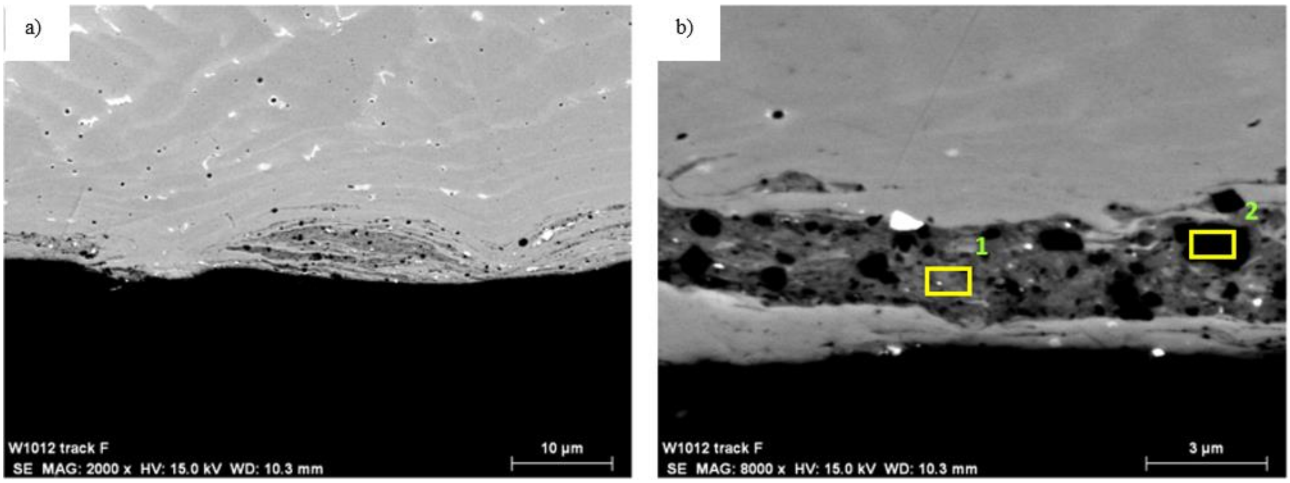

Figure 4.49: a) EDS analysis of the cross section of the wear track transversal with respect to the movement of the sample against alumina ball; b) plastic deformation of the matrix.

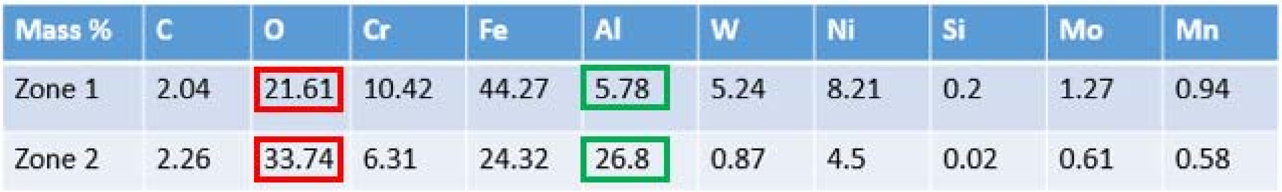

Mass %	C	O	Cr	Fe	Al	W	Ni	Si	Mo	Mn
Zone 1	2.04	21.61	10.42	44.27	5.78	5.24	8.21	0.2	1.27	0.94
Zone 2	2.26	33.74	6.31	24.32	26.8	0.87	4.5	0.02	0.61	0.58

Table 4.13: Percentage in mass of each element present in chemical analyses 1 and 2 of Figure 4.49 derived by EDS analysis.

4.3.3.3 Second interrupted test

The second interrupted test was performed on the sample W10-14 H6.3 with radius 11mm. The test was stopped at ~ 155000 cycles (Figure 4.35). In Figure 4.50, chemical analysis 1 exhibits the presence of oxygen and low amount of aluminium, whereas chemical analysis 2 shows presence of oxygen, higher amount of aluminium and very high percentage of tungsten (Table 4.14). Small parts of WC are over spread in the track, as it can be seen in Figure 4.50 b).

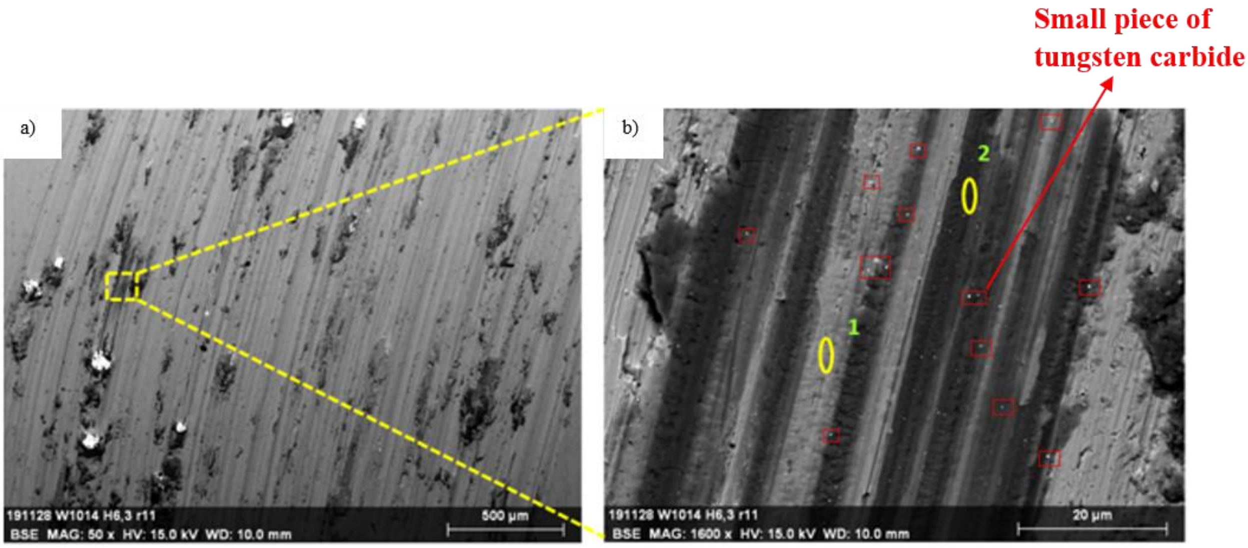

Figure 4.50: a) EDS composition regions of the second interrupted test on the W10-14 H6.3 sample with radius 11mm; b) many small pieces coming from broken carbide are recognised.

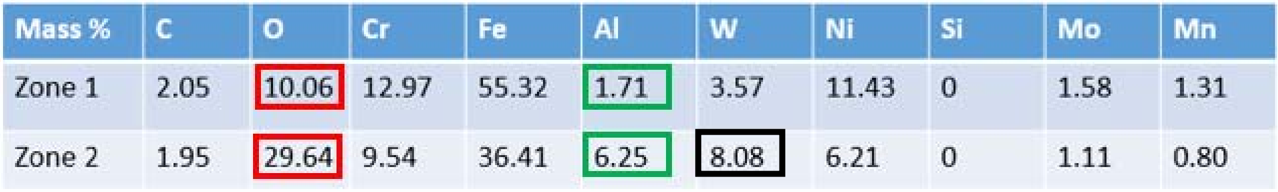

Mass %	C	O	Cr	Fe	Al	W	Ni	Si	Mo	Mn
Zone 1	2.05	10.06	12.97	55.32	1.71	3.57	11.43	0	1.58	1.31
Zone 2	1.95	29.64	9.54	36.41	6.25	8.08	6.21	0	1.11	0.80

Table 4.14: Percentage in mass of each element present in chemical analyses 1 and 2 of Figure 4.50 derived by EDS analysis.

The stacking of material in front of the carbides is not compact as shows Figure 4.51.

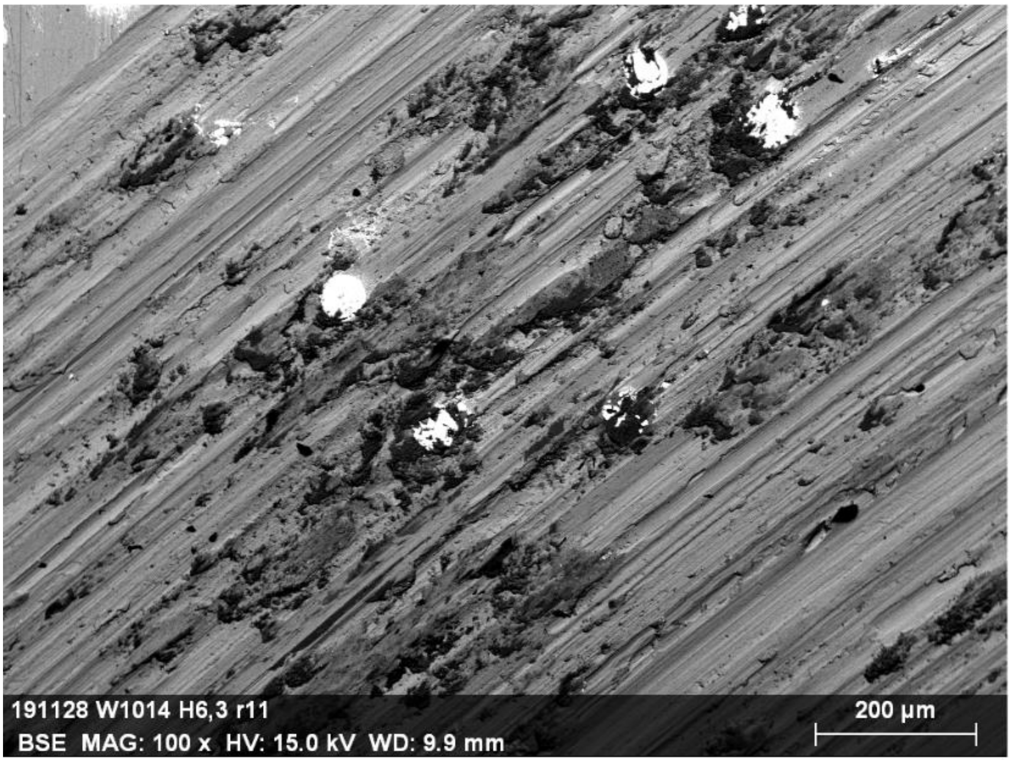

Figure 4.51: Detail of the stacking of the material over spread on the matrix and on carbides.

Heterogeneous composition on the track is evident after EDS analysis (Figure 4.52). Chemical analysis 1 is enriched of aluminium and oxygen, whereas chemical analysis 2 is enriched of oxygen and chromium as Table 4.15 shows.

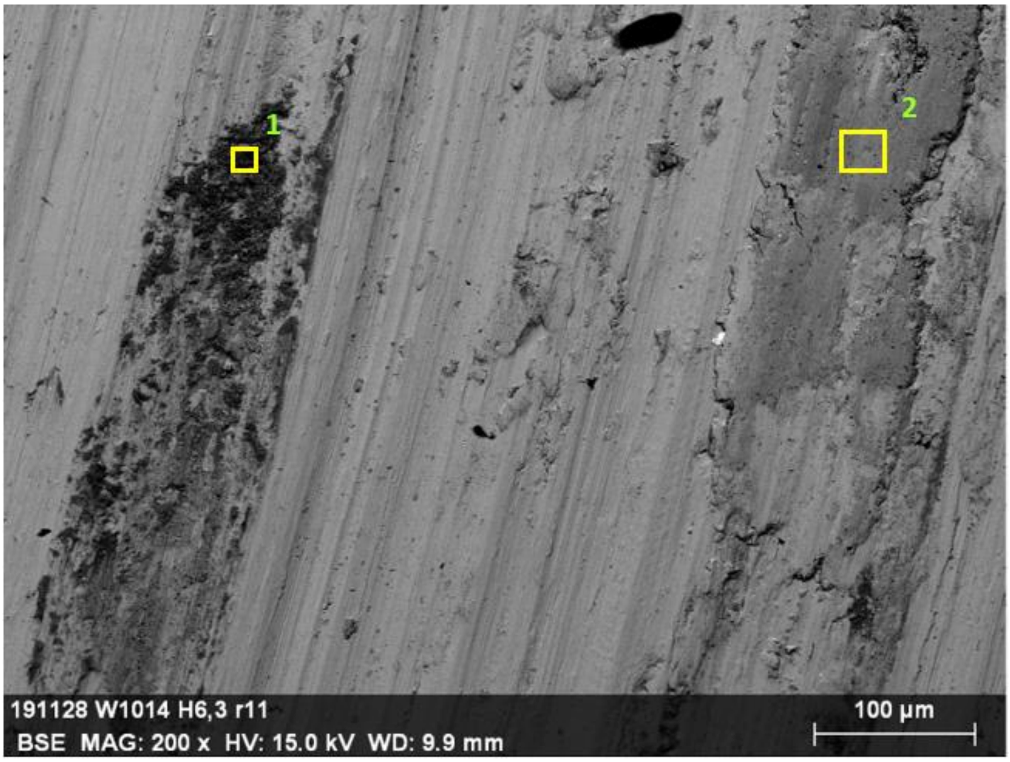

Figure 4.52: EDS composition of the second interrupted test.

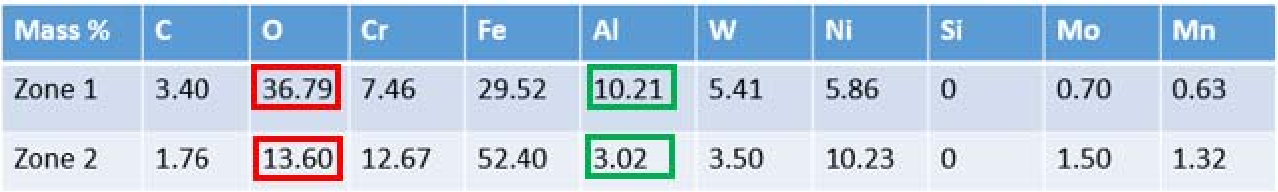

Mass %	C	O	Cr	Fe	Al	W	Ni	Si	Mo	Mn
Zone 1	3.40	36.79	7.46	29.52	10.21	5.41	5.86	0	0.70	0.63
Zone 2	1.76	13.60	12.67	52.40	3.02	3.50	10.23	0	1.50	1.32

Table 4.15: Percentage in mass of each element present in chemical analyses 1 and 2 of Figure 4.52 derived by EDS analysis.

4.3.3.4 Third interrupted test

The third interrupted test was carried out on the sample W10-12 H6.3 with radius 11mm. The test was stopped at ~ 12000 cycles (Figure 4.36). In Figure 4.53 stacking of material in front of carbides and very deep grooves may be recognised. Only bright zones are present.

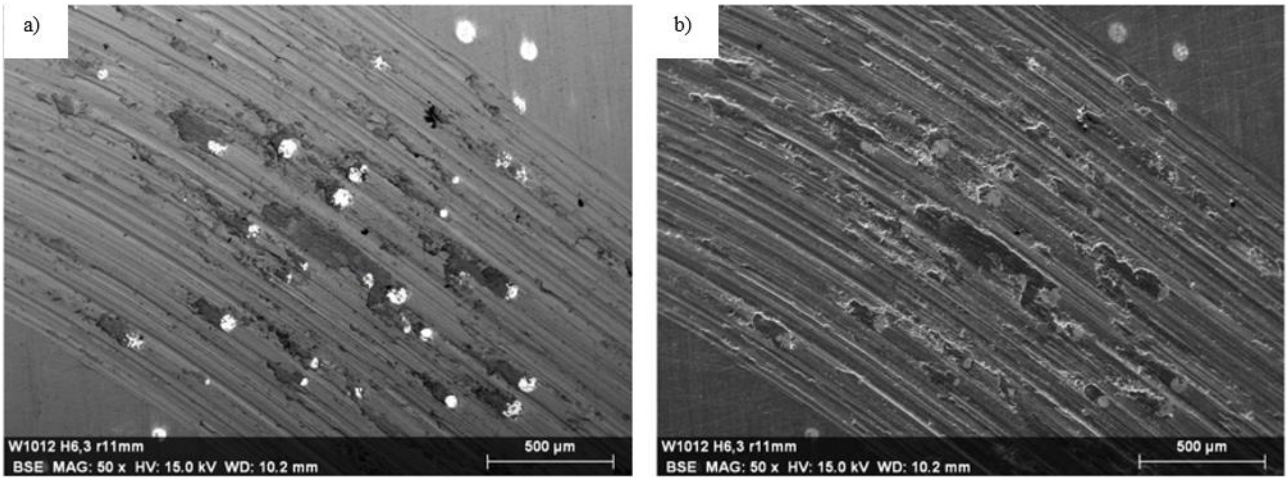

Figure 4.53: Detail of the track of the W10-12 H 6.3 sample with 11mm radius: a) BSE mode; b) secondary electrons mode.

Chemical analyses 1 and 2 in Figure 4.54 were analysed showing almost the same composition. Low amount of aluminium and presence of oxygen are in the track. Oxide is pretty homogeneous in composition (Table 4.16).

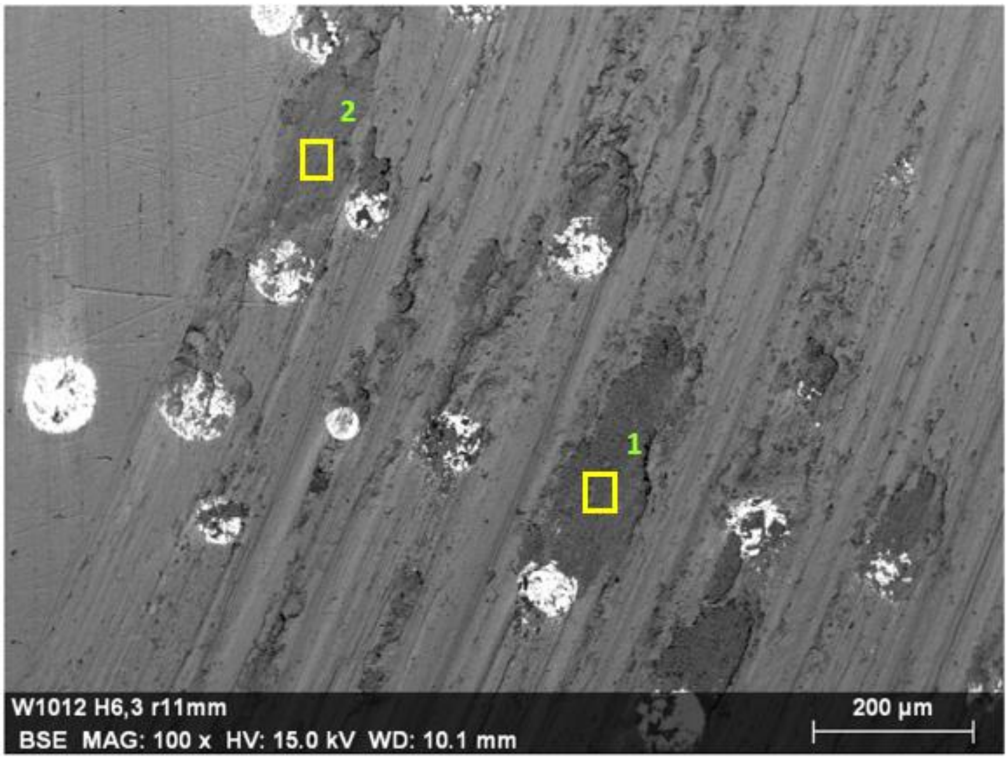

Figure 4.54: EDS composition regions of the third interrupted test.

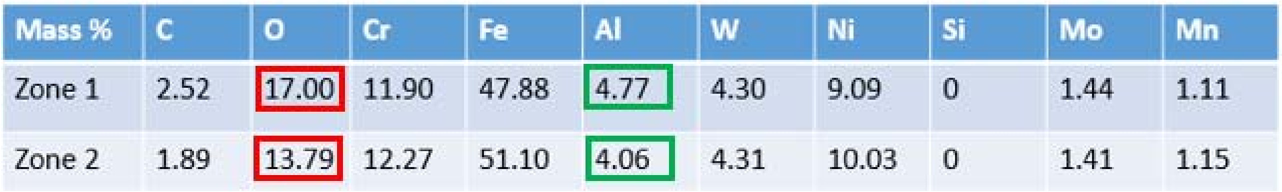

Mass %	C	O	Cr	Fe	Al	W	Ni	Si	Mo	Mn
Zone 1	2.52	17.00	11.90	47.88	4.77	4.30	9.09	0	1.44	1.11
Zone 2	1.89	13.79	12.27	51.10	4.06	4.31	10.03	0	1.41	1.15

Table 4.16: Percentage in mass of each element present in chemical analyses 1 and 2 of Figure 4.54 derived by EDS analysis.

The carbide in Figure 4.55 is partially covered by pretty compact stacking of material.

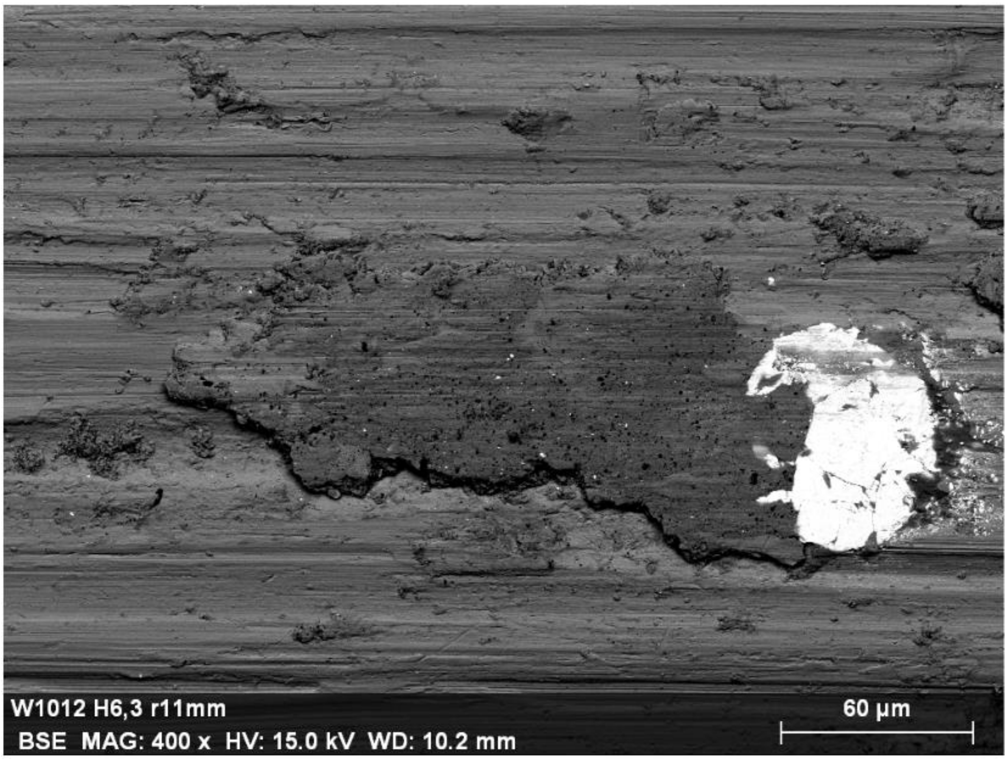

Figure 4.55: High magnification of stacking of the material close to the partially broken carbide.

After the cut of the track, EDS analysis were performed demonstrating the presence of compact oxide deposited on a side of the WC carbide (Figure 4.56 and its corresponding Table 4.17). Deformed matrix is observed in between the dark oxide and the cracked WC carbide. Different level between the surface of carbide and the matrix below the stacking material may be observed (red lines in Figure 4.56).

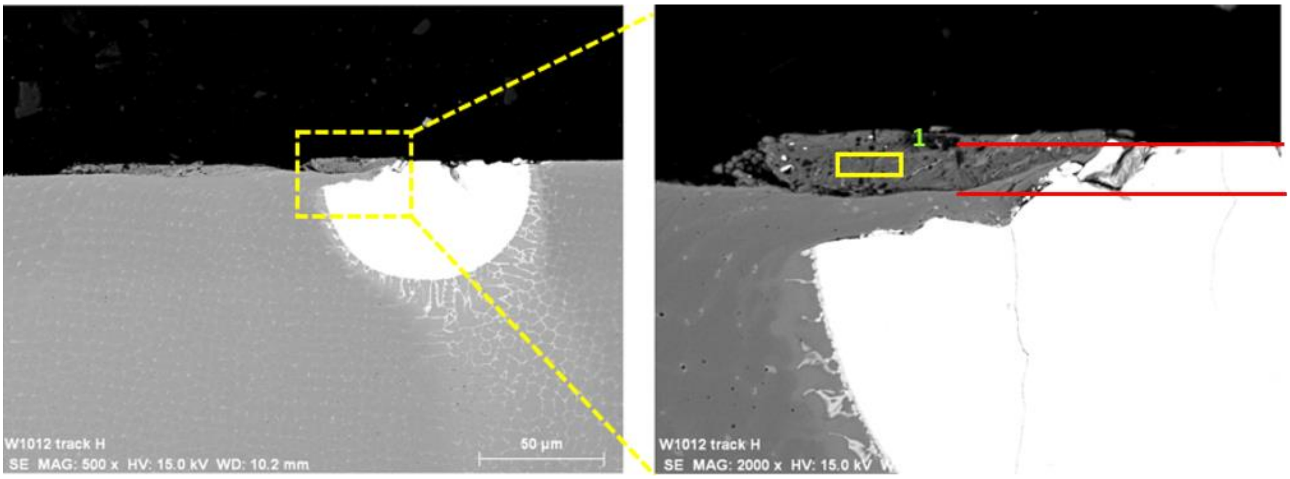

Figure 4.56: EDS analysis of the cross section of the wear track parallel with respect to the movement of the sample against alumina ball. Different levels between the matrix and the surface of carbide may be noted.

Mass %	C	O	Cr	Fe	Al	W	Ni	Si	Mo	Mn
Zone 1	2.14	20.72	10.82	46.65	3.72	3.55	9.43	0.16	1.55	1.25

Table 4.17: Percentage in mass of each element present in chemical analysis 1 of Figure 4.56 derived by EDS analysis.

4.3.3.5 Fourth interrupted test

The fourth interrupted test was carried out on the sample W10-12 F6.3 with radius 11mm. The test was stopped at ~ 7500 cycles (Figure 4.37). Figure 4.57 b) in SE mode exhibits quiet flat surface of the track after wear test.

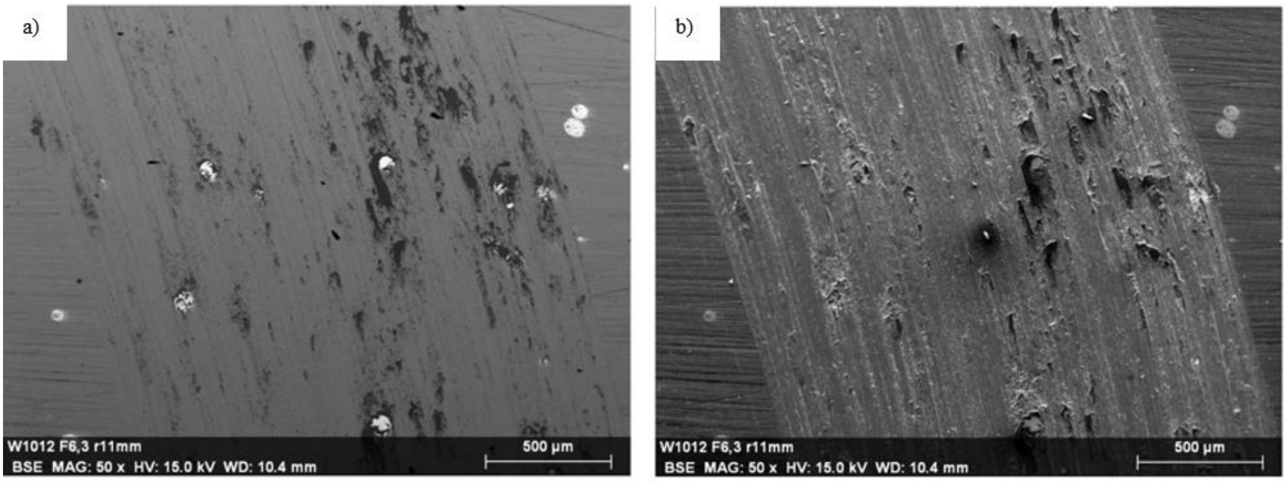

Figure 4.57: Detail of the track of the W10-12 F 6.3 sample with 11mm radius: a) BSE mode; b) secondary electrons mode.

Concerning Figure 4.58 and its relative Table 4.18, the chemical analysis 1 shows high amount of oxygen and chromium, with also presence of aluminium. Chemical analyses 2 and 3 are poorer of chromium and richer of aluminium than chemical analysis 1 with always presence of oxygen.

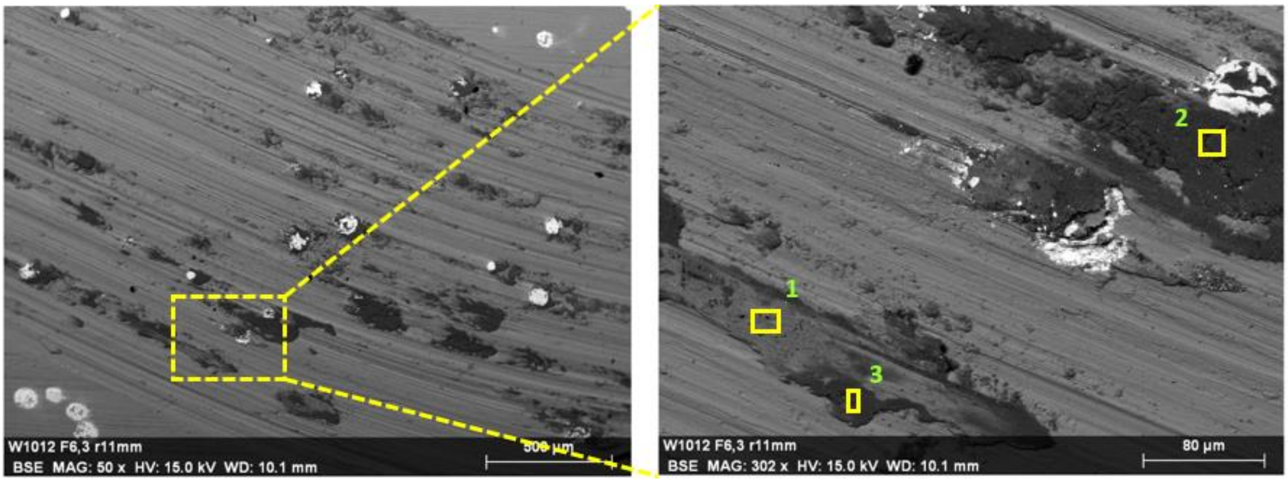

Figure 4.58: EDS analyses of the fourth interrupted test.

Mass %	C	O	Cr	Fe	Al	W	Ni	Si	Mo	Mn
Zone 1	1.88	15.04	12.26	48.38	6.58	4.75	8.76	0	1.41	0.95
Zone 2	2.06	44.66	4.84	18.32	10.25	6.65	3.34	0	0.47	0.42
Zone 3	2.33	39.06	6.34	25.12	14.64	6.71	4.59	0	0.65	0.55

Table 4.18: Percentage in mass of each element present in chemical analyses 1, 2 and 3 of Figure 4.58 derived by EDS analysis.

Oxide is over spread on the surface of the matrix. Small black spots may be seen into the oxide (Figure 4.59).

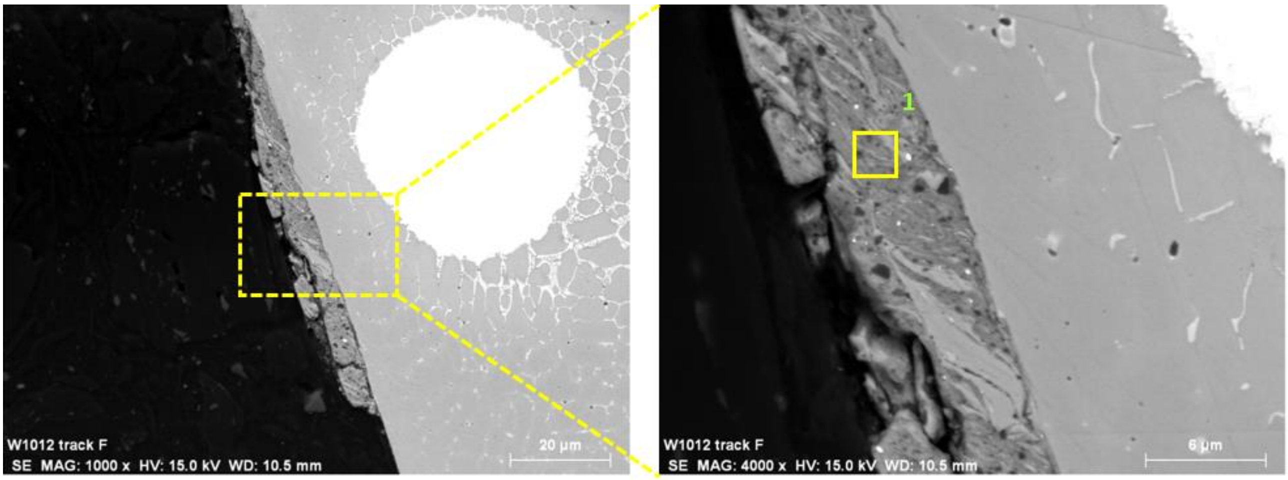

Figure 4.59: EDS analysis of the cross section of the wear track parallel with respect to the movement of the sample against alumina ball.

Mass %	C	O	Cr	Fe	Al	W	Ni	Si	Mo	Mn
Zone 1	2.22	23.96	9.9	42.17	6.95	3.83	8.29	0.25	1.37	1.06

Table 4.19: Percentage in mass of each element present in chemical analysis 1 of Figure 4.59 derived by EDS analysis.

Furthermore, the number of carbides in the track were also counted on SEM images and they are summarized in a Table 4.20. Only non-interrupted tests (22000 cycles) were considered in order to have a comparison between number of carbides and worn volume at the same number of cycles (22000 cycles).

SAMPLE	NUMBER OF CARBIDES
W10-13 F1.3 8mm	427
W10-13 F6.3 8mm	300
W10-13 H6.3 8mm	360
W10-13 H11.3 8mm	366
W10-12 F1.3 8mm	420
W10-12 H11.3 8mm	355
W10-14 F6.3 11mm	174

Table 4.20: Number of carbides in the track of post-mortem samples. Only uninterrupted tests are considered.

5. *Discussion*

The results shown in the previous chapter will be correlate to each other and explained in this section 5. First of all, the carbides distribution derived by the study of the composite with Optical microscopy and Stream Motion software will be explained. A good understanding regarding the microstructure of SS316L+10%WC was achieved by means the use of SEM analyses. EBSD, EDS together with the literature provided the discussion in the subchapter 5.2. Correlation between Vickers Hardness and thermal history will be explained as well, thanks to the data obtained by EBSD analyses and EDS profiles such as the grain size and the mean % of W, respectively. Finally, the wear behaviour of this metallic matrix composite will be explained considering the Profilometer measurements and SEM analyses performed, with a brief description concerning the reproducibility of the Tribometer tests.

5.1 Carbides distribution

According to Figure 4.5 b, image analysis of the cross-section of the raw WC carbides reveals a distribution in good agreement with the granulometry measurements carried out in previous works [7], but with the maximum of the distribution shifted at 75 µm. This shift is due to the observation of a section of the particle, instead of the actual size of the particles. The measurement was carried out with the purpose of compare the cross-section of the raw particles with the partially dissolved WC carbides in the microsctructure of the composite. Indeed, the maximum of the size distribution (Figure 4.6 d) in the composite is reached around a diameter of 40 µm since a partial or total dissolution of the WC powders occur during cladding due to the high temperatures and the contact with the molten metal.

Based on Figure 4.6 the carbides distributions are almost constant, despite small changes may be observed.This could be due to two phenomena:

- small feed variations during the LC process;
- being the virgin WC particles not exactly with the same size as it is shown in Figure 4.5 b), the smallest are completely melted in the matrix, whereas the biggest are partially melted. Thus, a local population of small powders lead to a local reinforced microstructure without WC carbides.

Figure 4.7 show the top layers of the composite, carbides with mainly small diameter are observed if compared with the rest of the material (Figure 4.6). This is due to the thermal history of the last track.

The remelting from the deposition of a further layer on the last track does not occur anymore and thus the carbides present in that region have more tendecy to be partially rather than completely dissolved. Therefore, the frequency of the carbides along Y direction in the top part is the largest (Figure 4.7 b).

5.2 Microstructure of SS316L+WC 10%

The microstructure of the SS316L+WC10% exhibits a complex reinforced microstructure as reported in section 4.1.2. SEM microscopy and EBSD analysis are considered together in order to identify phases with unique compositions. Different types of carbides were observed nearby of undissolved carbides, i.e. skeletal brighter, darker compact and lamellar carbides (Figure 4.9 and Figure 4.10), whereas in the track and away from the large WC only complex regular carbides were noted (Figure 4.11, point B and Figure 4.14, point B). In the HAZ only brighter compact carbides were found as Figure 4.14, point A shows.

As shown in Figure 4.18 b, all the phases in the pattern quality are well indexed due to their bright contrast. Based on Figure 4.19, the core of the big partially dissolved WC is identified as crystal of Qusongite (hexagonal WC), W_2C (orthorhombic) and Austenite (FCC). MC carbides match with FCC lattice that is sometimes mistaken for austenite [50]. Indeed, from the literature [23], it is possible to associate this lattice to the γ-WC_{1-x} that is the only tungsten carbide with a FCC crystal order. Furthermore, EDS analyses confirm the identification of a FCC crystal with high content of C and W. Being this carbide stable at 2600°C [23], the γ-WC_{1-x} is probably metastable and its presence at room temperature due to the high cooling rates of the gas atomization.

Into the carbide crown, traces of pure tungsten (BCC) may be noted (Figure 4.19) corresponding to the white particles with high percentage of W [49] (Figure 4.9 and Figure 4.10).

All the solidification carbides formed around the large WC carbide and the carbide crown are identified as FCC crystal lattice, as shown in Figure 4.19. The carbide crown is considered a modification of the γ-WC_{1-x} due to the exchange of elements during the interactions between molten metal and the WC powders. The Fe, Ni and Cr addition may enlarge the thermodynamic stability of the carbide to room temperature [49]. The FCC crystals orders of the solidification carbides are associated to darker compact carbides and skeletal brighter carbides (Figure 4.9). The darker compact carbides (Figure 4.11, E) exhibits an high Cr content, as Table 4.1 shows, suggesting that it may be associated to $(Fe,W)_{23}C_6$ [51]. Instead, the skeletal brighter carbides (Figure 4.11 point C) and their relative high amount of W [26] may be associated to $(Fe,W)_6C$ [52], [53]. Hence, $M_{23}C_6$ and M_6C are present depending on the W and Cr amount and are formed from the liquid during solidification. Indeed, their lattice structure is similar and the EBSD is not able to differentiate them completely.

The complex regular carbides are observed relatively far from the large WC carbides (Figure 4.11, point B) and in the track (Figure 4.14, point B). They exhibit a very high contents of W and Cr, as point B of Table 4.1 and Table 4.2 shows. The crystal lattice of this metastable carbide is distorted since EBSD analysis identifies and sometimes mistakes its FCC lattice for austenite (Figure 4.19). The chemical composition of the very last remaining liquid of the track, together with the high cooling rates achieved during deposition, may lead to this contraction of the crystal lattice [49]. Based on these considerations and on previous works [49], it can be assumed the complex regular carbide associated to $(Fe,W)_4C$ carbide due to its peculiar composition (point B of Table 4.1 and Table 4.2) and its metastable nature [49], [54], [55].

In the HAZ, the compact bright carbides are identified as FCC crystal lattice (Figure 4.21) and they can be associated to M_6C carbide due to their high W content (Table 4.2, point A). Regarding the matrix, it is indexed as FCC and identify as austenite with two different lattice parameters (Figure 4.19). This is due to the fact that during solidification are achieved very high cooling rate and more elements may be retained within the austenite crystal lattice leading to a distortion of the matrix [56]. As Table 4.1 points A and D show, traces of W are present, and they could be the reason of the lattice distortion.

5.2.1 Correlation between hardness and thermal history

According to the Figure 4.23 in section 4.2, it is clear as the Vickers hardness of the composite is greater than that of pure SS316L. The reinforcement of the matrix due to the presence of new solidification carbides and the partially dissolved carbides lead to enhance the hardness in the composite.

The result of the HV 10 test reported in Figure 4.23 shows an average hardness of the composite from the substrate (0 mm) to the core (6 mm) slightly lower than the upper part (from 6 to 12 mm) of the deposit. This observation may be appreciated in Figure 5.1, where the two vertical black lines emphasize what just mentioned.

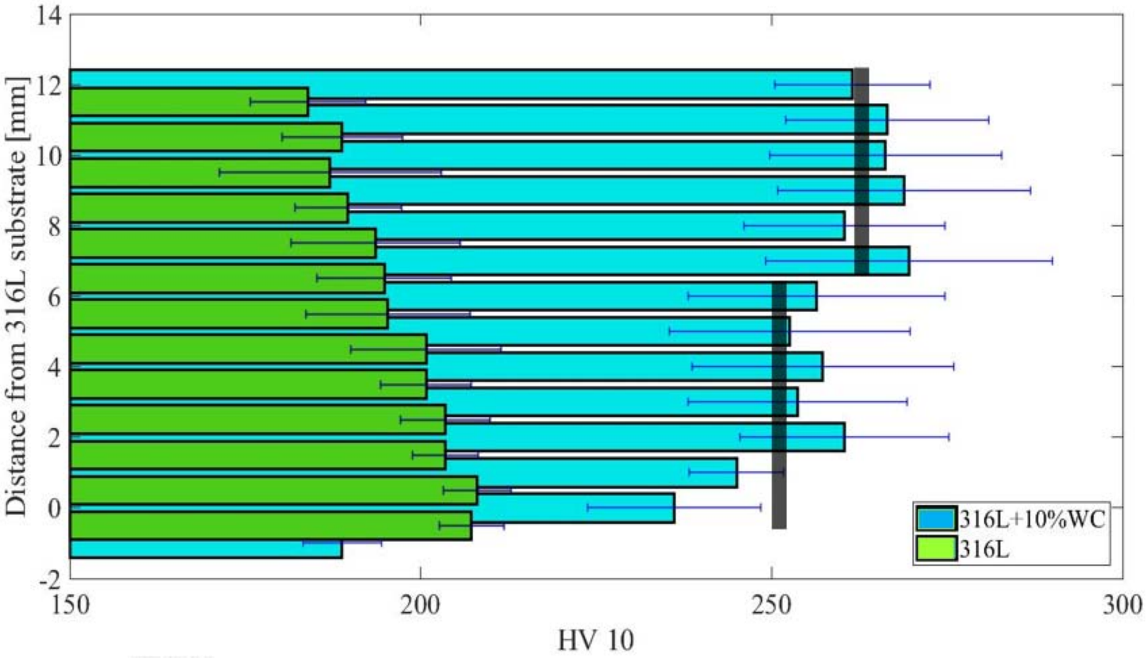

Figure 5.1: Results of hardness test for the 316L+10%WC composite and pure SS316L obtained by laser caladding. Vertical black lines represent the average hardness value of the composite in the lower and upper region of the cross section.

The grain size and the amount of the tungsten coming from the dissolution of carbides were evaluated in order to explain what is reason for which the hardness changes with the height of the deposit. The grain size was calculated by means EBSD analyses at 2 mm and 6 mm from the substrate, as shown in Table 4.3. Instead, the mean percentage in weight of W in the matrix was evaluated at 2, 6 and 10 mm from the substrate (Figure 4.17) by EDS analyses.

Being the substrate at room temperature the first deposited layers are characterised by the highest cooling rates corresponding to lowest grain size in the deposit (53 µm). The higher average W amounts were found at the middle and top of the deposit. Since from the classical theory, as the grain size decreases the hardness increases (in contrast with Figure 5.1 and Table 4.3), the key parameter to explain the hardness evolution in this composit might be not associated to the dimension of the grains. The amount of tungsten dispersed in the matrix could play a fundamental role in this material because it follows the same trend of the hardness of the composite. Furthermore, since the average temperature during the process of the LC process increases from the bottom to the top of the deposit (Figure 2.8) [57], also the fluctuations of carbides due to the Marangoni effect [58] might become more relevant moving away from the substrate. Therefore, the dissolution of carbides could be slightly stronger with the increase of the average temperature.

This could explain the higher amount of tungsten in the core and near to the top respect in the zone close to the substrate. The tungsten dispersed in the liquid may arrange in the crystal lattice of the austenitic matrix leading to get a more tensioned structure, enhancing the hardness.

5.3 Wear behaviour of SS316L+WC 10%

5.3.1 Profilometer observations

The results of the profilometer measurements reported in section 4.3.2 compared with the graphs of the COF evolution (section 4.3.1) are explained in this subchapter. Correlation between the number of carbides in the track with the worn sample volume and the worn of alumina ball are explained as well.

- Taking into account the 1° interrupted test stopped at 2000 cycles (Figure 4.34) arise as both wear of the sample and of the alumina ball already occur (Table 4.7 and Table 4.9). Making a comparison between the profilometer results of the uninterrupted tests with those of the 1° interrupted test, it can be noted that the number of cycles of the 1° interrupted test (2000) are the 9% of the cycles of each uninterrupted test (22000), where the worn volume of the track of the 1° uninterrupted test (0.2 mm^3) is the 17.24% of the average value of the worn track volume of the uninterrupted tests (1.16 mm^3). Whereas, the worn volume of the counter-body of the 1° uninterrupted test (0.07 mm^3) is the 12.55% of the average value of the alumina ball worn volume of the uninterrupted tests (0.5579 mm^3). Moreover, considering only the first wear stage as occured in the case of the sample W10-14 F6.3 (Figure 4.32), the worn track volume and the counter-body worn volume are the highest (Figure 5.2 and Figure 5.3). Based on these considerations, probably the combination of the wear phenomena leads to define the first wear stage as the most important.

- Considering the seven uninterrupted tests, the worn volume of the track and of the alumina ball are plotted against the number of carbides in the track in the Figure 5.2 and Figure 5.3. In Figure 5.2 the general trend of the worn sample volume may be noted, in which as the number of carbides in the track increases the worn sample volume decreases. The carbides protects the material, decreasing the penetration depth on the sample as Figure 4.38 shows.

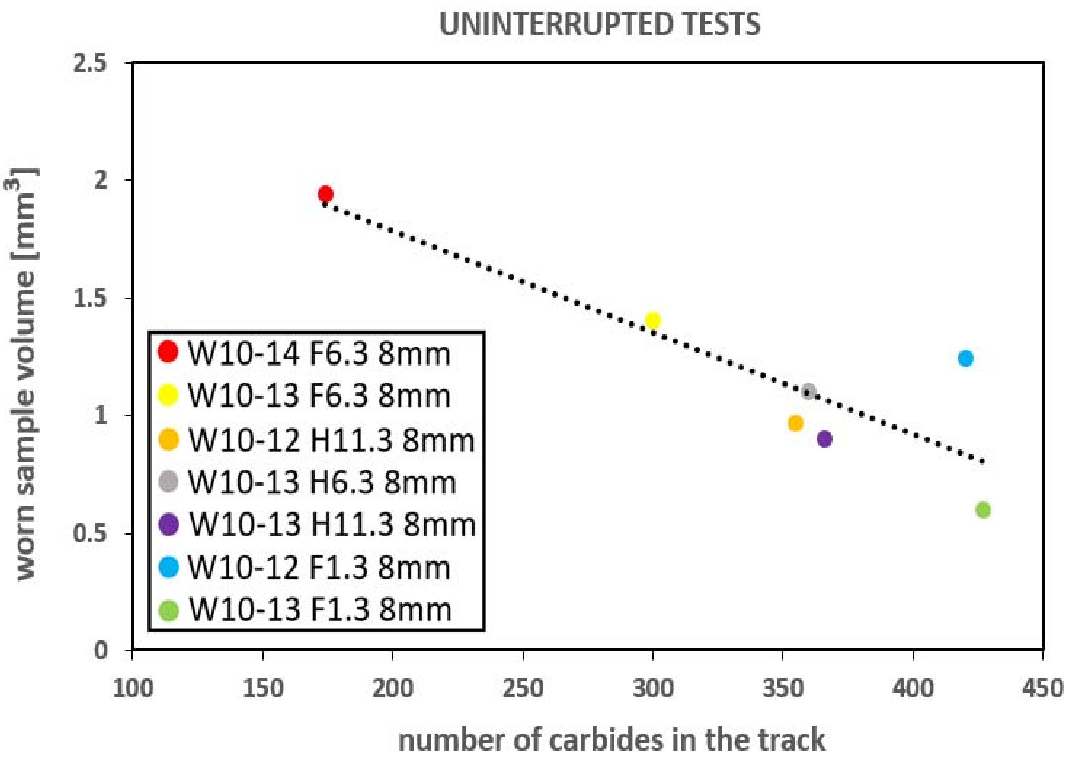

Figure 5.2: Worn sample volume against number of carbides in the track of the seven uninterrupted tests.

Considering the general trend of the experimental data represented in Figure 5.3, it can be observed that the number of the carbides in track increases the worn of the alumina ball decreases. This is due to the formation of the tribolayer from the carbides (Figures 4.43, 4.54, 4.55) and the worn of the matrix. Indeed, more carbides are present, more the formation of the tribolayer becomes simple, which reduce the wear on the counter-body.

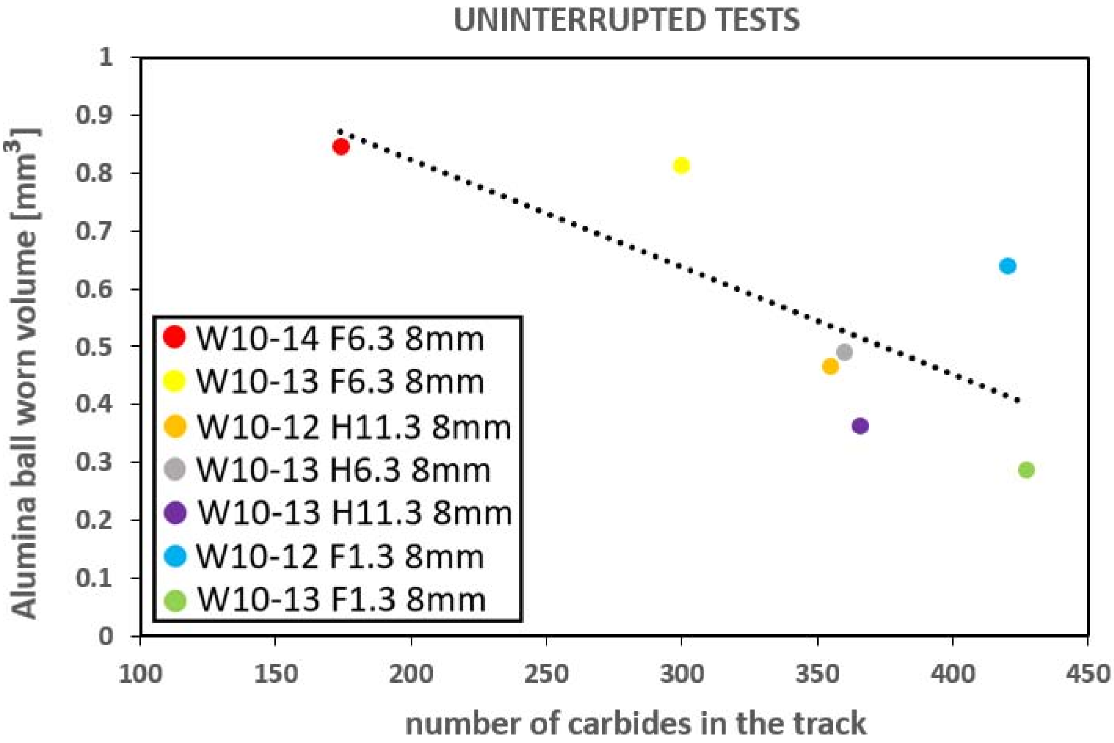

Figure 5.3: Alumina ball worn volume against number of carbides in the track of the seven uninterrupted tests.

5.3.2 Reproducibility

The COF and penetration depth curves obtained by wear tests considering the number of cycles should provide the same plots, regardless the sample and heights at which the tests are carried out. Each tribometer test carried out and their relative graphs shown in the section 4.3.1 exhibit similar trends with slight variations, characterised by the repetition of the stage 2 and stage 3, as may be noted in Figure 4.25. However, in some cases the COF evolution graphs can show different behaviour than usual. Indeed, in Figure 4.29 the COF curve does not follow the same behaviour of the other graphs (section 4.3.1), since during the stage 3 the COF drastically rises rather than suddenly falling. Instead, in Figure 4.32 only the stage 1 is shown, though it is an uninterrupted test. It is important to say that the tribometer tests were performed on different heights of the same sample as well as on different samples. As shown in the chapter 4, the features of the composite changes with the heights of the deposit. Moreover, different samples may have slight differences in composition due to the not always constant WC feed during the LC process and the not equal size of raw WC. The penetration depth curve decreases for a few cycles as soon as the COF drastically drops only for the Figure 5.4 and Figure 5.5. The sharp falls of the COF could be associated to the breakdown of the most part of the oxide layer forming during the test. The debris coming from this phenomenon may remain entrapped between the alumina ball and the track decreasing the penetration depth.

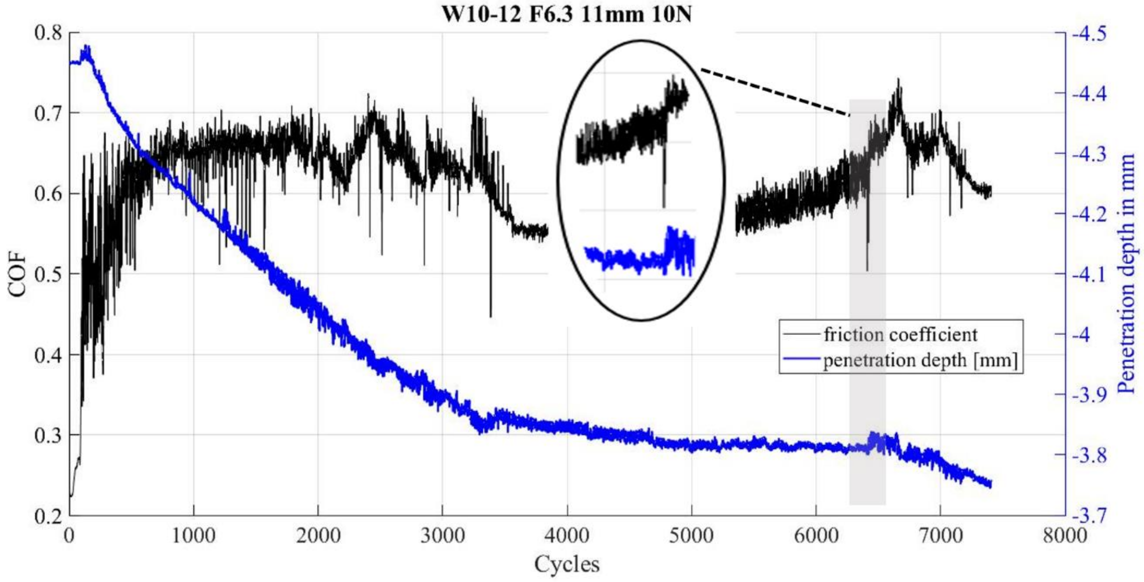

Figure 5.4: Tribometer test of the sample W10-12 F6.3 with radius 11mm. The zoom in shows as the decreases in penetration depth occurs when the COF suddenly drops.

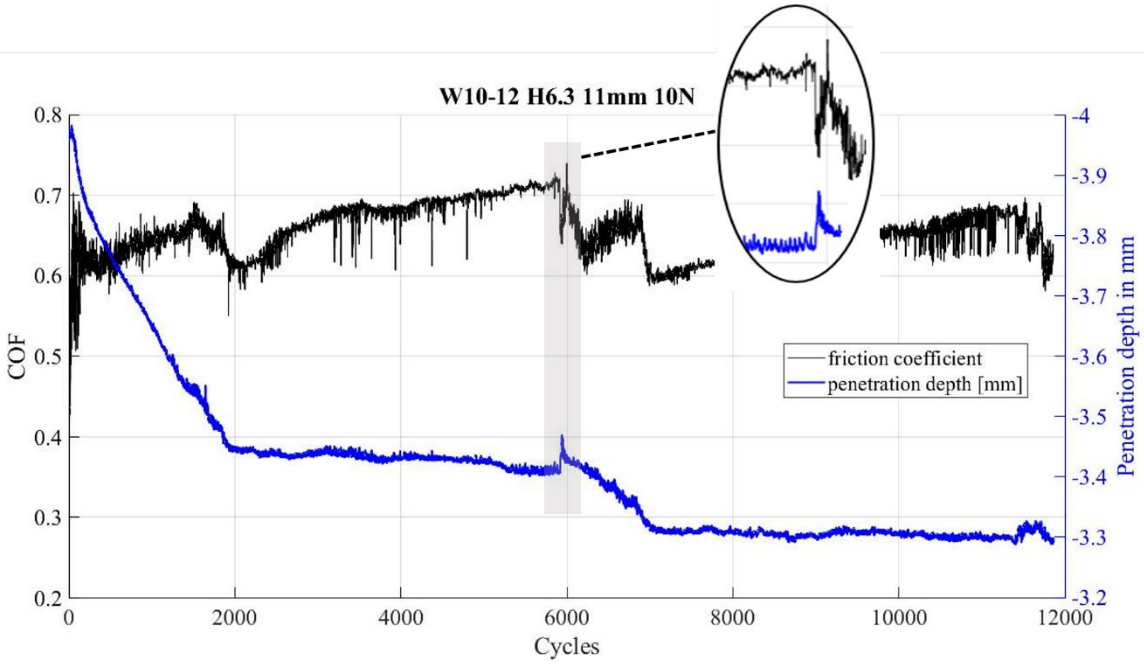

Figure 5.5: Tribometer test of the sample W10-12 H6.3 with radius 11mm. The zoom in shows as the decreases in penetration depth occurs when the COF suddenly drops.

5.3.3 *Wear sequence*

The tribometer tests have shown a relative high grade of reproducibility. Based on it, the graph of Figure 4.25 has been used as a reference to establish the targets of the interrupted tests in order to analyse the worn surfaces in different zones of the COF. The explanation of the wear sequence will be given in this section taking into account the whole results. The graph in Figure 5.6 was divided in three main areas.

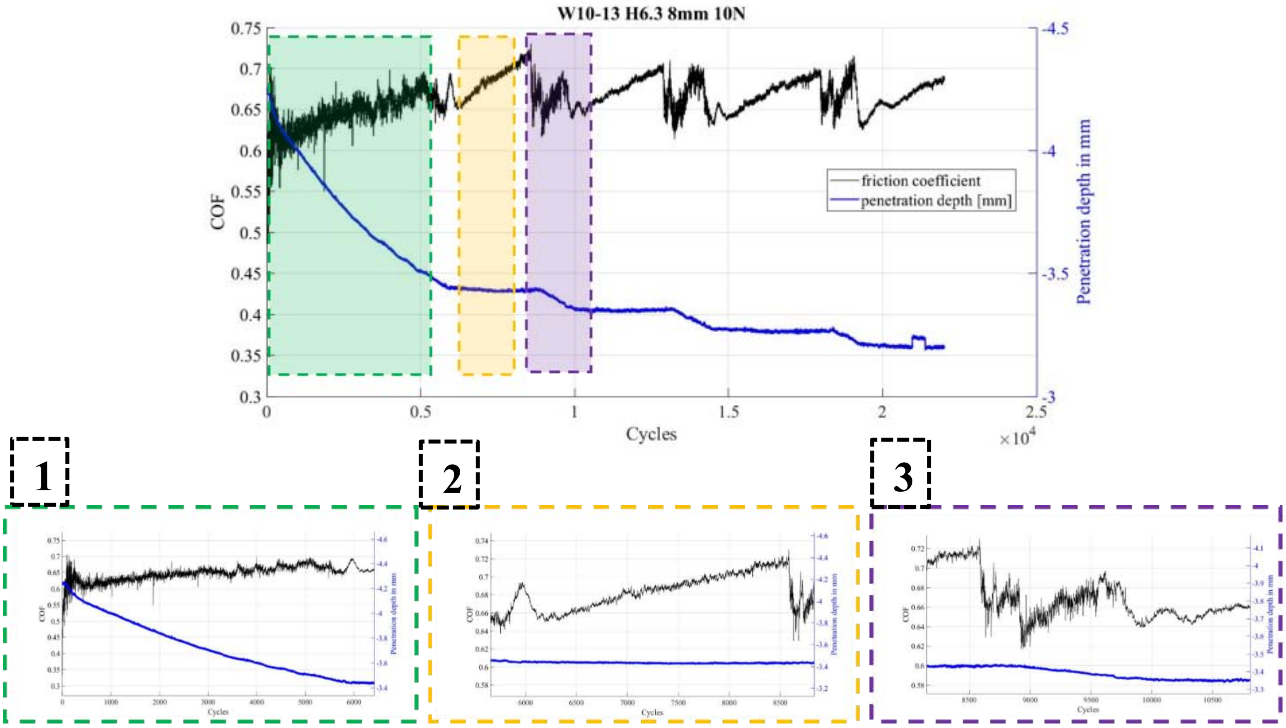

Figure 5.6: Tribometer test used as reference. The three main wear stages are represented in green, yellow and violet colour together with the zoom in of each stage.

Each of them will be considered separately in order to associate the wear beahaviors in every wear stage (green, yellow and violet rectangles) with the evolution of the COF and penetration depth curves.

1

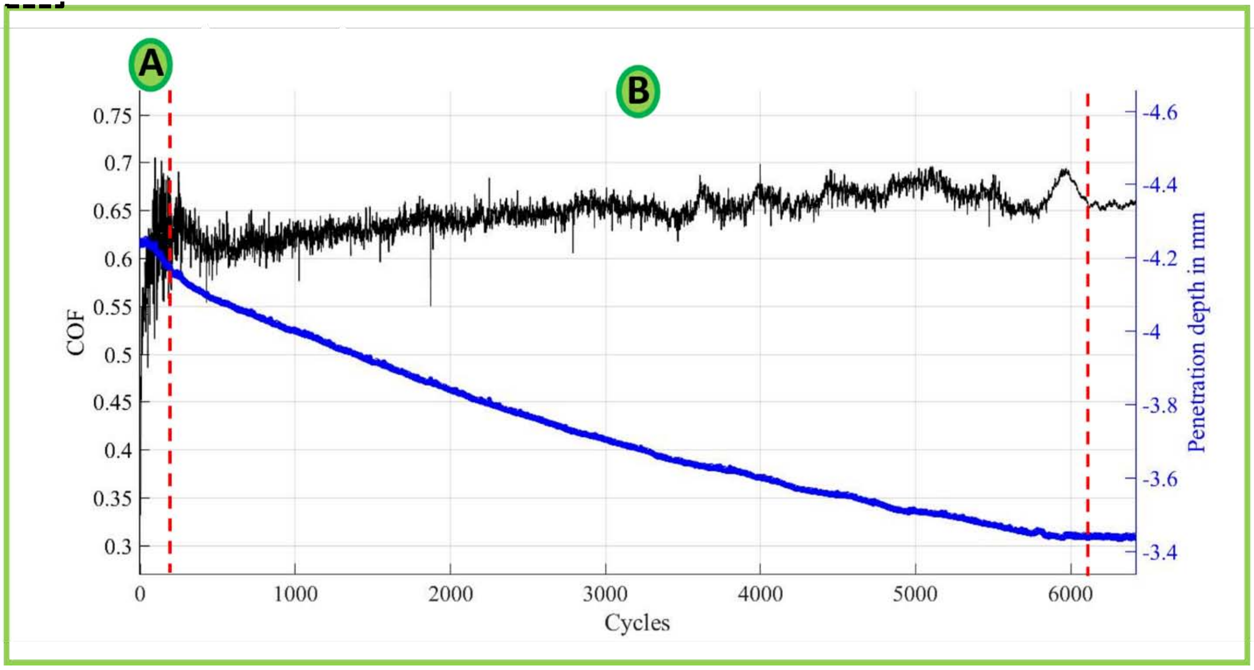

Figure 5.7: First wear stage based on Figure 5.6. The evolution of the penetration depth and COF curves suggests the presence of different wear mechanisms.

A) Considering the evolution of the COF curve related with penetration depth curve, the first sharp increase of COF may be associated to **adhesive wear** [59], since the two relative surfaces are completely free of contaminations at the beginning of the test and the asperities are always present on the surface provoking bonds with the ball (section 2.5, [39]). The penetration depth remain costant and then starts to increases.

B) From Figure 4.49 can be noted that a slight deformation of the matrix occurs afer a certain cycles in which a mixture of oxide is embedded due to the strain accumulation. This wear phenomenon can be associated to **delamination** (section 2.5, [44]). The plastic deformation of the matrix may cause strain hardening and it may lead to a relative long stage. In addition, the **adhesive wear** is still present due to the stacking of the alumina in front of WC (Figure 4.48). Moreover, the presence of grooves (Figure 4.47) suggests the presence of **2-body abrasion** both on the matrix and on the ball. During this stage, the amount of debris becomes more relevant and they may enrich the formation of the tribolayer in the grooves. The penetration depth starts to increases due to the three wear mechanisms.

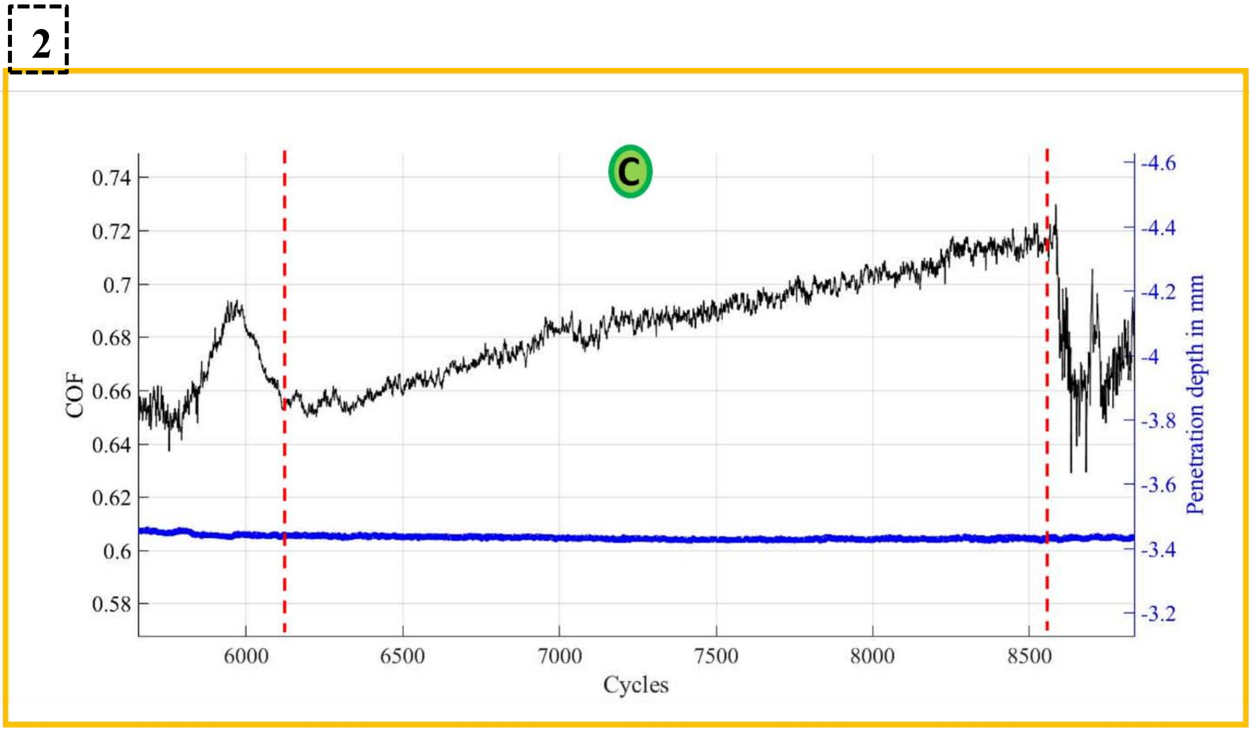

Figure 5.8: Second wear stage based on Figure 5.6. The evolution of the penetration depth and COF curves suggests the presence of one wear mechanism.

C) When the compactation of the tribolayer takes place,the COF has a steady value or slighlty increases it can be associated to **oxidative wear** [39], [32]. In addition to the debris of alumina and the tribolayer formed by the presence of the WC carbides, the presence of oxygen in the air during the test leads to partial oxidation of the tribolayer.

Nevertheless, the oxidation is a minor phenomenon since it is thermally activated and in those tests at room temperature hot spots are possible, but it is not possible achieve high temperatures. However, the stage representing oxidative wear appears after a certain number of cycles since the formation of the tribolayer requires time. Furthermore, the penetration depth remains stable (alumina ball and composite are not worn in this step). In some cases, the penetration depth curve in this area is not completely flat (i.e. Figure 4.36 and Figure 4.37), exhibiting many small peaks and valleys, but remaining overall constant. The tribolayer formation is not always completely compact and this could justify these small changes.

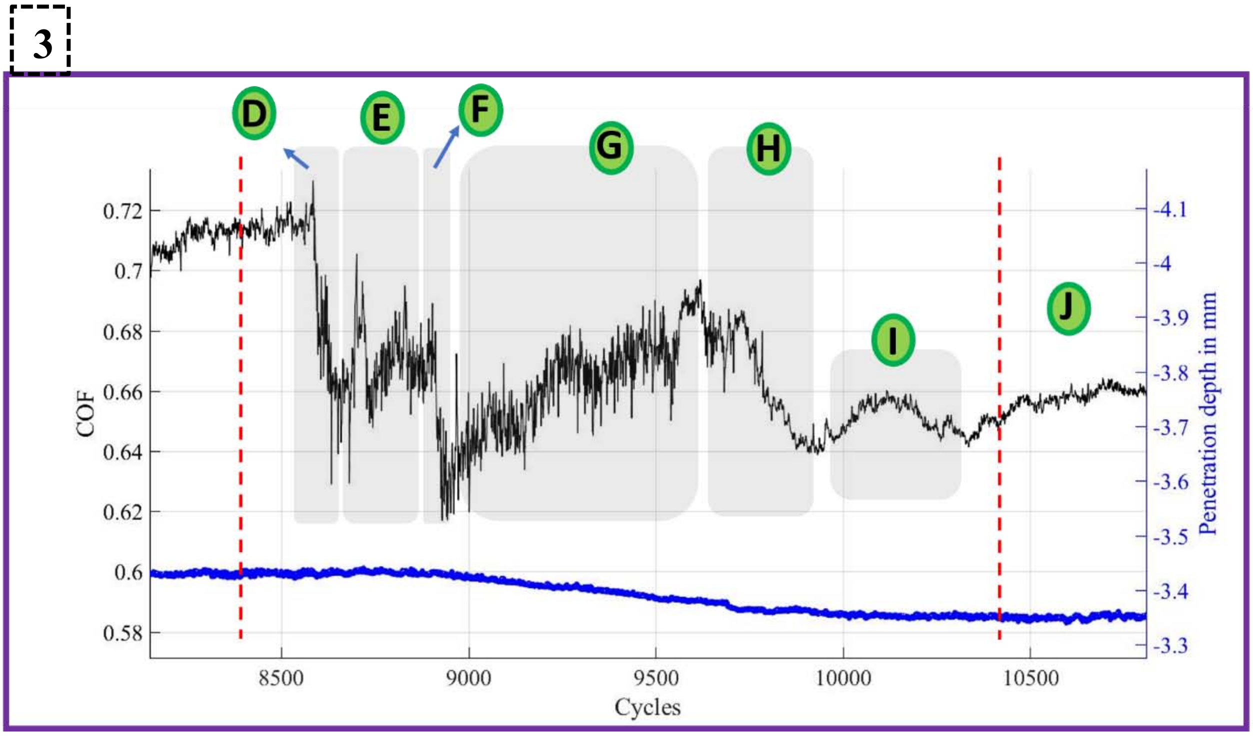

Figure 5.9: Third wear stage based on Figure 5.6. The evolution of the penetration depth and COF curves suggests the presence of different wear mechanisms.

D) During the oxydative wear, the quantity of the debris increases with the progress of the test together with the compactation of the tribolayer. When the thickness of the tribolayer reaches a threshold value, a large part of it **breaks down** (Figure 4.51) [39], corresponding to a sharp fall of COF since the counter body finds less resistance. At this point, the penetration depth is still constant, even though sometimes the penetration depth seems to decreases for a few cycles (section 5.3.2).

E-F) The removal of debris occurs leads to a short increase of the penetration depth.

G) When the surface is relatively clean, the direct contact between the alumina ball with the surface of the track can generate a difference in level among the surface of carbide and the matrix below the stacking of material (Figure 4.56). The evolution of this process tends to fracture more and more the carbides into small particles. The fractured particles mixed with wear debris cannot be easily evacuated from the track, leading to increases the COF. Indeed, those particle lead to the formation of very deep grooves (Figure 4.53) due to **3-body abrasion** [37]. The penetration depth increases due to the wear of the track and of the alumina in contact with the WC carbides in relief.

H) When the debris entrapped inside the track can go away cycle by cycle, the friction coefficient decreases whereas the pentration depth is at the end of its increaes. Indeed, the abrasion mechanism does not occur anymore since the surface does not exhibit deep grooves (Figure 4.57). Furthermore, Figure 4.58 suggests the formation of a **new tribolayer** in this region.

I) The formation of the new tribolayer is not immediately stable and a small peak of the COF can be noted in this zone. It could be associated to **transition zone**.

J) This region is characterised by the same wear behaviour of the region C (**oxidative wear**). After that, a cyclical wear behaviour may be noted, since the same scenario is repeated more times during each test.

The wear mechanisms and their main observations together with the evolution of COF and penetration depth curves are summarized in a Table 5.1.

	Wear mechanism	**Observations**	**COF curve behaviour**	**Penetration depth curve behaviour**
A	**Adhesive on matrix and on WC**	Surfaces free of contaminations [39]; Asperities are always present on the surface [39]	Suddenly increases	Constant, then starts to increases
B	**Delamination** + **Adhesive on WC** + **Abrasive on matrix**	Strain accumulation [44]; Stacking of the alumina in front of WC; Grooves	Slightly increases (presence of many small peaks and valleys)	Increases
C	**Oxidative wear**	COF has a steady value [39,32]; Presence of oxygen (air and alumina ball); Relative high temperature	Slightly increases (no small peaks and valleys, almost flat)	Constant
D	**Tribolayer breakdown**	Threshold value thickness [39]	Drastically falls	Constant

E-F		Removal of debris	Increases for a few cycles; Decreases for a few cycles	Constant; Starts to increases
G	**3-body abrasion**	Small parts of tungsten carbide are spread over in the track [43] + Presence of the remaining debris = Generation of deep grooves [37]	Increases	Increases
H	**No abrasion anymore**	Debris entrapped inside the track cycle by cycle can go away	Decreases	Increases
I	**New tribolayer**	Not immediately stable	Slightly increases and the decreases	Constant
J=C	**Oxidative wear**	COF has a steady value [39,32].	Slightly increases (no small peaks and valleys, almost flat)	Constant

Table 5.1: Correlation between wear mechanisms and their main causes of the SS316L+10%volWC composite. Also penetration depth and COF behaviours curves are considered.

6. Conclusions

The main purpose of this work was focused on the study of the wear sequence in the SS316L+10%WC composite in order to have a full comprehension regarding the different wear mechanism acting on this material. For this purpose, many wear tests were carried out and correlated with a microstructural characterization. Moreover, Vickers hardness tests was also performed to have proof that tungsten carbides reinforcement enhance the hardness compared with traditional SS316L.

- It is relevant to take into account that the wear tests were carried out at different heights in the same sample. The grain size and the mean % of W change at different heights from the substrate (Table 4.3 and Figure 4.17, respectively) leading to a not constant value of the hardness (Figure 4.23). Also different number of carbides in the tracks on different surfaces were counted (Table 4.20). This anisotropy could be the reason for which the tribometer tests sometimes are not reproducible.
- Image analysis on the image obtained by means of OM exhibits a homogeneous distribution of the carbides in the matrix, without consider the last deposited layers (Figure 4.6 b and c). The size of the undissolved carbides may vary from 20 to 130μm due to the partial dissolution of virgin WC (Figure 4.6 d).
- EBSD analyses confirmed the presence of out-of-equilibrium structures. Many types of carbides were identified in the vicinities of a big undissolved WC and inside of it i.e. $M_{23}C_6$, M_6C, M_4C, M_2C, MC and γ-MC_{1-x}. Whereas far away from the giant WC only M_4C (in the track) and M_6C (in the HAZ) were observed. EDS and EBSD analyses have demonstrated the presence of chromium carbide only close to the undissolved WC.

7. *Perspectives*

The good corrosion resistance of the SS316L and the high wear resistance of the WC reinforcement are combined together in this metal matrix composite. The corrosion resistance of the pure 316L is already well known. Hence, one of the next steps could be investigate the corrosion resistance of the SS316L+WC composite with electrochemical tests. A comparison between previous work [7], in which the same composite but with 20% (vol. %) of WC were studied, and this work, shows as the chromium carbides are placed in different zones in the two materials. With 20% of WC, chromium carbides are present close and also far (in the HAZ) to the giant WC, whereas in this work the presence of chromium carbides is only close to the undissolved carbides. The less amount of carbon available leads to have less chromium carbides with 10% of WC. Hence, could be reasonable have higher corrosion resistance with 10% of WC.

Traces of Al derived by the worn of the Al_2O_3 ball were noted in every track analysed. This together with the always presence of oxygen could increase the worn of the alumina ball. Basically, traces of aluminium oxides into the track could enhance the worn of the alumina ball. Could be interesting change the material of the counter-body.

Stainless steel is widely used in aerospace field and many industrial environments which are characterised by high temperature conditions. For this reason, wear tests at high temperature could be perform to investigate the wear behaviour at high temperature.

8. References

[1] M. Belotserkovsky, A. Yelistratov, A. Byeli, and V. Kukareko, “Steel thermal sprayed coatings: Superficial hardening by nitrogen ion implantation,” *Weld. J. (Miami, Fla)*, vol. 88, no. 12, 2009.

[2] “Corrosion behaviour and microhardness of plasma-sprayed WNi composite coatings Morks MF, Fahim NF, Kobayashi Manuf Process 2008,” p. 2008, 2008.

[3] Z. Wu, “Empirical modeling for processing parameters’ effects on coating properties in plasma spraying process,” *J. Manuf. Process.*, vol. 19, pp. 1–13, 2015, doi: 10.1016/j.jmapro.2015.03.007.

[4] P. F. Mendez *et al.*, “Welding processes for wear resistant overlays,” *J. Manuf. Process.*, vol. 16, no. 1, pp. 4–25, 2014, doi: 10.1016/j.jmapro.2013.06.011.

[5] S. M. Shariff, T. K. Pal, G. Padmanabham, and S. V. Joshi, “Sliding wear behaviour of laser surface modified pearlitic rail steel,” *Surf. Eng.*, vol. 26, no. 3, pp. 199–208, 2010, doi: 10.1179/174329409X455458.

[6] D. Herzog, V. Seyda, E. Wycisk, and C. Emmelmann, “Additive manufacturing of metals,” *Acta Mater.*, vol. 117, pp. 371–392, 2016, doi: 10.1016/j.actamat.2016.07.019.

[7] D. Mario, “Room temperature wear behavior of laser clad 316L + WC composite coating Université de Liège – Università degli Studi di Padova Faculté des Sciences Appliquées - Scuola di Ingegneria Room temperature wear behavior of laser clad 316L + WC co,” 2019.

[8] M. Ziętala *et al.*, “The microstructure, mechanical properties and corrosion resistance of 316 L stainless steel fabricated using laser engineered net shaping,” *Mater. Sci. Eng. A*, vol. 677, pp. 1–10, 2016, doi: 10.1016/j.msea.2016.09.028.

[9] Y. Zhai, D. A. Lados, and J. L. Lagoy, “Additive Manufacturing: Making imagination the major Limitation,” *Jom*, vol. 66, no. 5, pp. 808–816, 2014, doi: 10.1007/s11837-014-0886-2.

[10] M. Yan and P. Yu, “An Overview of Densification, Microstructure and Mechanical Property of Additively Manufactured Ti-6Al-4V — Comparison among Selective Laser Melting, Electron Beam Melting, Laser Metal Deposition and Selective Laser Sintering, and with Conventional Powder,” *Sinter. Tech. Mater.*, 2015, doi: 10.5772/59275.

[11] Y. Lee, M. Nordin, S. S. Babu, and D. F. Farson, “Effect of fluid convection on dendrite arm

spacing in laser deposition," *Metall. Mater. Trans. B Process Metall. Mater. Process. Sci.*, vol. 45, no. 4, pp. 1520–1529, 2014, doi: 10.1007/s11663-014-0054-7.

[12] W. E. Frazier, "Metal additive manufacturing: A review," *J. Mater. Eng. Perform.*, vol. 23, no. 6, pp. 1917–1928, 2014, doi: 10.1007/s11665-014-0958-z.

[13] W. E. King *et al.*, "Laser powder bed fusion additive manufacturing of metals; physics, computational, and materials challenges," *Appl. Phys. Rev.*, vol. 2, no. 4, p. 041304, 2015, doi: 10.1063/1.4937809.

[14] M. S. Węglowski, S. Błacha, J. Pilarczyk, J. Dutkiewicz, and L. Rogal, "Electron beam additive manufacturing with wire - Analysis of the process," *AIP Conf. Proc.*, vol. 1960, no. February, 2018, doi: 10.1063/1.5035007.

[15] S. Mokadem, C. Bezençon, A. Hauert, A. Jacot, and W. Kurz, "Laser repair of superalloy single crystals with varying substrate orientations," *Metall. Mater. Trans. A Phys. Metall. Mater. Sci.*, vol. 38 A, no. 7, pp. 1500–1510, 2007, doi: 10.1007/s11661-007-9172-z.

[16] H. Paydas, A. Mertens, R. Carrus, J. Lecomte-Beckers, and J. Tchoufang Tchuindjang, "Laser cladding as repair technology for Ti-6Al-4V alloy: Influence of building strategy on microstructure and hardness," *Mater. Des.*, vol. 85, pp. 497–510, 2015, doi: 10.1016/j.matdes.2015.07.035.

[17] G. Abbas and U. Ghazanfar, "Two-body abrasive wear studies of laser produced stainless steel and stainless steel + SiC composite clads," *Wear*, vol. 258, no. 1-4 SPEC. ISS., pp. 258–264, 2005, doi: 10.1016/j.wear.2004.09.036.

[18] A. Mertens, S. Reginster, Q. Contrepois, T. Dormal, O. Lemaire, and J. Lecomte-Beckers, "Microstructures and mechanical properties of stainless steel AISI 316L processed by selective laser melting," *Mater. Sci. Forum*, vol. 783–786, pp. 898–903, 2014, doi: 10.4028/www.scientific.net/msf.783-786.898.

[19] N. R. Baddoo, "Stainless steel in construction: A review of research, applications, challenges and opportunities," *J. Constr. Steel Res.*, vol. 64, no. 11, pp. 1199–1206, 2008, doi: 10.1016/j.jcsr.2008.07.011.

[20] Y. H. Kim, K. Y. Kim, and Y. D. Lee, "Nitrogen-alloyed, metastable austenitic stainless steel for automotive structural applications," *Mater. Manuf. Process.*, vol. 19, no. 1, pp. 51–59, 2004, doi: 10.1081/AMP-120027498.

[21] A. Atlas Steels, “Stainless Steel 316L & 316H Data Sheet,” pp. 1–2, 2011.

[22] “Qusongite (wc): A new mineral Q. Fang, W. Bai, J. Yang, X. Xu, G. Li, N. Shi, M. Xiong, H. Rong 94 (2009) 387 – 390,” vol. 94, p. 2009, 2009.

[23] A. S. Kurlov and A. I. Gusev, “Tungsten carbides and W-C phase diagram,” *Inorg. Mater.*, vol. 42, no. 2, pp. 121–127, 2006, doi: 10.1134/S0020168506020051.

[24] Granta, “CES EduPack 2017,” p. 2017, 2017, doi: 10.1017/CBO9781107415324.004.

[25] J. W. Kaczmar, K. Pietrzak, and W. Wlosiński, “Production and application of metal matrix composite materials,” *J. Mater. Process. Technol.*, vol. 106, no. 1–3, pp. 58–67, 2000, doi: 10.1016/S0924-0136(00)00639-7.

[26] “Additive-Manufacturing-of-Al-Alloys-and-Aluminium- Matrix Composites Manfredi-Calignano-Canali 2014,” p. 2014, 2014.

[27] S. C. Tjong and K. C. Lau, “Abrasion resistance of stainless-steel composites reinforced with hard TiB2 particles,” *Compos. Sci. Technol.*, vol. 60, no. 8, pp. 1141–1146, 2000, doi: 10.1016/s0266-3538(00)00008-7.

[28] J. C. Betts, B. L. Mordike, and M. Grech, “Characterisation, wear and corrosion testing of laser-deposited AISI 316 reinforced with ceramic particles,” *Surf. Eng.*, vol. 26, no. 1–2, pp. 21–29, 2010, doi: 10.1179/174329409X433920.

[29] G. Thawari, G. Sundararарjan, and S. V. Joshi, “Laser surface alloying of medium carbon steel with SiC(P),” *Thin Solid Films*, vol. 423, no. 1, pp. 41–53, 2003, doi: 10.1016/S0040-6090(02)00974-4.

[30] M. Yakout, M. A. Elbestawi, and S. C. Veldhuis, “Density and mechanical properties in selective laser melting of Invar 36 and stainless steel 316L,” *J. Mater. Process. Technol.*, vol. 266, no. July 2018, pp. 397–420, 2019, doi: 10.1016/j.jmatprotec.2018.11.006.

[31] S. Rawal, “Metal-matrix composites for space applications,” *Jom*, vol. 53, no. 4, pp. 14–17, 2001, doi: 10.1007/s11837-001-0139-z.

[32] M. Vardavoulias, “The role of hard second phases in the mild oxidational wear mechanism of high-speed steel-based materials,” *Wear*, vol. 173, no. 1–2, pp. 105–114, 1994, doi: 10.1016/0043-1648(94)90262-3.

[33] M. L. Griffith *et al.*, “Understanding thermal behavior in the LENS process,” *Mater. Des.*,

vol. 20, no. 2–3, pp. 107–113, 1999, doi: 10.1016/s0261-3069(99)00016-3.

[34] Y. Zhong, L. Liu, S. Wikman, D. Cui, and Z. Shen, “Intragranular cellular segregation network structure strengthening 316L stainless steel prepared by selective laser melting,” *J. Nucl. Mater.*, vol. 470, pp. 170–178, 2016, doi: 10.1016/j.jnucmat.2015.12.034.

[35] J. D. Majumdar, A. Pinkerton, Z. Liu, I. Manna, and L. Li, “Mechanical and electrochemical properties of multiple-layer diode laser cladding of 316L stainless steel,” *Appl. Surf. Sci.*, vol. 247, no. 1–4, pp. 373–377, 2005, doi: 10.1016/j.apsusc.2005.01.131.

[36] E. Mancini, “Studio delle etereogenità microstrutturali in un rivestimento composito a matrice metallica di acciaio inossidabile 316L e carburo di tungsteno,” p. 2017, 2017.

[37] C. X. Li, J. Xia, and H. Dong, “Sliding wear of TiAl intermetallics against steel and ceramics of Al2O3, Si3N4 and WC/Co,” *Wear*, vol. 261, no. 5–6, pp. 693–701, 2006, doi: 10.1016/j.wear.2006.01.044.

[38] H. Dong and T. Bell, “Designer surfaces for titanium components,” *Anti-Corrosion Methods Mater.*, vol. 46, no. 3, pp. 181–188, 1999.

[39] “Engineering Tribology G.W. Stachowiak Butterworth-Heinemann, Oxford, 2013.,” p. 2013, 2013.

[40] H. I. M and S. Philip, “Tribology : friction and wear of engineering materials / Ian M Hutchings; Philip Shipway.,” p. undefined-undefined, 2017.

[41] “American Society for metals ASM. Metals Handbook, vol. 15:Casting .,” vol. 18, p. 1256, 2008.

[42] N. Serres, F. Hlawka, S. Costil, C. Langlade, F. Machi, and A. Cornet, “Dry coatings and ecodesign. Part. 2 - Tribological performances,” *Surf. Coatings Technol.*, vol. 204, no. 1–2, pp. 197–204, 2009, doi: 10.1016/j.surfcoat.2009.07.011.

[43] M. R. Fernández, A. García, J. M. Cuetos, R. González, A. Noriega, and M. Cadenas, “Effect of actual WC content on the reciprocating wear of a laser cladding NiCrBSi alloy reinforced with WC,” *Wear*, vol. 324–325, pp. 80–89, 2015, doi: 10.1016/j.wear.2014.12.021.

[44] A. Kapoor and F. J. Franklin, “Tribological layers and the wear of ductile materials,” *Wear*, vol. 245, no. 1–2, pp. 204–215, 2000, doi: 10.1016/S0043-1648(00)00480-4.

[45] “Hoganas (n.d.). httpswww.hoganas.com (accessed May 19, 2019),” p. 2019, 2019.

[46] "Sirris. httpswww.sirris.be (accessed May 19, 2019).pdf." .

[47] C. S. M. T. Features, "CSM Technical Features //// HIGH TEMPERATURE TRIBOMETER (THT)," p. 2009, 2009.

[48] Alicona, "Alicona Cobots Real3D," vol. 7, p. 2017, 2017.

[49] T. M. Enrici, "Microstructural and Thermal Characterization of 316L+WC Composite Coatings by Laser Cladding," p. 316, 2018.

[50] M. Godec *et al.*, "Characterization of the carbides and the martensite phase in powder-metallurgy high-speed steel," *Mater. Charact.*, vol. 61, no. 4, pp. 452–458, 2010, doi: 10.1016/j.matchar.2010.02.003.

[51] J. Laigo, F. Christien, R. Le Gall, F. Tancret, and J. Furtado, "SEM, EDS, EPMA-WDS and EBSD characterization of carbides in HP type heat resistant alloys," *Mater. Charact.*, vol. 59, no. 11, pp. 1580–1586, 2008, doi: 10.1016/j.matchar.2008.02.001.

[52] P. Ding, G. Shi, and S. Zhou, "As-cast carbides in high-speed steels," *Metall. Trans. A*, vol. 24, no. 6, pp. 1265–1272, 1993, doi: 10.1007/BF02668195.

[53] C. G. Levi, "Thermal considerations on the recalescence of alloy powders," *Metall. Trans. A*, vol. 19, no. 3, pp. 687–697, 1988, doi: 10.1007/BF02649283.

[54] X. Cai, Y. Xu, M. Liu, and L. Zhong, "Evaluation of microstructure and growth kinetics of tungsten carbide ceramics at the interface of iron and tungsten," *J. Alloys Compd.*, vol. 741, pp. 666–676, 2018, doi: 10.1016/j.jallcom.2018.01.212.

[55] F. Z. Abderrahim, H. I. Faraoun, and T. Ouahrani, "Structure, bonding and stability of semi-carbides M 2C and sub-carbides M 4C (M=V, Cr, Nb, Mo, Ta, W): A first principles investigation," *Phys. B Condens. Matter*, vol. 407, no. 18, pp. 3833–3838, 2012, doi: 10.1016/j.physb.2012.05.070.

[56] T. Maurizi Enrici, A. Mertens, M. Sinnaeve, and J. T. Tchuindjang, "Elucidation of the solidification sequence of a complex graphitic HSS alloy under a combined approach of DTA and EBSD analyses," *J. Therm. Anal. Calorim.*, vol. 13, no. 0123456789, 2019, doi: 10.1007/s10973-019-09093-9.

[57] M. L. Griffith, "Mater. & Des.," vol. 20, p. 1999, 1999.

[58] A. Yadollahi, N. Shamsaei, S. M. Thompson, and D. W. Seely, "Effects of process time

interval and heat treatment on the mechanical and microstructural properties of direct laser deposited 316L stainless steel," *Mater. Sci. Eng. A*, vol. 644, pp. 171–183, 2015, doi: 10.1016/j.msea.2015.07.056.

[59] L. J. O'Donnell, "Tribology Of 316l Austenitic Stainless Steel Carburized At Low Temperature," *Wear*, no. January, p. 120, 2010.